UNIVERSITAS STUDIORUM MEDIOLANENSIS

Facoltà di Scienze Matematiche Fisiche e Naturali
Scuola di Dottorato in Fisica, Astrofisica e Fisica Applicata

Quench protection and design of high-field superconducting accelerator magnets: the role of dynamic effects on the differential inductance

Relatore: Dr. SORBI Massimo

Tesi di dottorato di:
MARINOZZI Vittorio
Matr. R-10474

Ciclo XXIX

Contents

Chapter 1

Superconductivity and accelerator magnets

1.1 Introduction

Superconductivity is one of the most revolutionary discoveries of the XXth century. The possibility of having materials with exactly null resistivity has opened new ways in different fundamental research areas, until now.
One of the main application of superconductivity is the design of accelerator magnets. Before the development of superconducting cables, accelerator magnets were basically iron-dominated electro-magnets. These categories allowed to reach magnetic fields of few Tesla (iron saturates at about 2 T), using a reasonable amount of copper cables. In order to go beyond, a huge amount of copper is needed, and a huge power dissipation due to the resistance of the material has to be taken into account. For this reason, the energy of the accelerated beams was mainly limited by the bending capability of the dipoles. The introduction of superconductivity, instead, has allowed to reach much higher magnetic fields (for example, LHC has 8 T dipoles), therefore to reach higher beam energy, with basically null power dissipation within the cables, and with reasonable coil dimension. This allowed, for example, to break the TeV wall at Tevatron, and to discover the

Higgs Boson at LHC in a reasonable time (few years of machine operation). In this chapter, an introduction of the main phenomena concerned to superconductivity is given, with particular regard to the application in accelerator magnets. Then the concept of magnet quench is treated more in depth.

1.2 Superconductivity signs

Superconductivity is a special matter state, discovered in the 1911 by the Dutch physicist Heike Kamerlingh Onnes. In those years, there were discussions within the scientific community on what was the behavior of metal resistivity going close to 0 K temperature. It was well known that the resistivity was proportional with the temperature, because of the motion of the lattice nuclei, therefore some scientists said that the resistivity had to go to zero, because at null temperature the nuclei had to stop their motion (quantum mechanics was not yet understood); other scientists, said that at zero temperature the electrons could not move, because they were such as freezed; therefore the resistivity had to diverge to infinite. In this scenario, the technological progress made possible to liquefy the helium (4.2 K), giving possibilities to clarify this discussion. Onnes, therefore, worked on mercury samples, reducing their temperature as much as possible. Going under a certain temperature, he noted that the resistivity of the samples went suddenly to zero, which was a phenomenon different from the two described before. He called this phenomenon *Superconductivity*. Then, it was discovered that superconductivity is not only null resistivity, but it is also magnetic field expulsion (*Meissner effect*). Superconducting properties have lots of applications (for example, Meissner effect is exploited to build magnetic levitation trains), but we are mostly interested in applications on particle accelerator development. In particular, it is possible to develop high-field magnets by making use of superconducting materials, because they have null electrical resistivity, so very high currents can flow through them without generating heat. Therefore, you can get very high fields at lower costs than with standard resistive magnets.

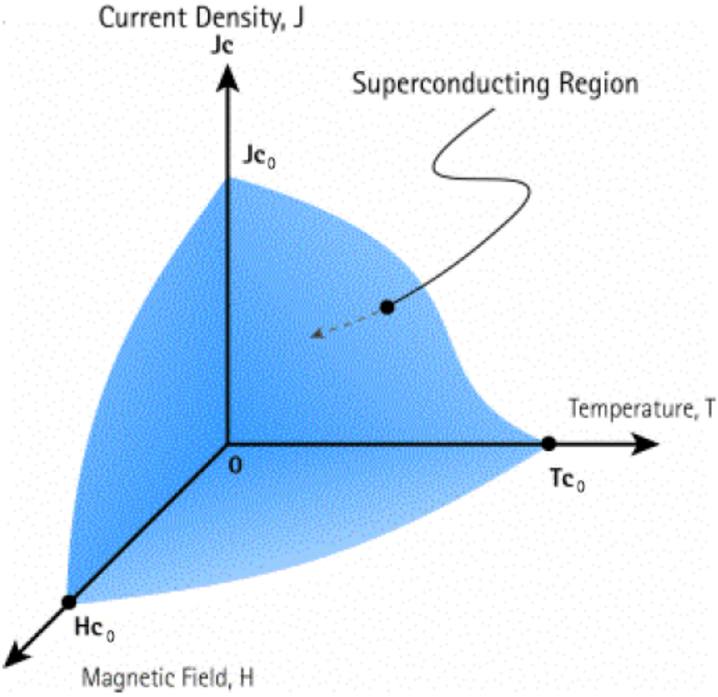

Figure 1.1: Critical surface example: a material maintain his superconducting properties under it

We have already said that a superconducting material has to be under a certain temperature, called *critical temperature*, in order to maintain its superconducting properties. Actually, this temperature also depends on the density current which flows in the material, and on the magnetic field applied on the material; in practice, in order to maintain superconducting properties, a material has to be in a zone delimited by a so called *critical surface*, such as the one you can see in Fig. 1.1. Interceptions with the three axes are called *critical temperature* T_{c0}, *critical field* H_{c0} and *critical current* J_{c0}. You can note that on the critical surface, while one quantity rises, both the others decrease. It's so clear that if you want to utilize superconductors, you must maintain these parameters under their critical values; obviously, critical values vary in dependence of the chosen material. All these considerations are valid for materials called *type-I superconductors*; another class of superconductors, called *type-II superconductors*, has instead two critical values for the magnetic field (H_{c1} and H_{c2}): below the first of them, material is like an usual type-I superconductor; between the first and the second, magnetic field can partially penetrate inside the material, but superconducting features are held; beyond the second, the material loses superconducting properties. Type-II superconductors are therefore the ones used in magnets development, because generally they can reach magnetic fields higher than type-I superconductors can do.

Until now, $NbTi$ (*niobium-titanium*) has been the most utilized type-II superconductor in accelerator magnets. Critical parameters are reported in Tab. 1.1. $NbTi$ can so be used as superconductor if cooled with liquid helium at a temperature of 1.9 K (superfluid helium temperature), or with boiling helium (4.2 K). $NbTi$ has mechanical properties similar to those of simple metals.

Critical values $NbTi$			
T_{c0}	J_{c0}	H_c1	H_c2
9.2 K	$\sim 10^6\ A/mm^2$	0.1 T	10 T

Table 1.1: Critical values for $NbTi$

NbTi has almost reached its highest performances, therefore, in the last years, the study of another superconducting material, the Nb_3Sn (*niobium-three-tin*), has been carried on in order to design accelerator magnets. In fact, Nb_3Sn has more performance features, as you can see in tab. 1.2. However, it has mechanical properties more similar to those of ceramics than to those of metals, so the realization of windings is very difficult; moreover, protection systems of Nb_3Sn magnets have to be more efficient, and we will see why in the next chapter.

Critical values Nb_3Sn			
T_{c0}	J_{c0}	H_c1	H_c2
$18.3\ K$	$\sim 10^6\ A/mm^2$	$0.05\ T$	$25\ T$

Table 1.2: Critical values for Nb_3Sn

1.3 Causes of quench

We have already seen that a material has to stay under its critical surface in order to maintain superconducting properties. When one of the three parameters (temperature, field or current) exceeds its critical value, the material leaves the superconductive state and it returns in the normal state: when this happens in a magnet, this phenomenon is called **quench**. Clearly, its consequences could be destructive, because currents of tens kA suddenly flow in cables with bad electrical and thermal features (superconductors are usually bad conductors in their resistive state): so, in case of quench, normal zones have to dissipate as heat all the stored energy $\frac{1}{2}LI^2$, and there is risk of damaging, or even melting cables. Quench study is therefore very important in the design of a superconducting magnet.

The possible causes of quench are described in the following sections.

1.3.1 Degradation and training

We have already seen that superconductors can carry a maximum current J_c, over which a transition occurs, despite they have null electrical resistivity. Critical current can be measured on short cable samples. But when cables are arranged in coil windings, coils never reach the performances measured on the short sample, and a quench occurs at a current less than the nominal critical current: this phenomenon is called *degradation*. It is mainly due to defects and micro-breakages that occur in cables when they are wound. In addition to degradation, a magnet is always subjected to another phenomenon called *training*: suppose to energize a magnet for the first time, and a quench occurs at 50% of nominal critical current; at the subsequent charging, the magnet will reach a larger percentage of the critical current, for example 60%, and later a larger percentage again, until settling on a stable percentage (nominal critical current is never reached, because of degradation). A good magnet reaches stable zone in few cycles of cooling-warming, and it reaches at least 85% of the nominal critical current. The training is mainly due to the coils movements under the action of the strong electromagnetic forces that act on the windings: the friction between layers can deliver enough energy to start a quench process. At the subsequent ignition, however, the coil in which quench started is in equilibrium position, so the current can increase until another coil moves, or until critical current is reached.

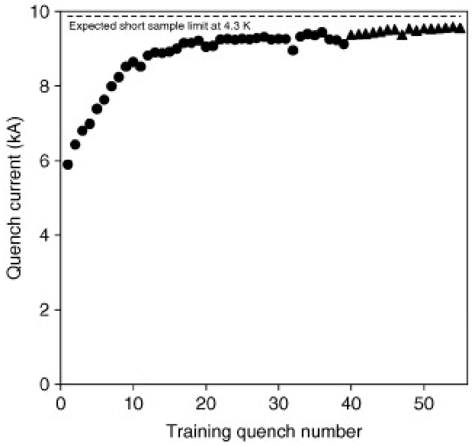

Figure 1.2: Training and degradation example

1.3.2 The disturbance spectrum

Generally, it can be said that every quench event is due to an energy release within the coils, as the field and the current are increased. Temperature locally rises because of this energy, so that the critical current is reduced; when the critical current is equal to the current that flows in the magnet,

Time	**Space**	
	Point	Distributed
Transient	J	J/m^3
Continuous	W	W/m^3

Table 1.3: Disturbance spectrum

heat is produced and a quench could occur. It is so important to know the amount of energy needed to start a quench. It is useful to introduce the *disturbance spectrum* (Tab. 1.3), which encompasses all the energy disturbances that could occur within a superconducting magnet.

Continuous disturbances are caused by a steady power source, that could be due, for example, to a bad joint (point disturbance), or to a.c. and magnetization hysteresis losses (distributed disturbance). Continuous disturbance are usually well known and they do not produce training, but only degradation. They generally do not cause serious problems.

Transient disturbance are instead the dominant cause of degradation and training in magnets, and they may cause serious problems. A type of transient disturbance is *flux jumping*, that is a natural instability of superconducting materials under current variation. This effect can be reduced by decreasing superconducting filaments size, so today it is not a big problem. The mechanical movements are so the main problem. It is obviously impossible to predict and prevent them.

In the next sections we will calculate relationships between quenching current and disturbance size, in order to predict the minimum energy release that can cause a quench, and the temperature rise of the zone in which quench starts.

1.3.3 Distributed disturbances

If an energy release occurs in a large zone of the windings, its temperature rise will be determined only by its heat capacity

$$\partial T = C\partial Q \tag{1.1}$$

where T is the temperature, C the heat capacity, and Q the absorbed heat. At very low temperature, heat capacity strongly depends on the temperature, so it is convenient to talk in terms of enthalpy $H(T) = \int_0^T C(T)dT$. Some enthalpy plot examples are reported in fig. 1.3 (image from [1]).

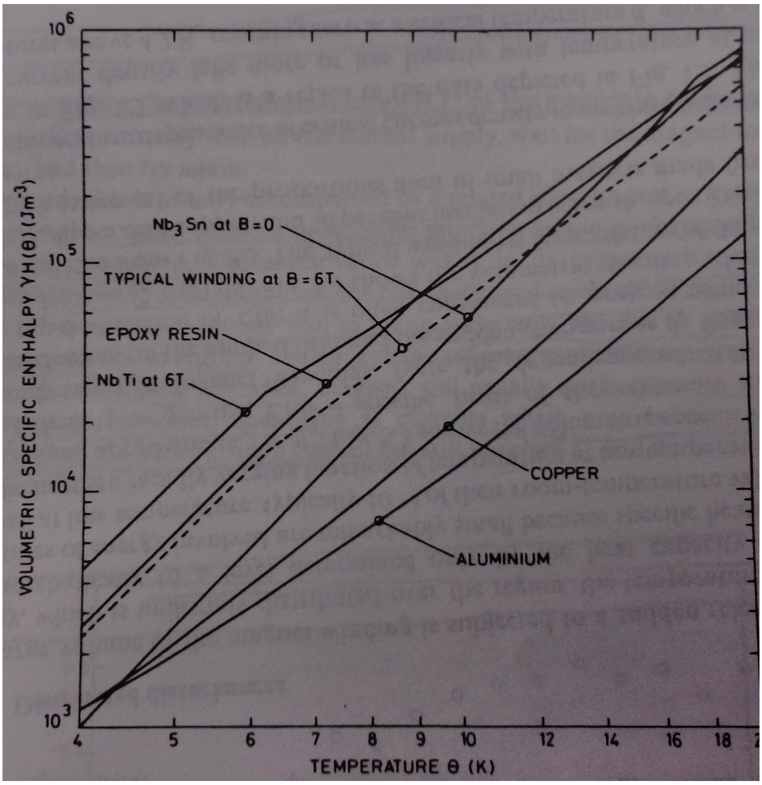

Figure 1.3: Critical current as function of the temperature

$$\partial T = \frac{\partial H}{c_p} \tag{1.2}$$

Suppose that the critical current linearly depends on temperature, as shown in Fig. 1.4. If T_0 is the coolant temperature, it is clear that if the corre-

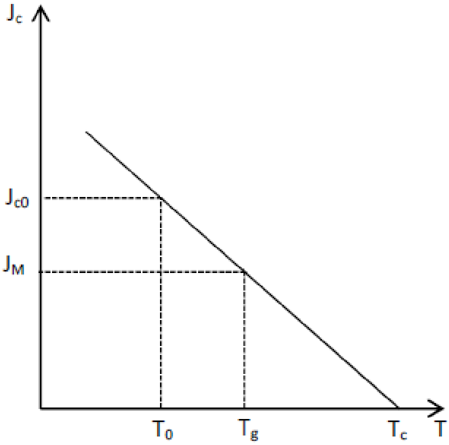

Figure 1.4: Critical current as function of the temperature

sponding critical current J_{co} flows in the cables, the lowest release of energy will develop a quench, because temperature rise makes the current higher than critical current. For this reason, as margin of safety, a sub-critical current J_M flows in the conductors. You can see in Fig. 1.4 that the temperature at which the heat generation starts is given by

$$T_g = T_c - (T_c - T_0)\frac{J_M}{J_{c0}} \tag{1.3}$$

You can use equation 1.3 and data from “typical winding” in Fig. 1.3 in order to estimate the energy needed to reach T_g. For example, an energy of only $750\frac{J}{m^3}$ is needed to reach T_g at the 90% of the nominal critical current at a helium temperature $T_0 = 4.2\ K$; this is a very small release of energy, that would raise the winding temperature by only $10^{-4}\ K$ at room temperature.

1.3.4 Point disturbances and MPZ

Consider a hot spot at temperature T_c. This spot is normal, and it generates a heat power equal to $J_c^2 \rho A l$, where ρ is the normal state resistivity, A the cross-section area of the wire, and l the normal zone length. Under balance, the power generated is equal to that conduced along the wire, according to the Fourier equation

$$\frac{P}{A} = -k\frac{\partial T}{\partial x} \tag{1.4}$$

where k is the longitudinal heat conductivity. We could assume that the temperature rise is linear, so equation 1.4 becomes

$$J_c^2 \rho A l = 2kA\frac{(T_c - T_0)}{l} \tag{1.5}$$

and so

$$l = \left[\frac{2k(T_c - T_0)}{J_c^2 \rho}\right]^{\frac{1}{2}} \tag{1.6}$$

A normal zone longer than l will grow, because heat generation hangs over heat conduction; otherwise, a normal zone smaller than l will collapse and superconductivity will be restored. For these reasons, l is called *Minimum propagating zone* (MPZ). Energy needed in order to establish the MPZ is very small: for example, in a $NbTi$ wire of 0.3 mm diameter cooled with boiling helium ($T_0 = 4.2\ K$) MPZ is only 0.5 μm and the energy needed to origin a quench is only 10^{-9} J, when a current J_c flows inside it. Therefore, wire composed of only superconductor cannot be used, in practice, because they are vulnerable to the slightest disturbance. Composite conductors have been developed in order to improve cables and magnets performances.

1.3.5 Composite conductors

Superconducting wires have a complex cross-section structure [2]. Generally, very thin superconducting filaments of $\sim$ 10 μm diameter are organized in a copper (or a good conductor) matrix. Sometimes, a copper nucleus protected by a tantalum barrier is present. Fig. 1.5 reports some superconducting wires examples. The presence of copper enlarges the conductivity and reduces the resistivity when the quench occurs (when there is no quench all the current goes into the superconductor, otherwise it flows in the copper), so these wires are more resistant to disturbances.

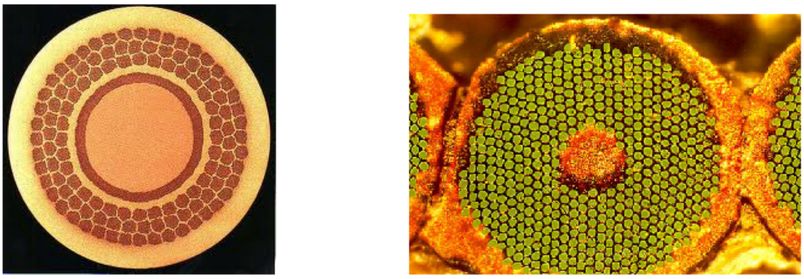

Figure 1.5: Cross section of modern superconductors. On the left you can see the tantalum barrier

Clearly, a one-dimension calculation for the MPZ as in the section 1.3.4 is not suitable, because the wire is very anisotropic. A three-dimension calculation can be carried on. The result is that the MPZ is an ellipsoid elongated in the direction parallel to the wire. This shape is due to the fact that in the longitudinal direction copper heat conductivity is dominant, while in the transversal direction superconductor heat conductivity is dominant. Details on the calculations can be found in [1].
These kind of wires needs higher energy release in order to establish MPZ, of the order of $\sim 10^{-5} J$; nevertheless, this energy is yet very small, therefore a quench can always occur and magnets always need a suitable quench protection system.

1.4 Quench propagation

When a quench occurs, accelerator magnets have to dissipate in heat a very high energy $\frac{1}{2}LI^2$, because they generally have large inductance, and they carry high current. In the previous section we have seen that generally a quench is caused by point disturbances. If the quench propagation is slow, all the energy is dissipated in a very small zone, and the temperature could rise until damaging the magnet. To prevent this situation, it is important to analyze the temperature rise of the normal zone and the quench propagation velocity.

1.4.1 Temperature rise and MIITs

During a quench, the normal zone expands with time because of the heat conduction. Clearly, the zone where the quench starts has the highest temperature, so we will call it the *hot spot.* In order to protect the magnet, it is important to maintain the hot spot temperature under a suitable level. For the calculation of the hot spot temperature, we can assume local adiabaticity; obviously this is a tricky approximation, because quench couldn't propagate, but the error is conservative, so we can accept it.
If we assume local adiabaticity, all the energy per unit volume generated for joule effect is absorbed by the specific heat

$$J^2(t)\rho(T)dt = \gamma C(T)dT \tag{1.7}$$

where ρ is the resistivity, γ the density and C the specific heat. Multiplying for the square section area of the wire, dividing for the resistivity and integrating we obtain

$$\int_0^t I^2(t)\,dt = \int_{T_0}^T \frac{\gamma C(T)}{A^2\rho(T)}\,dT \tag{1.8}$$

Dividing the integral on right in 1.8 for 10^6, we obtain an important quantity called *MIITs.*

$$MIITs(T) = \int_{T_0}^T \frac{\gamma C(T)}{10^6 A^2\rho(T)}\,dT \tag{1.9}$$

The name MIITs is due to the measure unit, that is MA^2s. This quantity is very important because it depends only on the material properties and on the section of the wire. If we know them, we can plot the MIITs vs temperature function. Then, if we know the $I^2(t)$ function, we can integrate it, calculate MIITs developed, and find on the MIITs plot the temperature

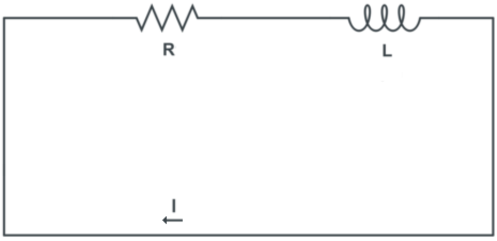

Figure 1.6: Simple protection circuit for a superconducting magnet

that the hot spot has reached. For example, consider the ciruit in Fig. 1.6. The magnet is represented by its inductance, and there is an external resistance R to dissipate the energy when it is extracted from the circuit. We are neglecting the resistance developed by the quench. Clearly, the starting current I decays according to the equation

$$I(t) = Ie^{-\frac{Rt}{L}} \tag{1.10}$$

The integral on left in the equation 1.8 is equal to

$$\int_0^t I^2(t)\, dt = I^2 \frac{L}{2R} \left(1 - e^{-2\frac{Rt}{L}}\right) \tag{1.11}$$

If we use some typical values, such as $I = 10\,\mathrm{kA}$, $L = 0.1\,\mathrm{H}$, $R = 0.05\,\Omega$, $t = 20\,\mathrm{ms}$, we obtain $MIITs \simeq 100$. If we know the material properties, and so the MIITs vs temperature function, we can find the temperature corresponding to 100 MIITs. In this way we can estimate the hot spot temperature.

1.4.2 Quench propagation velocity

Once a quench has started, the normal zone will propagate in three directions under the actions of heat conduction and heat generation. In order to protect the magnet, it is important to analyze the quench propagation

velocities. For details on the calculation refer to [1].
As you can see in Fig. 1.4, if a current J_M flows in the wires, the heat generation starts when the temperature is T_g, and the current starts splitting between copper and superconductor. In this way current in excess flows in the copper and heat is generated, and the superconductor maintain its state, but with a lower flowing current. This process continues until the temperature is T_c, and all the current flows in the copper. The power generation function is represented in Fig. 1.7. We could assume that power

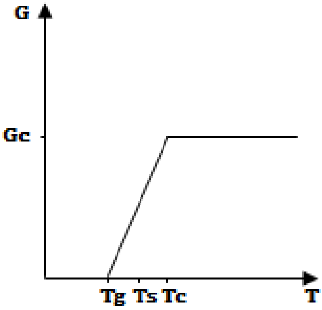

Figure 1.7: Power generation in a composite superconductor

$G = G_c$ is generated when temperature exceeds $T_s = \frac{T_g+T_c}{2}$, and there is not power generation under T_s. Under this approximation, the normal zone has a boundary with temperature T_s which travels with velocities v_L in the longitudinal direction, and v_T in the transversal direction. Under adiabatic approximations, you can prove that the longitudinal propagation velocity is

$$v_L = \frac{J}{\gamma C}\left(\frac{\rho k}{T_s - T_o}\right)^{\frac{1}{2}} \tag{1.12}$$

About the transversal propagation velocity, the only differences are on the thermal conductivity and on the specific heat. It's clear that in the longitudinal propagation almost only the copper is involved, otherwise in the transversal direction the superconductor and the insulation are involved, too. So, the ratio between the two propagation velocity is

$$\frac{v_T}{v_L} = \frac{C_{avm}}{C_{av}} \left(\frac{k_T}{k_L}\right)^{\frac{1}{2}} \tag{1.13}$$

where C_{avm} is the specific heat averaged only on the metallic components, C_{av} is the specific heat averaged on the whole wire cross section.Typically, the longitudinal propagation is 100-200 times faster than the transversal one.

This model is strongly approximated, but it gives indications on the quantities involved in the quench propagation.

1.5 Quench protection

Accelerator magnets generally work at almost the highest performances that they can reach. It is so clear that a quench can always occur, and magnets are in danger without a suitable protection. There are many techniques developed in order to protect magnets, we are going to describe some of them.

1.5.1 Quench detection

The first question to answer is how to detect a quench. When a quench starts, the normal zone grows with the propagation velocities indicated in the section 1.4.2. It is clear that the magnet resistance grows, too, therefore between the ends of the magnet a voltage $V(t) = R_q(t)I_0$ can be measured, and this voltage rises with time. So, in order to detect a quench you can measure the voltage difference between the ends of the magnet: when the voltage overcomes a certain threshold a quench is detected and the protection can start.

1.5.2 External dumping resistance

The simplest way to protect a magnet is by means of an external resistance: consider the circuit in Fig. 1.8. When the magnet is superconducting, the

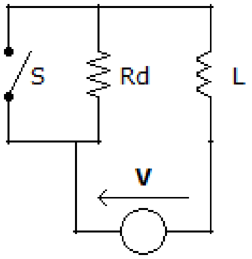

Figure 1.8: Protection system with external dumping resistance

switch is closed. When a quench is detected, the switch is immediately opened and the current starts to decay. Neglecting the normal zone resistance, a number of MIITs equal to

$$MIITs = I_0^2 t_d + \int_{t_d}^{t} I_0^2 e^{\frac{Rd}{L}t}\, dt \tag{1.14}$$

is developed. t_d is the time needed to reach the voltage threshold for the quench detection plus an eventual delay for the switch opening, and an eventual validation time (needed in order to avoid false quench detections caused by voltage spikes due to instabilities of the superconductor). Clearly, this time depends on the quench propagation velocities: the faster is the propagation, the faster the switch is opened and the resultant hot spot temperature is lower. It is therefore important to maintain t_d as low as possible.

The integral in the equation 1.14 depends on the dumping resistance. The current fall is faster whit a high R_d, and a minor number of MIITs is developed. So, with very high dumping resistance you should be able to carry the current to 0 in a very small time, and so to maintain the hot spot temperature under a suitable level. The problem is that accelerator magnets have high inductance, so high voltage $V = L\dot{I}$ is generated between windings, and a high voltage $V = R_d I$ appears between the magnet ends. Therefore the dumping resistance value is limited by the maximum voltage supported by the magnet. Generally, voltages over ~ 1 kV can break the insulation and damage the magnet.

Protection with only dumping resistance is possible in small magnets, in some cases, because the propagation velocities are high enough to "help" the current decay by means of the resistance developed by the quench. This never happens in large Nb_3Sn accelerator magnets.

1.5.3 Quench heaters

We just said that in large Nb_3Sn accelerator magnets the dumping resistance cannot protect the magnet alone. Protection is therefore completed by means of the *quench heaters*. Quench heaters are resistive strips, usually aluminum sheets, in direct thermal contact with the coils, all along the magnet. When a quench is detected, heaters are immediately fired and generate heat. In this way, after a certain time t_{QH}, due to the heat diffusion in the insulation, almost all the magnet is resistive. The energy is dissipated on a larger volume, and the coil resistance R_c makes the current fall faster. The MIITs developed are

$$MIITs = I_0^2 t_d + \int_{t_d}^{t_{QH}} I_0^2 e^{\frac{Rd}{L}t}\,dt + \int_{t_{QH}}^{t} I^2(t)\,dt \tag{1.15}$$

In this way the hot spot temperature can be maintained under a safe level.

Chapter 2

Differential inductance and Inter-Filament Coupling Currents

As we have seen in section 1.5, one of the main parameters involved in the quench protection of a superconducting magnet is the inductance. Therefore, in order to have a reliable prediction of the hot spot temperature, it is important to have tools able to compute exactly the inductance of a magnet; this is true in particular in the design phase, when inductance measurements are not possible. There are many computational tools which can compute inductance of magnets; however, in this section it is shown that using the standard inductance (measured or computed with usual tools) is not correct for the simulation of a quench, when the current decays very fast ($\sim$ 100 kA/s). This fact is justified by the Inter-Filament Coupling Currents (**IFCC**), which affect the differential inductance of a superconducting magnet.

2.1 Experimental motivation

For the development of HiLumi LHC [3], in the USA the project LARP [4] has started; more details on these activities can be found in the chapter 3. One of the prototype magnets developed by LARP is HQ [5], a superconducting Nb_3Sn quadrupole magnet. Some of the protection tests planned at Fermilab in 2013 [6] aimed to look at the effect of high ramp rate on the magnet. For this reason, the magnet has been short-circuited on a high dump resistor, in order to reach very large dI/dt ($\sim$ 100 kA/s). The circuit is therefore a simple L-R circuit, and a simple exponential current decay is expected

$$I(t) = I_0 e^{-\frac{t}{\tau}} \tag{2.1}$$

$$\tau = \frac{L}{R_d} \tag{2.2}$$

where L is the magnet inductance, and R_d is the dumping resistance. It is easy to understand that such a test should be very simple to simulate, because there is not the complication of the quench resistance, and the circuit solution is very simple. But, as seen in Fig. 2.1, using a simple exponential the experimental decay cannot be predicted well.

The dumping resistance is obviously well known. A possible explanation could be that there is some magnet resistance missing in the simulation; nevertheless, in this test there is not spontaneous quench, and quench heaters are not fired, which means that magnet resistance could arise only from AC losses within the windings.

AC losses are due to the eddy currents which circulates in the copper matrix between filaments, or which go through the insulation of the superconducting cables, generated by the field change. These currents dissipate some energy into heat, and can induce a quench; but, they need roughly 10-20 ms to make the cables reach the critical temperature. This means that, at least at the beginning of the decay, the pure exponential should describe well the experimental curve, but this does not happen, as Fig. 2.1 shows. The only possible explanation is therefore that the magnet inductance is

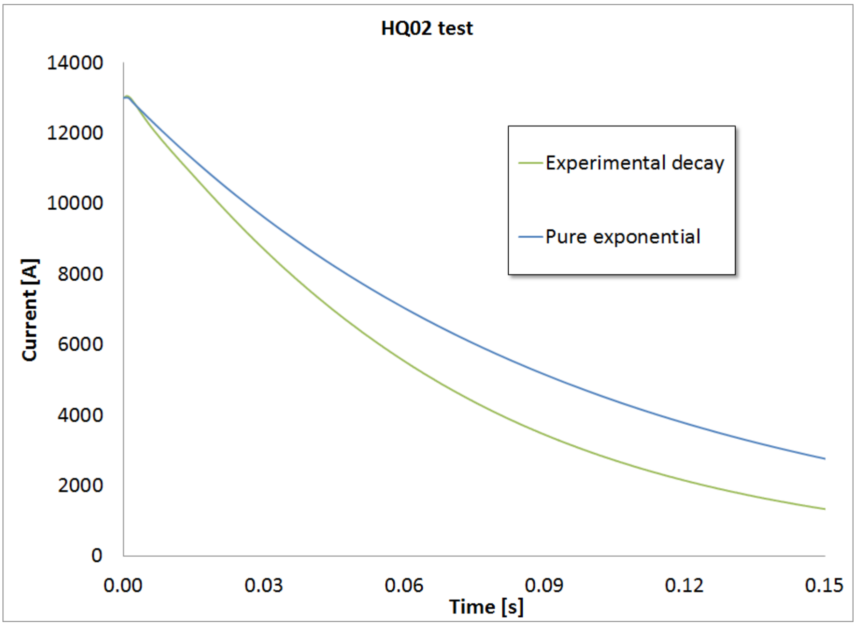

Figure 2.1: Comparison between the current decay from a fast extraction test on HQ and a pure exponential with decay time $\tau = \frac{L}{R_d}$

not correct, even if the inductance used for the simulation is experimentally measured [7] and agrees with the simulated values. Therefore it is necessary to find an explanation of the discrepancy between the inductance measured experimentally and the one inferred by the current decay showed in Fig. 2.1.

The same phenomenon can be seen also in other tests [8] [9] performed in other magnets developed by the LARP collaboration. In the next sections, it will be shown that using the inductance measured at low ramp rate, such as the one used for HQ, is wrong, and that the differential inductance of superconducting magnets is affected by the coupling currents between the filaments.

2.2 Differential inductance

First of all, the concept of differential inductance is introduced here. The standard inductance is defined as

$$L_s = \frac{\Phi(B)}{I} \tag{2.3}$$

where $\Phi(B)$ is the field flux, and I is the current. When the flux is linear with the current, the inductance of a magnet is constant. In order to compute the current decay during a quench, the voltage across the magnet has to be computed in order to solve the Ohm equation. In this simple case, the inductive voltage across the magnet under current changes is

$$V = -L_s \frac{dI}{dt} \tag{2.4}$$

However, generally the field flux of a magnet is not linear, for example because of the iron saturation. For this reason, the voltage across the magnet is not given by the equation 2.4. In fact, using equation 2.3 and the Faraday-Neumann-Lenz law 2.5, one can obtain the equation 2.6.

$$V = -\frac{d\Phi(B)}{dt} \tag{2.5}$$

$$V = -\left(L_s + \frac{dL_s}{dt} I\right) \frac{dI}{dt} \tag{2.6}$$

It is therefore useful to define the differential inductance L

$$L = \left(L_s + \frac{dL_s}{dt} I\right) \tag{2.7}$$

Combining equation 2.6 and 2.7, the inductive voltage across the magnet is given by

$$V = -L \frac{dI}{dt} \tag{2.8}$$

which is very similar to the equation 2.4. Combining equation 2.8 and 2.5, one can obtain another definition of the differential inductance

$$L = \frac{d\Phi(B)}{dI} \tag{2.9}$$

It is important to point out that differential inductance and standard inductance are two separate quantities with different meanings: standard inductance is related to the total field flux amount, while differential inductance is related to the field flux derivative, and it is the one to take into account in the solution of the circuit, for example during a quench; they coincide only when the field flux is linear.

2.2.1 An example: iron saturation

A typical example of the role of differential inductance in magnets is the iron saturation. Fig. 2.2 shows an hypothetic magnet where part of the field flux is given by coils (linear with current), and part by iron (up to 2 T). It is easy to note that at high current the iron makes the standard inductance larger, while the differential inductance is basically the same, because the two curves are almost parallel; instead, at low current, the differential inductance is larger because of the iron.

2.2.2 Differential inductance in magnetized materials

Such as the iron, every magnetized material affects the differential inductance of a magnet. The field within the material is given by

$$B = \mu_0(M + H) \tag{2.10}$$

the magnetization M can be seen as

$$M = \chi H \tag{2.11}$$

where χ is the susceptibility. Then, equation 2.10 becomes

$$B = \mu_0(1 + \chi)H \tag{2.12}$$

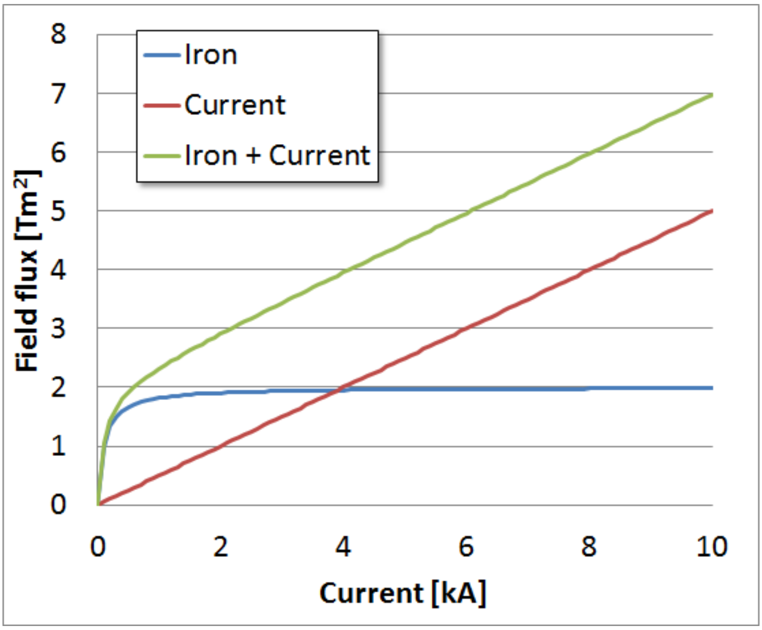

Figure 2.2: Hypothetic field flux in a magnet. Red curve represents the field given by the coils, the blue curve the one given by the iron, the green curve the total flux.

The magnetic energy density per volume unit variation under field changes is

$$du = MdB \tag{2.13}$$

Combining equation 2.12 and 2.13, one obtains

$$du = \mu_0 H dH + \mu_0 \chi H dH + \mu_0 H^2 d\chi \tag{2.14}$$

The total energy variation per unit time is

$$\frac{dU}{dt} = -VI \tag{2.15}$$

Equation 2.15, combined with equations 2.5 and 2.9, gives another definition for the differential inductance

$$L = \frac{1}{I}\frac{dU}{dI} \tag{2.16}$$

Differential inductance is therefore related to the total energy variation. Now, using equation 2.14 and 2.16, one obtains

$$L = \int \left[\frac{\mu_0 H}{I}\frac{dH}{dI} + \frac{\mu_0 \chi H}{I}\frac{dH}{dI} + \frac{\mu_0 H^2}{I}\frac{d\chi}{dI} \right] d\Gamma \tag{2.17}$$

where Γ is the volume.
In conclusion, the differential inductance, when magnetization phenomena are present, can be obtained from the equation 2.17, where the first term has to be integrated in the whole volume, while the second and third terms have to be integrated in the magnetized material volume. Therefore, known the magnetic field and the susceptibility, one can compute the differential inductance of a magnet using this integral relation.

2.3 An electro-magnetic model describing Inter-Filament Coupling Currents (IFCC)

2.3.1 IFCC as magnetization currents

As we have seen in section 1.3.5, superconducting strands are arranged in a copper matrix. For this reason, under field changes eddy currents circulate and go through the matrix, dissipating part of the stored energy into heat. But this is not the only effect of these currents; in fact, also the magnetic field at whom the strand is subjected is modified by the inter-filaments coupling currents (IFCC). It can be proved that the field B_i within a strand, when IFCC are present, follows the equation [1]

$$B_i = B_e - \frac{dB_i}{dt}\tau \tag{2.18}$$

where B_e is the external field, and τ is the IFCC decay times constant, given by

$$\tau = \frac{\mu_0}{2\rho_e}\left(\frac{p}{2\pi}\right)^2 \tag{2.19}$$

In equation 2.19, p is the filament twist pitch length, ρ_e is the effective transverse matrix resistance. Details on how to compute the effective transverse resistivity and the coupling currents can be found in the chapter 8 of [1]. In practice, considering the copper resistivity and a typical twist pitch length of 10-20 mm, one obtains that typical values of the IFCC decay time is τ=10-100 ms, depending on the temperature and on the magnetic field.

From direct integration of the current, the magnetization associated to IFCC can be computed

$$M = \frac{2\lambda\tau}{\mu_0}\frac{dB_i}{dt} \tag{2.20}$$

where λ is the packing factor, which takes into account that M is an uniform magnetization on the whole strand, but filaments are arranged in a reduced area (see for example Fig. 1.5); λ is the ratio between that area and the strand area, and typically it is ≤ 0.8. Therefore, because of the IFCC, coils can be considered as a magnetized material with magnetization M given by equation 2.20, such as, for example, the iron. It can be so expected that differential inductance is affected by the IFCC.

From equation 2.12, the susceptibility related to IFCC can be obtained

$$\chi = -\frac{1}{1+\frac{1}{2\lambda}\left(\frac{1}{1-B_e/B_i}\right)} \tag{2.21}$$

It is therefore clear that, using equation 2.17, it is possible to compute the differential inductance of a magnet taking into account the presence of IFCC in the strands, provided that the equation 2.18 can be solved in our problem. In fact, IFCC are basically screening currents, which tends to maintain constant the field flux (and, dealing with superconductivity, they are even more efficient in doing it), therefore it can be expected that the differential inductance is lower when this phenomenon occurs, while it tends to its nominal value when coupling currents decay.

In this section, we have seen that in principle it is possible to compute the differential inductance of a superconducting magnet when IFCC are present. In the next sections, we will look at how calculating differential inductance in some practical cases.

2.3.2 Exponential approximation

In order to obtain the susceptibility related to IFCC from the equation 2.21, it is needed to compute the field B_i from the equation 2.18. In order to do it, we can assume that the external field has an exponential behavior, such as

$$B_e = B_0 e^{-\frac{t}{\tau_e}} \tag{2.22}$$

where τ_e is the transport current decay time. With this assumption, the equation 2.18 can be solved together with the boundary condition

$$B_i(0) = B_e(0) = B_0 \tag{2.23}$$

which assume that the IFCC are not yet effective at the beginning of our problem, and therefore the internal field is obviously equal to the applied field. Together with this condition, the equation 2.18 is a Cauchy problem, which can be written as

$$\begin{cases} \dot{B}_i(t) + \frac{B_i(t)}{\tau} = \frac{B_e(t)}{\tau} \\ B_i(0) = B_0 \end{cases} \tag{2.24}$$

The solution of this Cauchy problem is well-known, and it is

$$B_i(t) = e^{\int_0^t \frac{dt}{\tau}} \left[B_0 + \int_0^t \frac{B_e(t)}{\tau} e^{-\int_0^t \frac{dt}{\tau}} dt \right] \tag{2.25}$$

Using equation 2.22, the equation 2.25 can be solved

$$B_i = \frac{B_0}{\tau - \tau_e} \left(\tau e^{-\frac{t}{\tau}} - \tau_e e^{-\frac{t}{\tau_e}} \right) \tag{2.26}$$

Now, we have the internal field at whom a strand is subjected when IFCC are present, and the appield field decay exponentially such as in equation 2.22. At this point, the susceptibility related to the IFCC can be calculated using equation 2.21. The result is

$$\chi(t) = \frac{2\lambda\tau\left(e^{-\frac{t}{\tau_e}} - e^{-\frac{t}{\tau}}\right)}{\tau e^{-\frac{t}{\tau}} - \tau_e e^{-\frac{t}{\tau_e}} - 2\lambda\tau\left(e^{-\frac{t}{\tau_e}} - e^{-\frac{t}{\tau}}\right)} \tag{2.27}$$

In principle, at this point one should be able to compute the differential inductance using equation 2.17, provided that the magnetic field $H(I)$ is known, and using the relation

$$\frac{d\chi}{dI} = \frac{1}{\frac{dI}{dt}}\frac{d\chi}{dt} \tag{2.28}$$

This approach is useful for problems in which the current, and therefore the applied field, is driven, in our case into in an exponential way. Using a similar approach, one could compute the differential inductance considering IFCC during a ramp-up or a ramp-down (field linear with the time), or during sinusoidal oscillation of the transport current. By the way, during a quench the power supplied is disconnected from the circuit, therefore the applied field is not known, but it has to be calculated together with the internal field. This approach therefore could seem not useful for a quench calculation; nevertheless, in the next sections we will see how to implement the exponential approach into a quench software.

This approximation is also useful to understand the fact that, during a quench, the inductance of a magnet has to be considered as an unknown of the problem: we have seen that it depends on a transient phenomenon (IFCC), which depends on how the current decays (τ_e in equation 2.22); but, obviously, also the current depends on the inductance ($\tau_e = L/R$). The conclusion is that, considering IFCC effect on the inductance, or whatever transient magnetization phenomenon, both the inductance and the current have to be computed in order to simulate a quench; it has not to be expected to have a current dependent function of the inductance to use as input in a quench software.

2.3.3 Implementation in QLASA

QLASA [10] is a semi-analytical quench simulation software. The main purpose of this program is the simulation of the quench propagation in superconducting solenoids; however, with some precautions, it is suitable to simulate quench in any superconducting magnet [11]. The quench propagation velocities are computed analytically following [1], while the temperature is calculated using the adiabatic heat equation

$$\gamma C_p dT = \rho J^2 dt \tag{2.29}$$

where γ is the mass density (kg/m^3), C_p the specific heat (K/J), ρ the electrical resistivity (Ω) and J the transport current density (A/mm^2). The current decay is calculated solving the circuit equation in a step-by-step method. The flow-chart of the program is shown in Fig. 2.3. The circuit implemented in QLASA is represented in Fig. 2.4, where the magnet is represented by its inductance L, R_q is the quench resistance, R_d is the dump resistance.

In order to compute the current decay, the equation to be solved is

$$[R_d + R_q(t)]\, I(t) + L(t)\frac{dI(t)}{dt} = 0 \tag{2.30}$$

The quantities R_q and L are time dependent, nevertheless, at each time step they are considered constant; then, at the following time step, the two quantities are computed again and used in order to calculate the new current. It is easy to understand that, under these assumptions, the solution of the circuit is a current decay composed by a series of small exponential decays bounded together, with different decay time at each time step. It is therefore understandable that the exponential approximation presented in section 2.3.2 is useful to compute the differential inductance $L(t)$ considering the effect of inter-filament coupling currents. The new time dependent quantity, the magnetic susceptibility, has to be implemented in the code, following equation 2.27; this quantity has to be calculated at each time step, considering that

$$\tau_e(t) = \frac{L(t)}{R_q(t) + R_d} \tag{2.31}$$

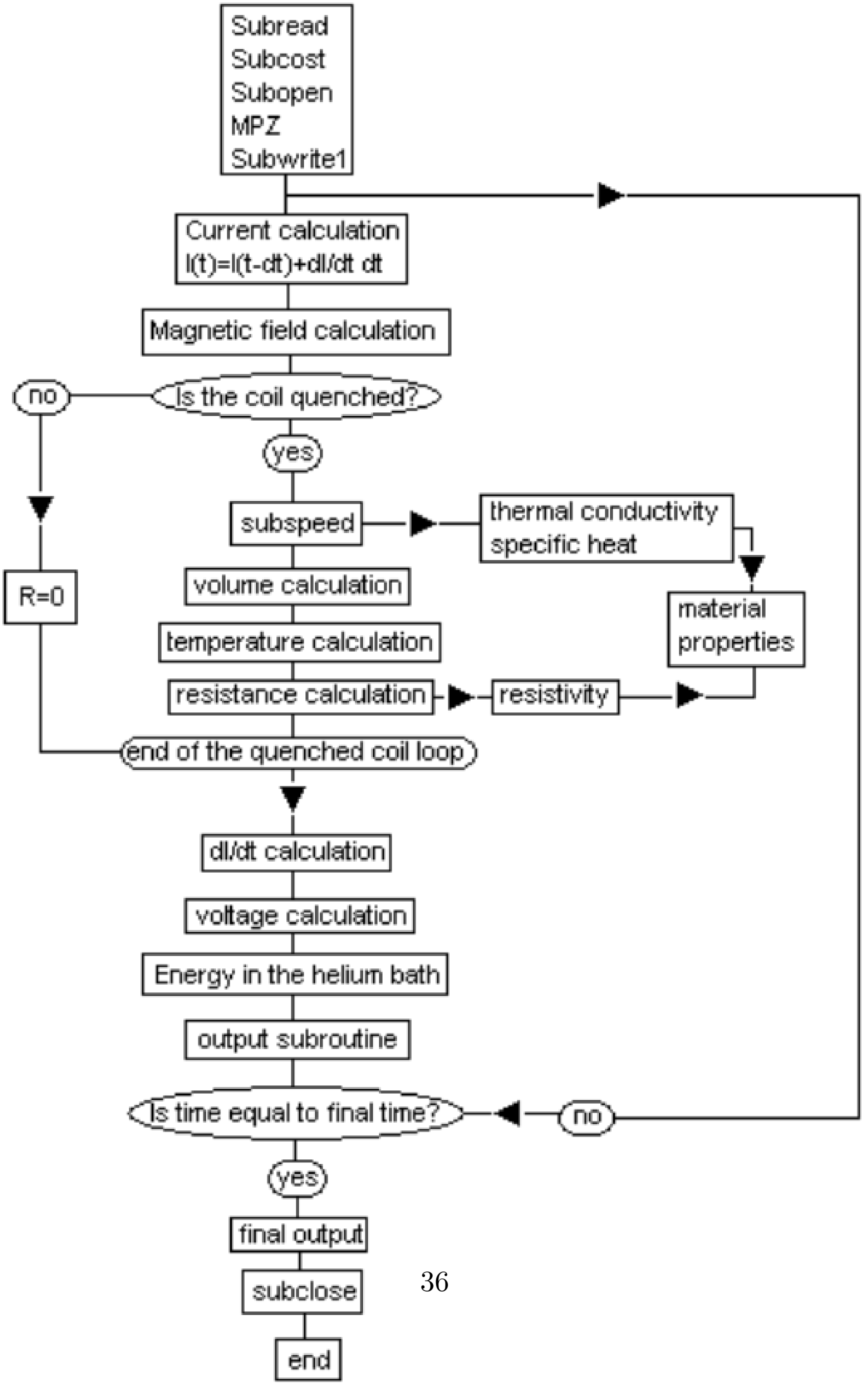

Figure 2.3: Flow-chart of QLASA

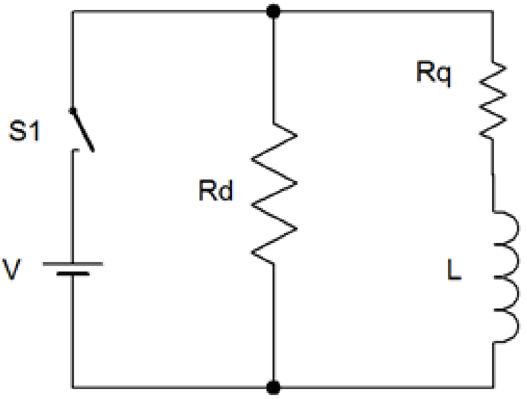

Figure 2.4: Circuit implemented in QLASA

The susceptibility can be used in order to compute the inductance following equation 2.17; then, this inductance is used in order to compute the new current at the following time step, the quench resistance is calculated again, and the new τ_e can be used in order to compute again the susceptibility and the inductance, and so on until the current goes to 0. This is a very simple way to implement the model showed in section 2.3.2, which could be implemented easily in any quench simulation software.

2.3.4 Differential inductance variation

Looking at equation 2.17, the question to answer is now: how to compute the integral? In order to answer, we will make a strong assumption: the magnetic field produced by the coils is not affected by the inter-filament coupling currents. It is obvious that the coupling currents modify the magnetic field within the coils; in particular, they are basically screening currents, therefore they tend to maintain constant the field under current changes. It is therefore understandable that the slope of the field flux curve has a minor slope, and that the differential inductance, defined as in equation 2.9, be-

comes lower. However, inter-filament currents are a transient effect, which can change significantly the derivative of the flux (and so the differential inductance), but only for a certain time (typically, the screening currents decay time), therefore the field flux amount can change only of few percents. This justify the assumption of considering the field unchanged.
In this condition, the equation 2.17 can be split in two parts:

$$L = L_s + \Delta L \tag{2.32}$$

where

$$L_s = \int \frac{\mu_0 H}{I} \frac{dH}{dI} d\Gamma \tag{2.33}$$

and

$$\Delta L = \int \left[\frac{\mu_0 \chi H}{I} \frac{dH}{dI} + \frac{\mu_0 H^2}{I} \frac{d\chi}{dI} \right] d\Gamma \tag{2.34}$$

L_s represents the static inductance, i.e. the inductance which can be computed neglecting any magnetization or transient effect. This number can be easily computed or measured with standard methods. Instead ΔL represents the inductance variation due to a transient or magnetization effect, such as inductance, or iron saturation. Considering that the only volume dependent quantity is the magnetic field, the equation 2.34 can be written as

$$\Delta L = \frac{\mu_0 I}{2I} \frac{d}{dI} \int H^2 dV + \frac{\mu_0}{I} \frac{d\chi}{dI} \int H^2 d\Gamma \tag{2.35}$$

This approximation is very useful, because we have seen that now we can talk of inductance *variation*; this means that, in our quench software, we do not have to totally modify the inductance modelling, but we can just add a correction to the inductance that we have ever used as input using the equation 2.35. The magnetic susceptivity is given by equation 2.27, and its derivative can be computed as

$$\frac{d\chi}{dI} = \frac{1}{\frac{dI}{dt}} \frac{d\chi}{dt} \tag{2.36}$$

The magnetic field within the coils can be obtained easily using FEM codes, such as ROXIE [12] [13], then it can be integrated numerically. We can now

compute the inductance variation in our quench software, considering the dynamic effects produced by inter-filament coupling currents.
However, we are also interested in a completely analytical solution, which would be very simple to implement in any quench software. In the next sections, we are going to see how to compute the differential inductance in a completely analytical way in some simple cases.

2.3.5 Computation of the inductance of an ideal superconducting quadrupole

The main application of the model presented in the previous sections is the quench protection of accelerator magnets. Typically, accelerator magnets are as ideal as possible n-poles magnets. For this reason, we are going to see how to compute the differential inductance of an ideal superconducting quadrupole, as example.
In general, in a superconducting accelerator magnet, the magnetic field is mostly generated by a current distribution. Iron is used only in the yoke, in order to screen the magnetic field and for mechanical reason, and, as a first approximation, one can assume that it is totally saturated and it adds 2 T to the magnetic field produced by the current. For this reason, the arrangement of the conductors has to be done with care, in order to produce the desired magnetic field.
In order to produce a quadrupole magnetic field, the most convenient current distribution is

$$J(\theta) = J_0 \cos 2\theta \tag{2.37}$$

With such a distribution, it can be proved that an ideal quadrupole magnetic field is produced inside the aperture. It is obvious that this is an ideal case, and that in reality the conductors arrangement has to imitate this distribution in order to be as similar as possible to that. In Fig. 2.5, an example of a superconducting quadrupole cross section is showed.

In order to describe the magnetic field inside and outside the magnet, it

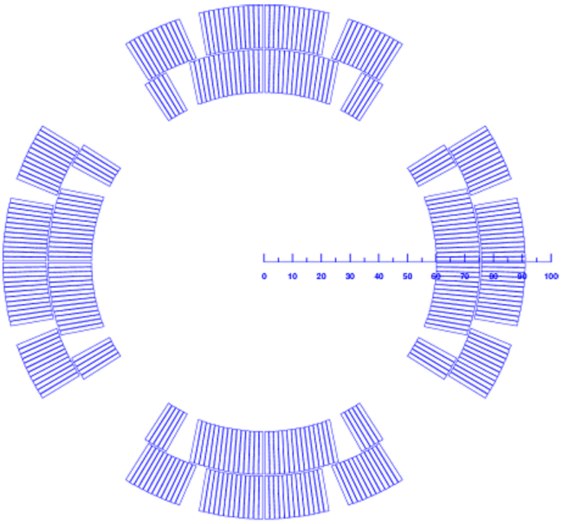

Figure 2.5: Example of the cross section of a superconducting quadrupole

is useful to use the complex notation. The magnetic field is then

$$\begin{aligned}
&B(z) = B_x(z) + iB_y(z) \\
&B^*(z) = B_x(z) - iB_y(z) \\
&z = x + iy
\end{aligned} \tag{2.38}$$

Using this notation, the magnetic field produced by a volumetric current distribution such as the one in equation 2.37 inside the aperture can be written as

$$B^*(z) = i\frac{\mu_0 J_0}{2} z \ln\left(\frac{a_2}{a_1}\right) \tag{2.39}$$

where a_1 and a_2 are the inner and the outer radius of the magnet, respectively, such as indicated in Fig. 2.6 The field produced outside the coils is instead:

$$B^*(z) = i\frac{\mu_0 J_0}{8}\frac{a_1^4 - a_2^4}{z^3} \tag{2.40}$$

Using equation 2.39 and 2.40, it is possible to obtain the analytical field inside the coils: in fact, considering a circumference of radius z within

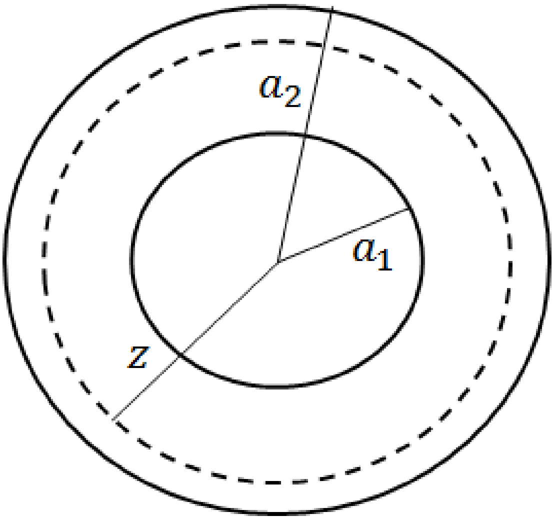

Figure 2.6: Ring representing the coils of a magnetic quadrupole with a $\cos 2\theta$ current distribution

the coils ($a_1 \leq z \leq a_2$) such as the dashed one represented in Fig. 2.6, one can imagine that the field $B^*(z)$ is the sum of the field produced by the part of the coils which is outside the circumference, calculated as in equation 2.40, plus the field produced by the part of the coils which is inside the circumference, calculated as in equation 2.39. The field within the coils is therefore

$$B^*(z) = i\frac{\mu_0 J_0}{2}\left[z\ln\left(\frac{a_2}{|z|}\right) - \frac{1}{4}\frac{|z|^4 - a_1^4}{z^3}\right] \tag{2.41}$$

Using this relation, it is possible to compute the volume integral in equation 2.34. In fact, assuming that the coils are not magnetized, we have that

$$H = \frac{B}{\mu_0} \tag{2.42}$$

and therefore $H^2 = HH^*$ can be easily computed

$$H^2 = \frac{J_0^2}{4}\left[r^2 \ln^2 \frac{a_2}{r} + \frac{1}{16}\frac{\left(r^4 - a_1^4\right)^2}{r^6} - \frac{1}{2}\frac{r^4 - a_1^4}{r^2}\ln\frac{a_2}{r}\cos 4\theta\right] \tag{2.43}$$

where $r = |z|$. The volume integral is therefore:

$$l\int_{a_1}^{a_2}\int_0^{2\pi} H^2 r\, dr\, d\theta = \frac{J_0^2 \pi l}{2}\left\{\frac{3}{64}a_2^4 - \frac{a_1^4}{64}\left[16\left(\ln^2\frac{a_2}{a_1} + \ln\frac{a_2}{a_1}\right) + \frac{a_1^4}{a_2^4} + 2\right]\right\} \tag{2.44}$$

In equation 2.44, J_0 represents the maximum current amplitude in an ideal $\cos 2\theta$. In order to use this result for a real magnet, it is important to relate J_0 to the current flowing in the conductors. This can be done comparing the current density integral on the whole cross sections to the actual current times the winding number, i.e.

$$NI = 2\int_{a_1}^{a_2}\int_{-\frac{\pi}{4}}^{\frac{\pi}{4}} J_0 \cos 2\theta r\, dr\, d\theta = J_0\left(a_2^2 - a_1^2\right) \tag{2.45}$$

where N is the total number of windings, and therefore

$$J_0 = \frac{NI}{a_2^2 - a_1^2} \tag{2.46}$$

Using equation 2.44 and 2.46, and putting them in equation 2.34, it is then possible to compute completely analytically the inductance variation due to the inter-filament coupling currents a in a superconducting quadrupole, assuming that the field within the coil is ideal, and that the coupling currents do not change this field.

With analogous calculations, it is possible to obtain similar results for a dipole, a sextupole, or for any $\cos n\theta$ magnet.

Equation 2.45 thus represents the integral of the magnetic field within the coils of an ideal $\cos 2\theta$ quadrupole. This equation can be combined with equation 2.35 in order to obtain a completely analytical equation for the inductance variation considering the effect of IFCC. Despite the strong assumptions made, this is a very useful tool, because it is easy to implement in an iterative way in every quench simulation software, and to obtain considerable results.

2.3.6 A simple example: discharge on a dump resistor

As a simple example to see the effect of the IFCC on the inductance, we can consider the case of a superconducting quadrupole discharged on an external dump resistor, assuming that no quench resistance is developed. An example like this is the HQ decay already shown in fig. 2.1. It is easy to understand that the the expected current decay is a simple exponential, like:

$$I = I_0 e^{-\frac{t}{\tau_e}} \tag{2.47}$$

We have already seen that this equation does not describe the decay at all, even at the very beginning. Now, without the complication of the quench resistance, it is easy to implement in an iterative way equations 2.27, 2.35 and 2.44 also in a very simple tool like Excel, in order to obtain the current decay considering the effect of coupling current. In fig. 2.7, the comparison of the experimental data and the pure exponential with the decay obtained with our simple model of IFCC is shown, considering a decay time τ for the coupling currents of 15 ms. It is easy to see that, while the pure exponential fails from the beginning to describe the curve, the decay obtained considering the effect of coupling currents on the magnet inductance allows to fit the decay until about 20 ms, using a reasonable average number for the coupling currents decay time (15 ms). In figure 2.8, a plot representing the HQ measured inductance compared with the inductance output of the model is shown: the inductance is even 50% lower at the beginning of the decay, then it saturates to its nominlal value. This explains well why the model is needed in order to fit the decay.

After 20 ms, it is reasonable to expect that a considerable part of the coils is resistive because of quench back, and that our simple assumptions of no quench resistance is not valid; this can easily explain the difference between the experimental curve and the simulated one. In order to add the quench resistance, we need a quench simulation software, such as QLASA; however, the point of this simple example is that effect of inter-filament-coupling-currents on magnet inductance can explain the discrepancy from experimental decay and simulated one at the very beginning, when a quench resistance cannot be considered effective.

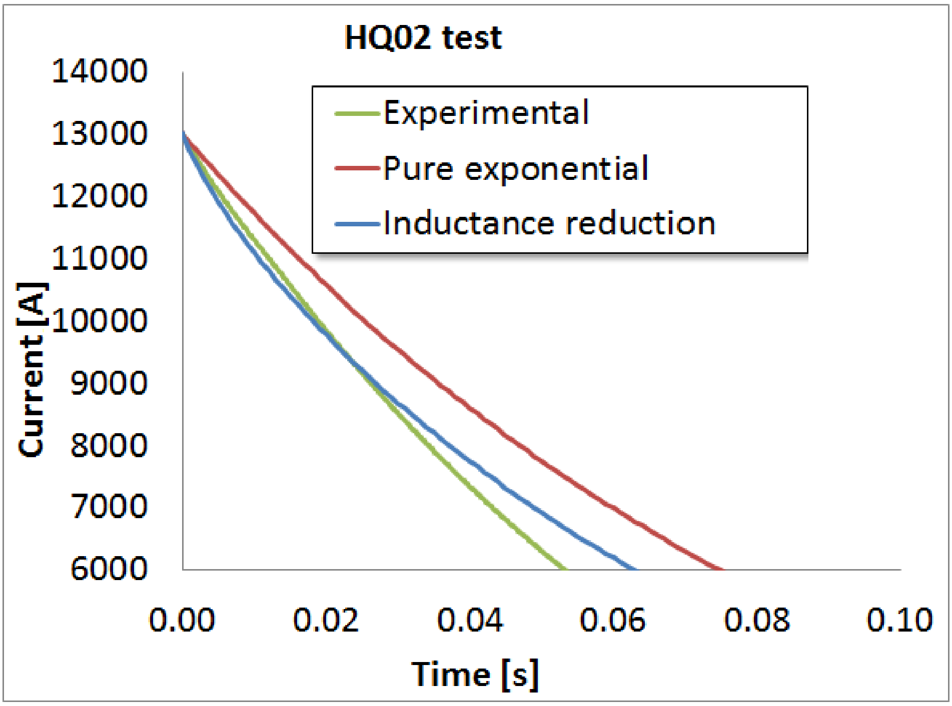

Figure 2.7: Comparison of experimental data (green) from a HQ test with a pure exponential decay (red), and with a decay obtained using the model for the simulation of the effect of inter-filament-coupling-currents on the magnet inductance (blue).

2.3.7 Power from IFCC

Inter-filament coupling currents flow within the strand copper matrix. For this reason, the power dissipated by them should be added to the Joule dissipation in order to solve the heat equation and to obtain the coils temperature during a quench. Using the model described in section 2.3.1, it is very easy to obtain this power, which is just [14]:

$$P_{IFCC} = M\frac{dB_i}{dt} \tag{2.48}$$

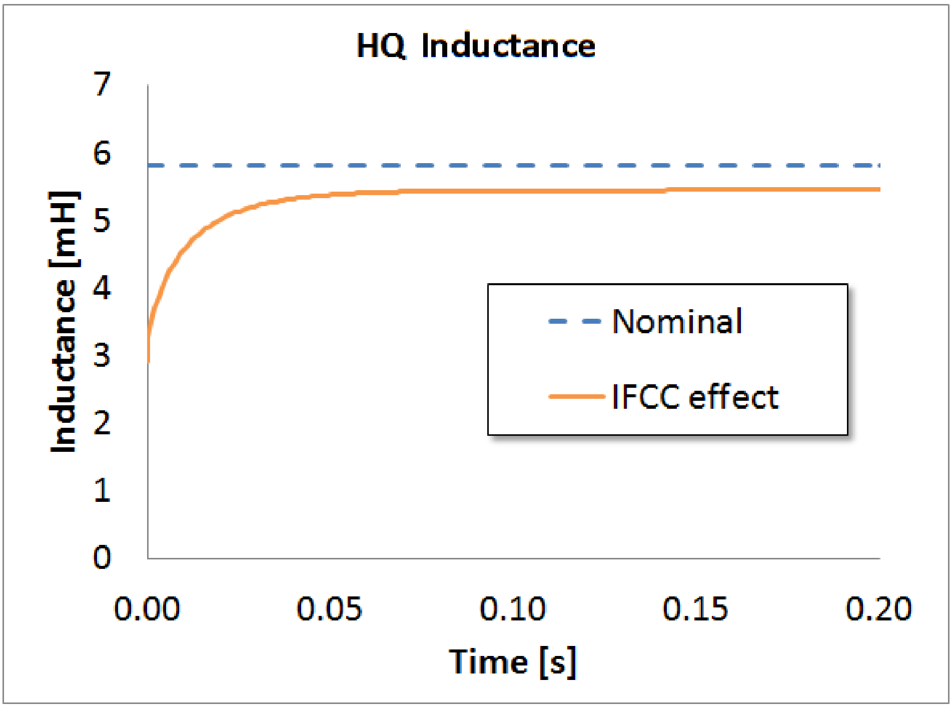

Figure 2.8: HQ measured inductance compared to the inductance obtained considering the IFCC effect

where M is the magnetization due to IFCC, given by equation 2.20, and B_i is the field internal to the strand, given by equation 2.26.
When implementing this in a quench software, it is very important to understand the energy balance involved in the phenomenon of the coupling currents generation. A common error when simulating coupling currents and quench back is adding the power dissipated by them within the coil as an external power source. Instead, the coupling currents are like a coupled circuit, which takes some energy from the main circuit (the coils); therefore, the power used to generate the IFCC, and dissipated within the coils, comes from the magnet itself! This power has to be subtracted to the mag-

HQ main parameters	
Aperture	120 mm
Strand diameter	0.8 mm
Number of strands	35
Cu/NCu	0.87
Filament twist pitch length	13 mm
Bare cable width	15.15 mm
Bare cable average thickness	1.437 mm
Insulation thickness	0.1 mm

Table 2.1: Main parameters of HQ

net stored energy, and dissipated within the coils. Adding it to the power equation as an external source is a mistake.

2.4 Experimental validation with HQ data

The model described in section 2.3 and implemented in QLASA has been validated with various experimental data from different magnets. In this section, the experimental comparison with HQ data [7] is reported.
The main parameters of HQ [5] are listed in Table 2.1. Considering the twist pitch reported in Table 2.1, a resulting average decay time τ of 15 ms has been used for IFCC (see equation 2.19). Here we report the comparison with the HQ test already shown in fig. 2.1 and in fig. 2.7, which is a discharge on a 60 mΩ dump resistor from a starting current of 13 kA, without an initial natural quench. The comparison is reported in Fig. 2.9. As it can be seen in fig. 2.7, the model simulating IFCC can describe the current decay only at the beginning. In fig. 2.9, a simulated decay which includes IFCC effect on the inductance and quench back is compared to the experimental data, and it is easy to see that it can describe very well the measured discharge. The main assumption on the quench back is that half of the magnet quenches 15 ms after the beginning of the discharge, then the quench propagates in

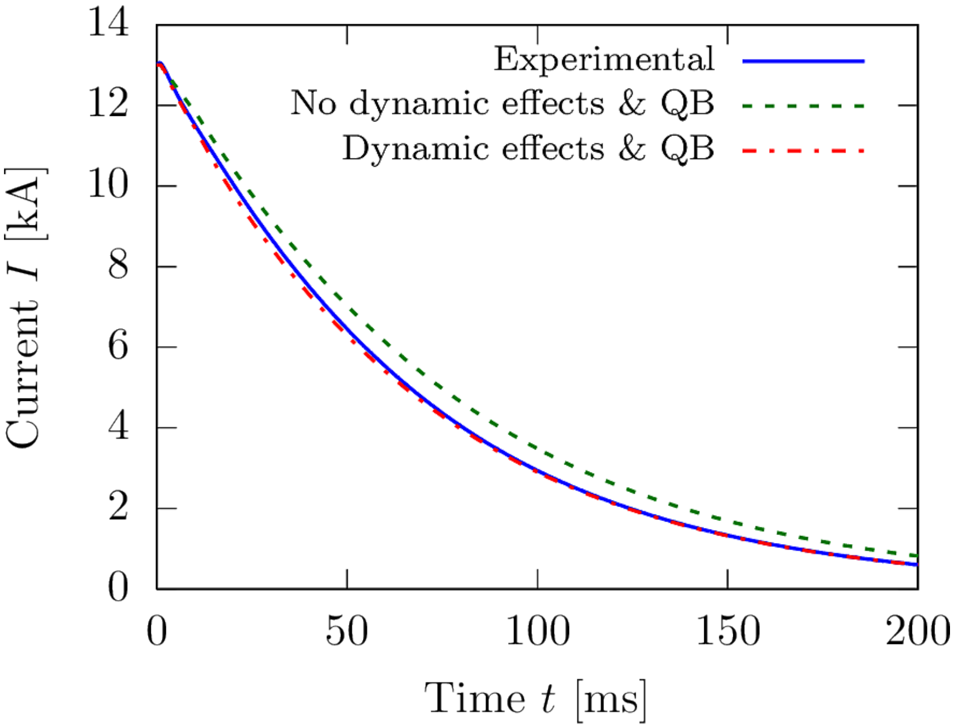

Figure 2.9: Comparison of experimental data (solid blue) from a HQ test with a simulation of QLASA considering IFCC effect on the magnet inductance and quench back (dashed red), and a simulation of QLASA without IFCC effect on the magnet inductance, but with quench back (dashed green)

the three directions; this number comes from experimental measurements and simulation from the CLIQ experience [15]. At now, QLASA cannot estimate the size and the time needed for the quench back to occur, but this values can only be added as external parameters.

It is very interesting to point out that adding quench back to the simulation is necessary to describe the experimental decay until the end, but, using a reasonable numbers, it is impossible to fit the decay considering only quench back and no dynamic effects on the inductance. In fact, in fig. 2.9 it is also reported a simulation with a quench back of the *whole* magnet which occurs 10 ms after the beginning of the decay, neglecting the dynamic effects on the inductance. Despite the strong assumption on the quench back time and size, it is easy to see that the current decay is yet too slow. The conclusion is that, considering fast quenches, the combination of dynamic inductance and quench back is needed in order to perform reliable simulations, and both quench back and IFCC effect on the inductance are important actors which cannot be neglected. This model can be considered useful for the design of high performance, high field superconducting magnets with a challenging quench protection.

Similar analyses, not reported here for the sake of simplicity, have been performed on different experimental data and magnets, with very similar results. An important comment is that the only sensitive parameter used during the experimental comparison is the IFCC decay time constant: this number has been set in order to fit the experimental current decays as much as possible, verifying that the used value is reasonable. It has been seen that the resulting decay time is basically the one obtained considering the copper resistivity at the average magnetic field, such as in the case reported here.

However, the comparison is not very sensitive to the decay time constant. For example, in Fig. 2.10 two simulations of a HQ discharge on a 60 mΩ dump resistor are reported, using two different values for the IFCC τ: 15 ms and 30 ms, therefore a factor 2 difference. It can be seen that the resulting decays are qualitatively very similar. This is an indication that it is important to consider the inductance reduction, but the model is not so sensitive to the used parameters, at this level of complexity. A more complex, numerical study could give more information on other quantities involved in the process.

An analysis of a current decay with quench heaters and no dump resistor is reported in the next section, together with other important considerations.

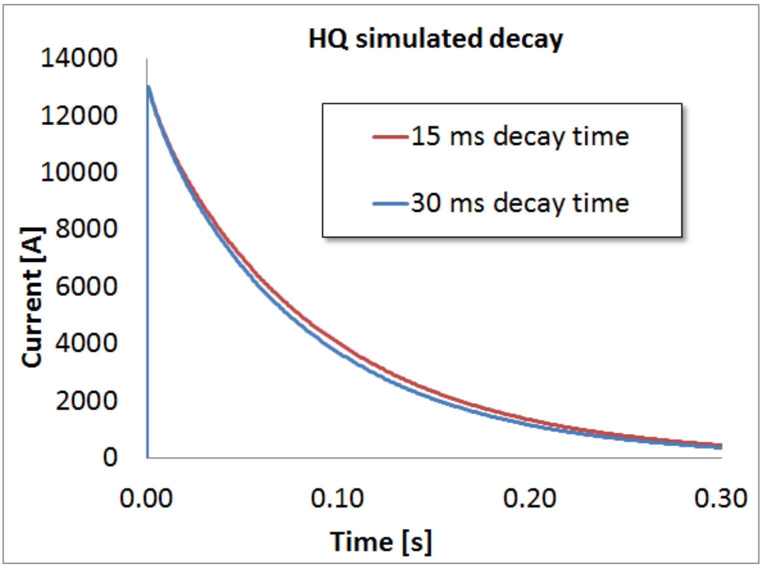

Figure 2.10: Comparison of two simulations of a HQ decay on a 60 mΩ dump resistor, obtained using two different values for the IFCC decay time

2.5 Inductance measurement during a quench

In section 2.4 we have seen that the model describing IFCC effect on the magnet differential inductance can be used in order to fit the current decay of a magnet during a quench, and therefore that it can be used in order to predict with a better reliability the hot spot temperature. But, can this be considered a *proof*, or a validation, of the model?
The actors of the current decay during a quench are the resistance, and the inductance; the resistance is basically the sum of the dump resistor resistance and the quench resistance (see figure 2.4). The dump resistor is obviously known, therefore the main unknowns during a quench are the magnet inductance and the quench resistance. How can we know them? Typically, this issue is solved measuring the current and the voltage between magnet ends: first, at low ramp rate, the voltage across the ends is purely

inductive (no quench is expected), therefore the inductance can be easily computed as $L = \frac{V}{\dot{I}}$; then, during a quench, known the inductance as previously specified, the magnet resistance can be computed as:

$$R_q = \frac{V - L\frac{dI}{dt}}{I} \tag{2.49}$$

But, we have learned in this section that the inductance of a superconducting magnet during a quench is substantially different from the one that can be measured at low ramp-rate! This means that this method leads to make mistakes in the evaluation of the quench resistance. The only way to measure the resistance is knowing the inductance, but this quantity is an unknown. The inductance depends on the current decay, and has to be evaluated case by case if one wants to include the dynamic effects due to coupling currents

This argument leads to another conclusion: during a quench, we cannot measure the inductance, therefore we cannot measure the resistance; the only thing we can measure is the current, which is a combination of inductance and resistance. In section 2.4, we have shown that the IFCC model can fit a current decay, but we do not know anything about modeled quench resistance and inductance compared to the experimental ones; to our present knowledge, this method could carry to an underestimation of the inductance, and to a contemporary overestimation of the resistance due to quench software, leading to an apparently well working simulation tool. But we do not want (only) a well working quench software, we want a good model describing IFCC. In order to validate the model developed in this chapter, we need an inductance measurement during a quench.

2.5.1 How to measure the inductance

If the inductance measured at low ramp-rate is useless at our scope, what shall we do? We need to measure the inductance during the quench discharge, and compare it to the simulated one, but how can we do it?

The easiest way to answer these questions is planning a special quench test aiming to the inductance measurement. Here we present an example of how measure the inductance of a superconducting quadrupole during a quench. We need:

- Current measurement
- Voltage measurement across the whole magnet and across everyone of the four coils
- Quench induced artificially by quench heaters or spot heaters in **maximum** two coils
- **At least two** purely superconducting coils
- No spontaneous quench
- Obviously, a quench protection system which avoids damaging the magnet

With these tools, the inductance can be measured from one of the superconducting coils: in fact, it can be proved that the magnet inductance, in a quadrupole, is the inductance of one coil times four:

$$L_{quadrupole} = 4L_{coil} \tag{2.50}$$

This is true and generalizable for any periodic magnet. The inductance of a coil can be computed using the current measurement and the voltage measurement across that coil:

$$L_{coil} = \frac{V_{coil}}{\frac{dI}{dt}} \tag{2.51}$$

But then, why do we need **two** superconducting coils? In a test like this, it is very probable that a quench occurs in one of the coils, due to quench back or to quench propagation from other coils, but we could not able to notice it with a single measurement. If a quench happens and we do not notice it, our measurement can become unreliable. A simple way to avoid this is to measure the inductive voltage in two identical coils: if no quench occurs, the two voltages will appear exactly identical, in the limit of the measurement noise, which is usual very low; in case of a quench of one coil, the two signals will become noticeably different, and the measurement can be considered reliable until that moment, while after that we do not know anything about the resistance of the coils. In principle ,it could also happen that exactly the same quench occurs in the two coils, and that exactly the same resistive voltage appears in both of them, creating a confused situation; by the way, this is a largely unlikely and unrealistic case. However, in principle one could do the measurement with just one superconducting coil, but the results should be checked with care in some way.

With this special test, it is possible to measure the inductance during a quench, and to compare it to the model developed in order to simulate the IFCC effect on the inductance, and to validate this model. A test like this has been planned and performed for HQ [16]; in the following, we are going to see the data analysis and comparison of experimental results with simulations [17].

2.5.2 Analysis of HQ data

In this section we report the analysis of the experimental data from a test from HQ experimental data in order to obtain a direct measurement of the inductance during a quench. The experimental data from the acquisition system are the current and the voltages of each of the 4 coils (named coil number 15, 16, 17 and 20), which have been acquired with a sampling rate of 100 kHz per channel. Figure 2.11 shows the current decay of the considered test. In this test, a quench has been artificially induced in coil 16 by one strip of the quench heaters, then the protection system, constituted by a 60 mΩ dump resistor, had a delay time of 300 ms before the activation. This test is ideal in order to perform the inductance measurement like the one described in section 2.5.

In fig. 2.11, the experimental decay is compared to two QLASA simulations: one considers the IFCC dynamic effects on the magnet inductance with a decay time for the coupling currents $\tau = 30$ ms, the other one neglects

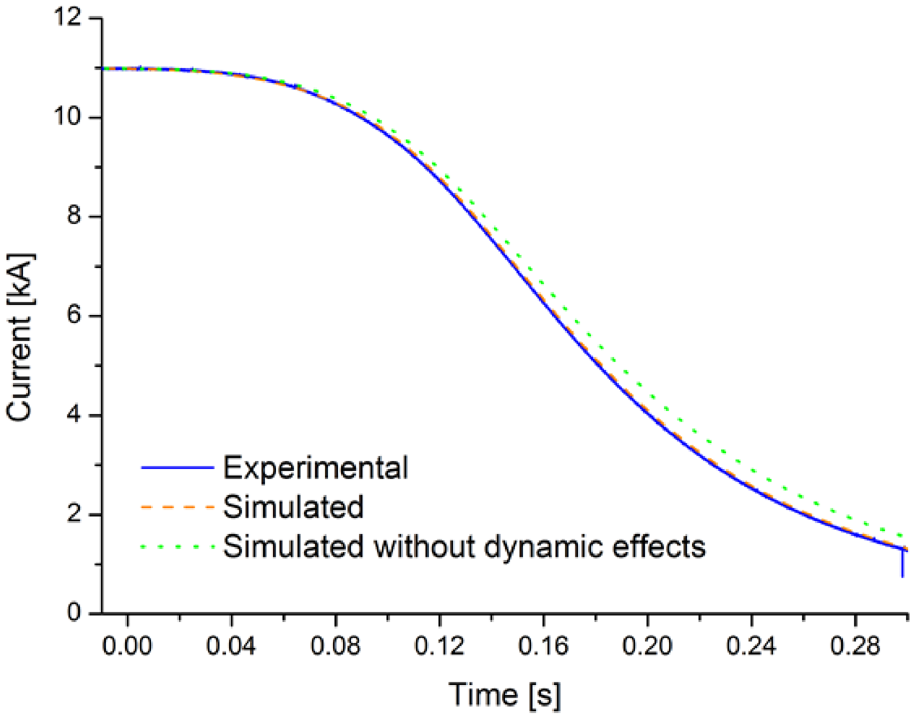

Figure 2.11: Experimental HQ current decay with quench induced in coil n. 16 and delay time of the quench protection system equal to 300 ms. The picture reports also the current decay QLASA simulations including and not including the dynamic effects due to IFCC for the inductance calculation.

them. It can be noticed that the model is needed in order to describe well the experimental discharge; however, the effect is less evident than in tests with dump resistor, such as the one shown in figure 2.7, because, in this case, when the inductance reduction is large, the quench resistance is small, then the decay is not so fast. By the way, our target now is to measure the inductance and validate the model.

In order to measure the inductance, we need the current derivative (see equation 2.51). The current derivative can be calculated numerically from the experimental data, but it requires a smoothing process, because the noise due to the large sampling frequency completely covers the calculated signal. Fig. 2.12 reports the graph of the current derivative, numerically calculated and smoothed applying twice a moving average 3.5 ms wide, which resulted the best compromise to obtain clean signal keeping a temporal resolution of the order of 10 ms [18]. From equation 2.51, it is evident that we need the voltage across the coils. In particular, we need the voltage across a superconducting coil. Fig. 2.13 reports the experimental voltages across the four coils, after noise suppression. It is easy to note that the coil

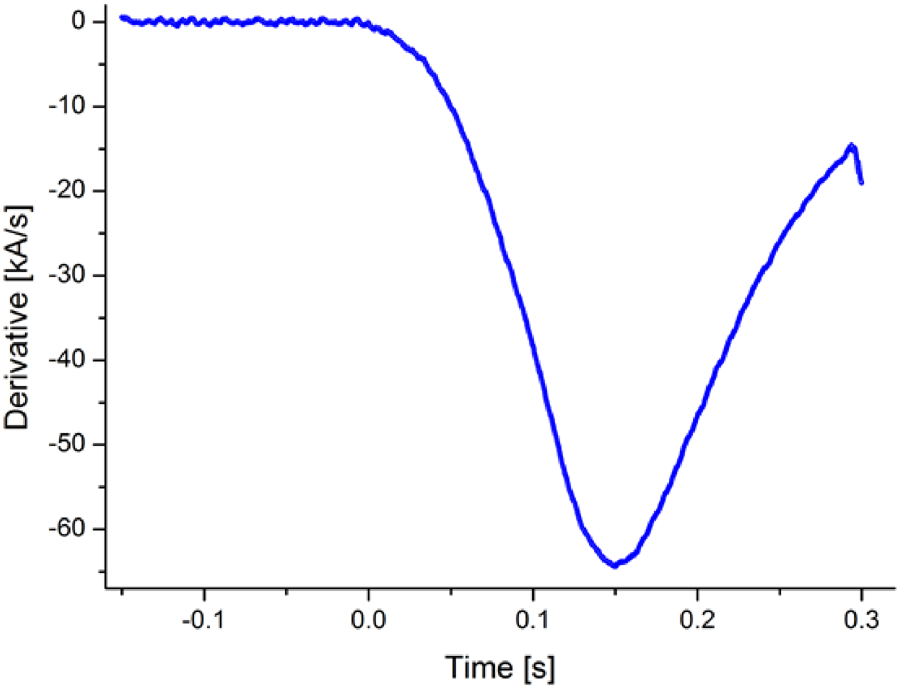

Figure 2.12: Current derivative vs. time with quench provoked in coil n. 16 and delay time 300 ms, calculated numerically and noise-suppressed

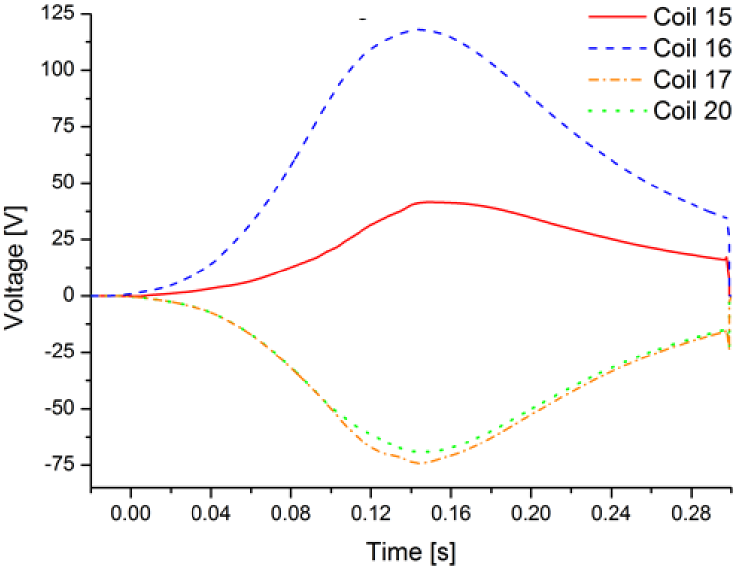

Figure 2.13: Voltages vs. time on each coil after smoothing and 50 Hz noise suppression with quench provoked in coil n. 16 and delay time 300 ms

16 has the first quench, because it reaches the highest resistive (positive) signal. Coil 15 too is resistive, probably because of quench propagation from coil 16. Then, coils 17 and 20 are surely in the superconducting state until ∼100 ms, because their signals are identical; after that, in coil 20 a resistive voltage appears (quench back probably), and we do not know until when the coil 17 maintains its superconducting state. This shows the importance of having two superconducting coils instead than just one. The coil chosen for the voltage analysis is coil 17.
As just said, it was necessary to apply a smoothing process to the voltages signal too, in order to suppress the noise. Fig. 2.14 reports the graph of the coil 17 voltage vs. time just before and at the beginning of the quench induced in coil 16.
After a first smoothing with a moving average of 3.5 ms (the same as the

current derivative), the signal can be considered almost clean; however a typical 50 Hz noise from the grid power is still present, such as can be seen in figure 2.14. We proceeded to suppress it by subtracting an equivalent 50 Hz sinusoidal signal with the same phase which was fitted from the voltage curve (red curve in Fig. 2.14). After data analysis and noise

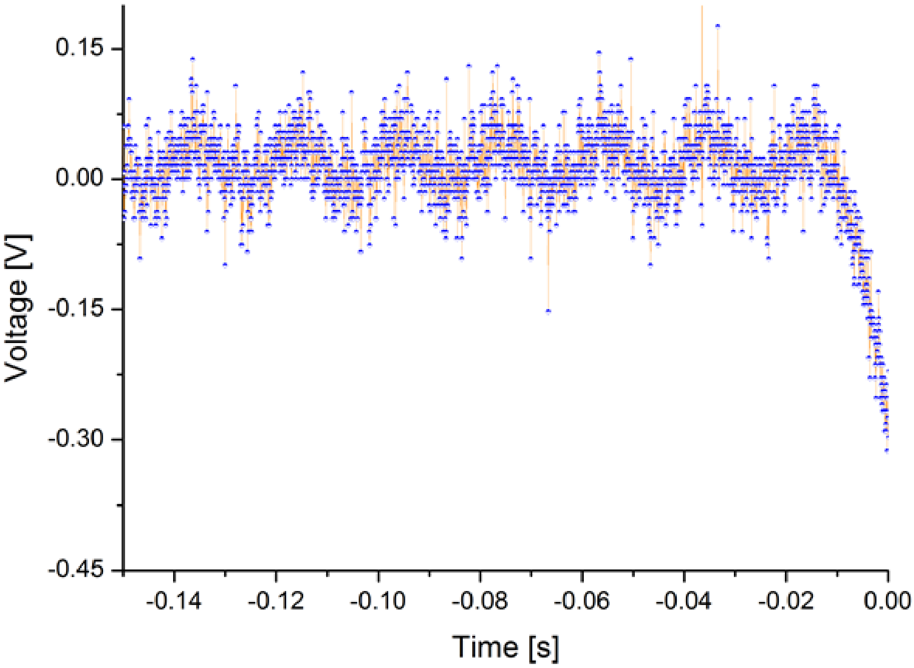

Figure 2.14: Voltage vs. time of coil 17 after a first smoothing with average moving. It is evident the 50 Hz noise superimposed to the signal, which can be fitted (red curve) and then subtracted.

suppression, using the experimental voltage of coil 17 shown in fig. 2.13, the current derivative signal shown in fig. 2.11, and equation 2.50 and 2.51, the experimental inductance of HQ during this quench test can be computed. Fig. 2.15 reports the HQ experimental differential inductance computed in this way, comparing it to the measure one at steady state, and to the simulated one using QLASA.

Despite the careful smoothing process of the signals of voltage and of current derivative, the experimental inductance curve still presents some anomalous oscillations, which can give an indication of the amplitude of the error committed in its evaluation.

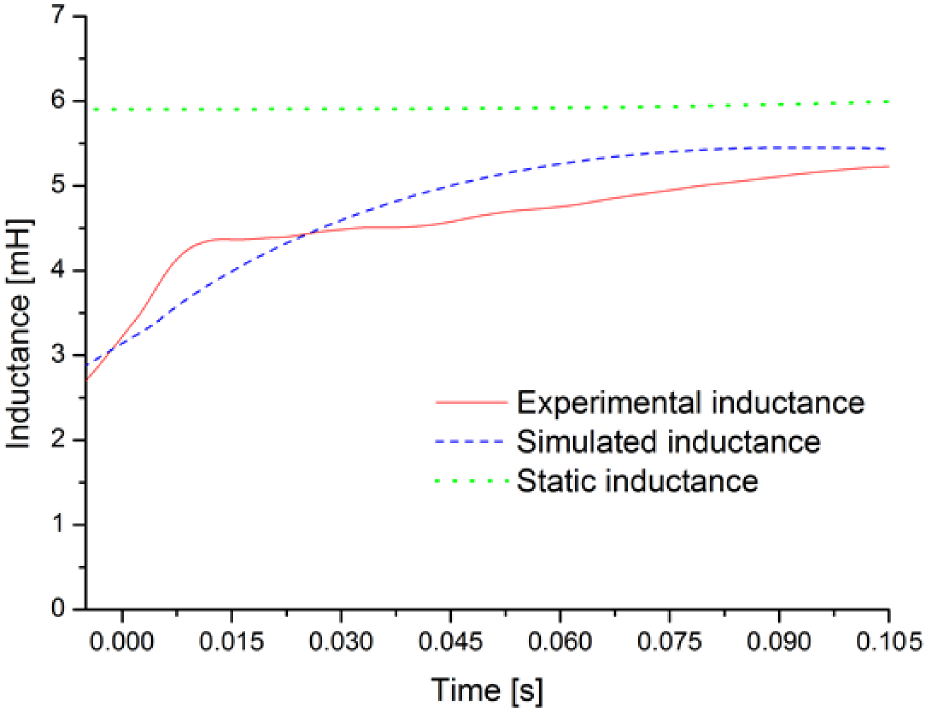

Figure 2.15: Experimental inductance vs. time for quench test provoked in coil n. 16 and delay time 300 ms. The picture reports also the simulated dynamic/static inductances. The graph is intentionally interrupted at 100 ms because the experimental inductance is meaningless when back-quenches start in coil 17 and 20 at about 100 ms.

It is easy to notice that the experimental value of the differential inductance is well below its nominal value in static condition; at the beginning of the quench the differential inductance assumes a value $\sim 50\%$ lower, and then it increases in about 10 ms. This difference can be interpreted as dynamic effects for the large and rapid variation of the magnetic field during the quench. In fact, the very simple model which computes the effect of inter-filament-coupling-currents on the differential inductance, described in section 2.3 and implemented in QLASA, can qualitatively describe with a good reliability the experimental inductance behavior, considering a reasonable value for the coupling currents decay time of $\tau = 30$ ms, as it can be seen in figure 2.15. This is a good confirmation of the model developed and implemented. As just mentioned previously in section 2.4, changing the value of τ does not significantly impact the analysis (unless using unreasonable values), however 30 ms is the best fit.

2.5.3 Simulation of quench with dynamic effects

In this section, we analyze in deep the quench simulation performed using QLASA in order to obtain the simulation curves shown in fig. 2.11 and 2.15. Such as already mentioned several time, in QLASA the model which takes in consideration the inter-filament-coupling-currents effect on the differential inductance described in section 2.3 has been implemented. The coupling current time constant τ which best reproduces the experimental data is 30 ms, to be compared with a theoretical value of about 15 ms based on the nominal twist pitch l and effective transverse resistivity ρ_e. In Fig. 2.16 and 2.17 the experimental and simulated value of the voltages in the inner and outer layers of each coil are reported; the agreement is overall quite good. To fit the curves, a quench back in coil 17 and coil 20 has been induced in the simulation with a delay of about 100 ms. As just mentioned, the quench back time cannot be computed by QLASA, and it has to be added as input parameters.

The acquisition of purely inductive voltage signal for coil 17 and 20 allowed to obtain the experimental resistive voltage of the coil 15 and 16 (difference between total voltage in coil 15 and 16 and inductive voltages, see equation 2.49). Fig. 2.18 reports the comparison of the so obtained

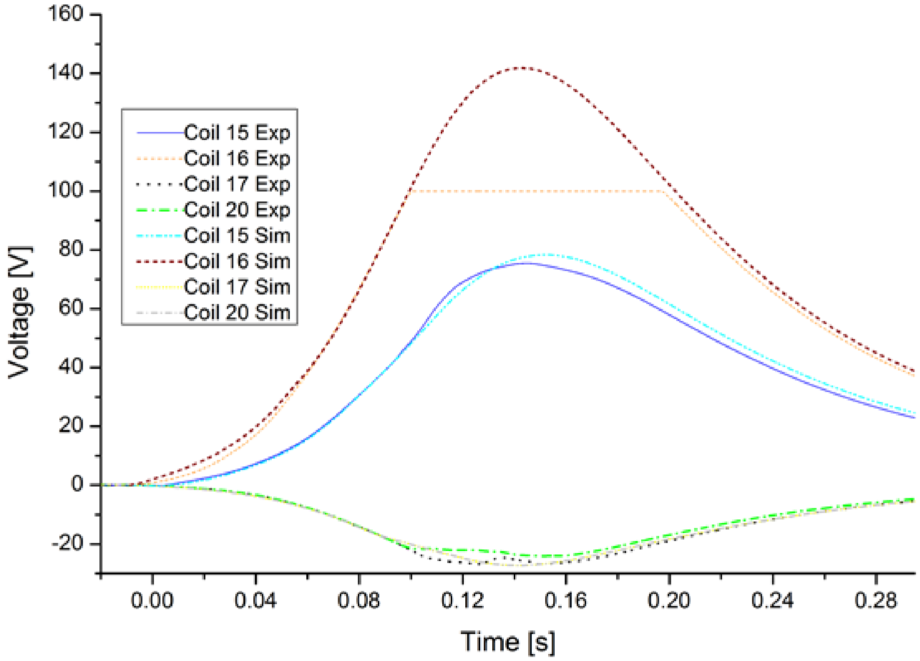

Figure 2.16: HQ experimental and simulated voltages on inner layers of each coil (quench provoked in coil n. 16 and protection system delay time 300 ms)

experimental resistances in coil 15 and 16 with respect to the simulated. one by QLASA, considering IFCC model and 100 ms quench-back. More details on the analysis and comparison can be found in [18]. It can be seen that the resistance agreement is very good up to about 100 ms; later the difference increases. However, this can be explained considering that the experimental resistance is under-estimated: in fact, in the subtraction shown in equation 2.49 to obtain the resistive voltage, the growing resistive voltage of coil 17 (which has a quench back at about 90 ms) is not properly accounted for. Basically, the measurement has to be taken with care after 100 ms, as after this time none of the coils can be used reliably to obtain the inductive voltage as none of them is superconducting (purely inductive).

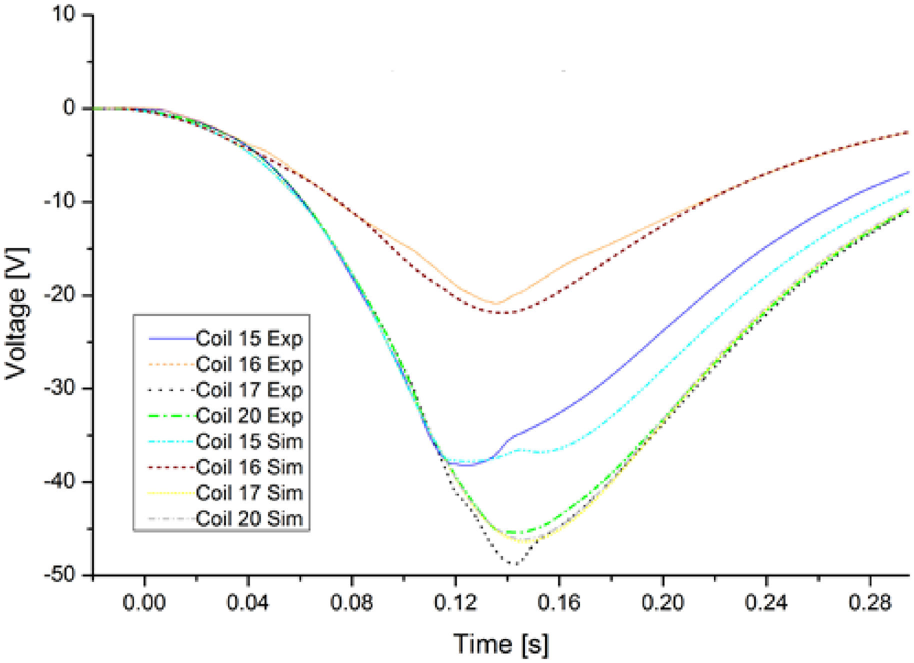

Figure 2.17: HQ experimental and simulated voltages on outer layers of each coil (quench provoked in coil n. 16 and protection system delay time 300 ms)

2.6 Conclusions and perspectives

In this chapter we have developed a model aiming to calculate the inductance reduction due to the inter-filament-coupling-currents in superconducting magnets; by the way, this model can be generalized to any magnetization phenomenon. The model developed is basically analytic, and it aims to describe in a simple way the physics beyond this phenomenon. Only after that it can be implemented in quench softwares to perform simulations. In fact, this model is very easy to implement in any quench simulation program, but it makes some strong assumptions which would be better to improve, such as the magnetic field which does not change with

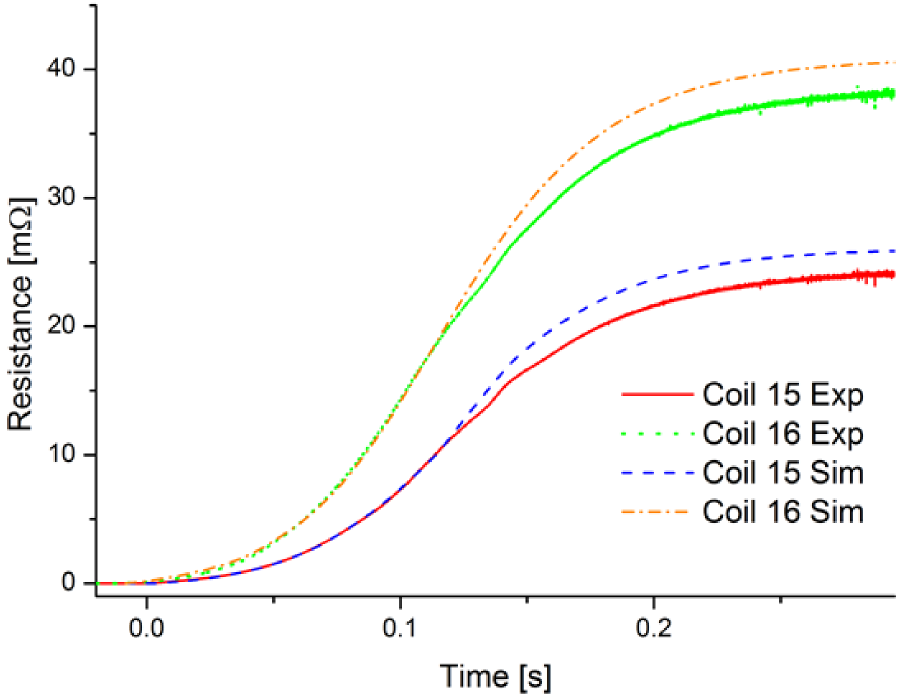

Figure 2.18: Experimental and simulated resistance of coil 15 and 16.

the coupling currents, the IFCC decay time which is an average value, etc... However, the model has been implemented in the QLASA quench software, and some simulations have been compared with experimental current decays from HQ data; the results can be considered encouraging, in fact with reasonable values of coupling currents decay time and quench back it is possible to fit the experimental current decay.
Moreover, we have shown how to perform an inductance measurement during a quench. An experimental inductance measurement has been made on HQ, and the experimental results have been compared to QLASA simulations. The results are pretty good: the inductance reduction is experimen-

tally visible, and the model implemented in QLASA can describe it well. This work leads to this important conclusion for the magnet community: using the inductance measured at steady-state in order to obtain the quench resistance, during fast quenches, can induces to some errors. The inductance can be largely different, and the effect of coupling currents should be taken into account. Moreover, the inductance reduction depends on a transient effect, which is the coupling currents; therefore, it is very important to understand that the inductance of a magnet cannot be known a priori, such as one can imagine; the idea of a plot of inductance vs current, or inductance vs current derivative, is meaningless when considering a transient effect such as eddy currents. In fact, the inductance depends on the state of the coupling currents, which rise during a quench, reach their maximum, and the decrease, with an unknown function. The main point is that the current decay depends on the inductance, but also the inductance depends on the current decay! They are linked together, and it is impossible to analyze them separately. Obviously, in some cases (such as low ramp rate measurements), these effects can be considered negligible, and classical measurements can be considered valid.

The model implemented in this chapter is a very important improvement for the quench protection study of superconducting accelerator magnets, providing more realistic values of the inductance of the magnets during fast discharges (respect to the too much large values of static inductances) and better estimations of the maximum temperature during a quench. Moreover, it allows the development of more performing magnets. In the next chapters, we will see the use of this model for the quench protection study of some accelerator magnets.

In the future, the implementation of this model in more performing softwares could lead to more reliable and detailed results.

Chapter 3

Quench protection of MQXF, the low-β quadrupole of HiLumi LHC

3.1 High Luminosity LHC (HiLumi)

The Large Hadron Collider (LHC) in 2010-2013 has produced collisions between proton beams with up to 4 TeV energy per beam. Now, LHC is producing collisions at 6.5 TeV per beam, and it will run until 2023. It is expected that in 2023 the integrated luminosity of 300 fb^{-1} will be reached; beyond this value, running the machine will not lead to significant statistical advantage, if the present peak luminosity of 1.5 - 2 x 10^{34} cm^{-2}s^{-1} will be maintained.

Then, a luminosity upgrade program, named High Luminosity LHC (HiLumi-LHC), has been planned, aiming at reaching an integrated luminosity of 3000 fb^{-1} in 10 years after 2025. The purpose of this upgrade is to produce more collisions per unit time, in order to increase the statistic number of particles that have to be investigated, and to study them with better precision and less errors. Without this program, LHC will be almost useless after 2023; for this reason, this will be the most important project at CERN

in the next 5-10 years.
The main intervention of HiLumi will be reducing the beam size. This can be achieved, among other interventions, replacing magnets in the interaction regions with more performing ones. To explain this, in section 3.2 we will discuss how the beam focusing works in an accelerator magnet, and what is an insertion.

3.2 Beam focusing and insertions

3.2.1 Motion of a particle

Consider the propagation on a path of lenght L in the free space of a particle with initial position x_0 and with divergence $\dot{x}$ (see the fig. 3.1), where $\dot{x}$ indicates the derivative respect to the propagation direction, named s. The final particle position is

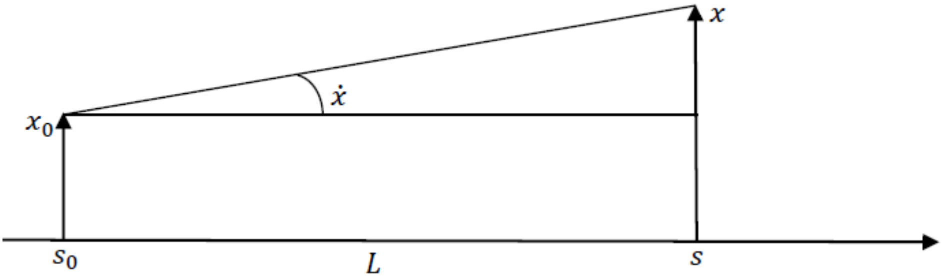

Figure 3.1: Particle propagation on free space

$$x = x_0 + L \tan \dot{x} \simeq x_0 + L\dot{x} \tag{3.1}$$

while the divergence is assumed to be small and constant. It is therefore possible to write equation 3.1 in matrix form, together with the information that the divergence is constant during the path.

$$\begin{pmatrix} x \\ \dot{x} \end{pmatrix} = \begin{pmatrix} 1 & L \\ 0 & 1 \end{pmatrix} \begin{pmatrix} x_0 \\ \dot{x}_0 \end{pmatrix} \tag{3.2}$$

In general, it is always possible to describe the motion of a particle in a linear system (and an accelerator is a linear system at the first order) by means of the equation

$$\vec{x} = M\vec{x}_0 \tag{3.3}$$

where x and x_0 are respectively the particle coordinates at the start and at the end of the system, and M is called *transport matrix* of the system. Therefore, it is possible to describe the motion of a particle using and combining the transport matrix of every component of an accelerator.

3.2.2 Transport matrix of a magnetic quadrupole

In this section, we aim to compute the transport matrix of a perfect magnetic quadrupole. The reference system moves together with the reference particle (the ideal particle that is on a perfect circular orbit on the bending sections, in a perfect straight trajectory on the focusing sections), as you can see in fig. 3.2. A perfect quadrupolar field can be written as

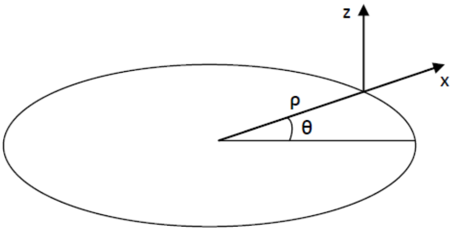

Figure 3.2: Reference system for beam particles. The reference particle is in the origin of the system

$$\begin{cases} B_x = Gz \\ B_z = Gx \\ B_s = 0 \end{cases} \tag{3.4}$$

where the longitudinal coordinate is $s = \rho\theta$.
The three components of the motion equation for a particle with charge q

in such a field, and in absence of acceleration, are:

$$\begin{cases} m\frac{d^2x}{dt^2} = q(v_s B_z - v_z B_s) \\ \\ m\frac{d^2z}{dt^2} = q(v_x B_s - v_s B_x) \\ \\ m\frac{d^2s}{dt^2} = q(v_z B_x - v_x B_z) \end{cases} \tag{3.5}$$

With the assumption that the particle velocity has only longitudinal component, i.e. $v \simeq v_s$, and replacing equation 3.4 in equation 3.5, the following equations can be obtained:

$$\begin{cases} m\frac{d^2x}{dt^2} = qvGx \\ \\ m\frac{d^2z}{dt^2} = -qvGz \\ \\ m\frac{d^2s}{dt^2} = 0 \end{cases} \tag{3.6}$$

It is easy to understand from equation 3.6 that the longitudinal motion is simply uniform rectilinear; therefore we pay attention only on the transversal motion. By means of the variable change $s = vt$, equation 3.6 becomes

$$\begin{cases} \ddot{x} = \frac{qG}{mv}x \\ \\ \ddot{z} = -\frac{qG}{mv}z \end{cases} \tag{3.7}$$

The product $mv = p$ ís the particle momentum; it is easy to prove that, for a particle in circular motion, the equation 3.8 is valid.

$$\frac{p}{q} = B\rho \tag{3.8}$$

The product $B\rho$ is called *rigidity* of the beam. Thus, replacing equation 3.8 in equation 3.7 we obtain

$$\begin{cases} \ddot{x} = \frac{G}{B\rho}x \\ \\ \ddot{z} = -\frac{G}{B\rho}z \end{cases} \tag{3.9}$$

Assuming $G > 0$, it is easy to understand that the quadrupolar field has a focusing effect on the axial plane (it is the harmonic motion equation!), while it has a defocusing effect on the radial plane. It is therefore possible to describe the motion of a particle that goes through a quadrupole with length L, with initial coordinates x_0 and $\dot{x}_0$, by solving the differential equation 3.9. The solutions are well known, and in matrix form they are:

$$\begin{pmatrix} x \\ \dot{x} \end{pmatrix} = \begin{pmatrix} \cosh kL & \frac{1}{k}\sinh kL \\ k\sinh kL & \cosh kL \end{pmatrix} \begin{pmatrix} x_0 \\ \dot{x}_0 \end{pmatrix} \tag{3.10}$$

$$\begin{pmatrix} z \\ \dot{z} \end{pmatrix} = \begin{pmatrix} \cos kL & \frac{1}{k}\sin kL \\ -k\sin kL & \cos kL \end{pmatrix} \begin{pmatrix} z_0 \\ \dot{z}_0 \end{pmatrix} \tag{3.11}$$

where

$$k^2 = \frac{G}{B\rho} \tag{3.12}$$

The matrices structure is similar, but in the focusing case trigonometric functions appear, in the defocusing case hyperbolic functions appear. The matrices are the transport matrices of a magnetic quadrupole.

In this section, we have understood that a magnetic quadrupole focuses a particle in a direction, and defocuses the same particle in the perpendicular direction

3.2.3 Beam motion

The motion of a beam is more complicated than that of a single particle; for a detailed explanation you can refer to [19] . Here, we present just a brief introduction.

Briefly, a beam can be described by an ellipse in the phase space ($\vec{x}$,$\vec{\dot{x}}$). The ellipse is made by all the particles within the beam, which have a certain position and a certain divergence. The ellipse evolution represents the beam behavior under the effect of the machine components, and it can be described using the transport matrices, such as for the single particle.

A synchrotron is a periodic machine (at least, the period is the whole circumference). You can prove that the beam motion has the same periodicity

of the machine. So, you can reach beam focusing by repeating several times a small system with a focusing effect on the beam. The simplest system of this kind is the *FODO cell*: it is composed by a focusing quadrupole (F), a free space (O), a defocusing quadrupole (D) and another free space. Under certain conditions, such a system can have a resulting focusing effect on both radial and axial direction. In the free spaces magnetic dipoles can be inserted, in order to bend the beam; focusing effect from dipoles is negligible, so the periodicity is preserved.
FODO is only one of the focusing system that has been studied: different configurations of focusing and defocusing quadrupoles are used in order to focus the beam. We are particularly interested in the focusing system which is usually posed close to the colliders intersection regions, called *insertion.*

3.2.4 Insertions and inner triplet

The purpose of the insertions is to reduce as much as possible the beam size in the collision point. They are therefore one of the main components which can act on the luminosity.
The luminosity of an accelerator is proportional to the rate of events when a collision occurs in the interaction point. Clearly, the smaller the beam cross section is, the bigger the luminosity. Insertions are a sequence of focusing and defocusing quadrupoles, plus other magnets. This sequence aims at reducing the more as possible the beam size in the collision point. The size of a beam is directly proportional to a quantity called β function.

3.2.5 The inner triplet

The inner triplet is the main actor of an insertion. It is a sequence of three quadrupoles (a triplet), set in order to reduce as much as possible the β function, and therefor the beam size, in the interaction point. For this reason, they are also called *low-β quadrupoles.*
An important feature of low-β quadrupoles is that their focusing power is proportional to their bore diameter: the larger is the quadrupole, the lower

will be the beam in the interaction point. Without going into details, which can be found in [19], this is due to the fact that the area of the ellipse in the phase space which describes the beam is constant in absence of acceleration, such as during particle collisions; for this reason, in order to obtain a small beam, one has to create a large beam, and this is exactly what the insertion has to do. A simple explanation is shown in figure 3.3.

In order to have a small beam in the collision point, it is therefore important to design large inner-triplet quadrupoles.

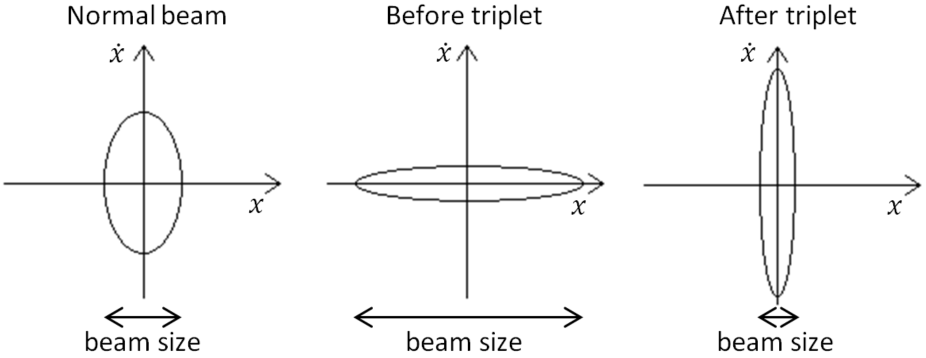

Figure 3.3: Example of a beam ellipse in the phase space before entering in the insertion (left), in the insertion before the triplet (center), and in the interaction point after the triplet (right)

3.3 MQXF quench protection

MQXF is the low-β quadrupole designed by the HiLumi-LHC program. As just said in section 3.1, the target of HiLumi is to increase the machine luminosity. In order to do so, one of the interventions will be replacing the present low-β quadrupoles, with new, more performing ones. In particular, the present lowβ triplet NbTi superconducting quadrupoles are planned to be substituted with new Nb_3Sn magnets, called MQXF.

MQXF is one of the first Nb_3Sn superconducting magnets designed in order to be inserted in a particle accelerator, and many challenges have been faced. The main features of this magnet are the high field reached, which is 11.5 T, and the large aperture, which is 150 mm, versus 70 mm of the present triplet magnets. In table 3.1 the main MQXF parameters are reported. Fig. 3.4 reports the MQXF magnetic field, Fig. 3.5 reports the whole MQXF cross section. More details on the MQXF magnetic and mechanical design can be found in [20].

One of the most challenging aspects of the MQXF design has been the quench protection. This is because of the large magnetic energy stored into the coils (0.12 J/mm3, a factor 2 larger than in the present NbTi LHC lowβ quadrupoles), and of the high magnetic field (12 T) needed for the

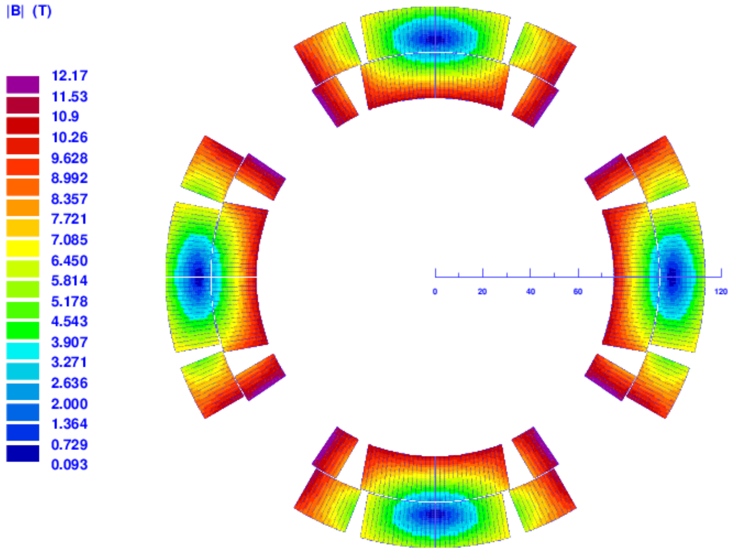

Figure 3.4: Magnetic field of MQXF

MQXF parameters	
Material	Nb_3Sn
Aperture diameter	150 mm
Gradient	132.6 T/m
Nominal current	16470 A
Magnetic stored energy	1.17 MJ/m
Inductance @ $I = 0$	8.3 mH/m
Magnetic length (Q1/Q3)	2 x 4.2 m
Magnetic length (Q2a/Q2b)	7.15 m
Conductor peak field	11.5 T
Operating temperature	1.9 K
Operating point on the load line	76%
Strand diameter	0.85 mm
Number of strands	40
Bare cable width	17.86 mm
Bare cable inner thickness	1.462 mm
Bare cable outer thickness	1.588 mm
Cable insulation thickness	0.145 mm
Cu/NCu	1.2
Copper RRR	100
Filament twist pitch length	19 mm

Table 3.1: MQXF main parameters

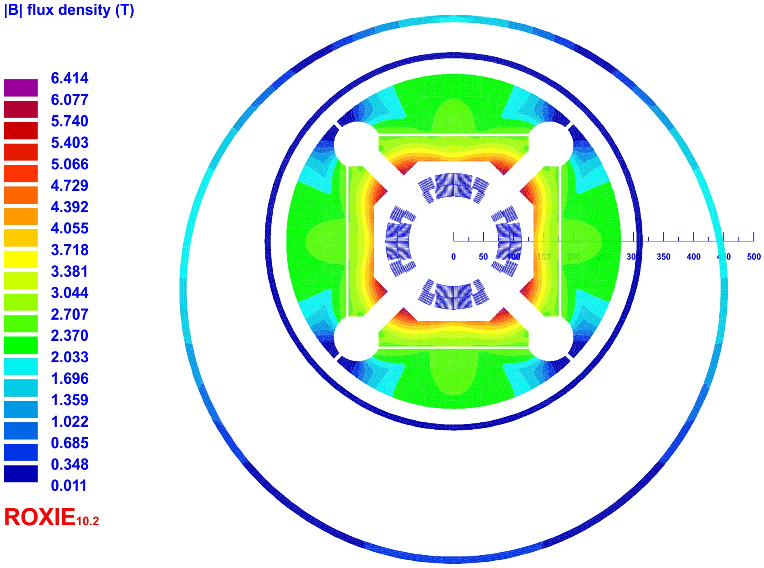

Figure 3.5: MQXF cross section

focusing of the beams. In the next section, we are going to analyze in deep the quench protection study of MQXF.

3.3.1 MQXF MIITs

First of all, it is important to compute the MIITs for the MQXF cable. As explained in section 1.4.1, MIITs are an usefool tool to compute the magnet hot spot temperature. In fig. 3.6, the plot of the MQXF cable MIITs versus the temperature is reported. In the figure, two curves appear: one considers that part of the cable contains bronze, one neglects it. The reason of adding bronze to the cable materials is due to the manufacture of Nb_3Sn cables: very briefly, niobium is made to combine with tin during a thermal process; however, part of the tin bounds with the copper matrix, therefore a part of the cable becomes bronze. Some experimental measurements showed that $\sim 30\%$ of the not copper fraction of the cable can be bronze [21],

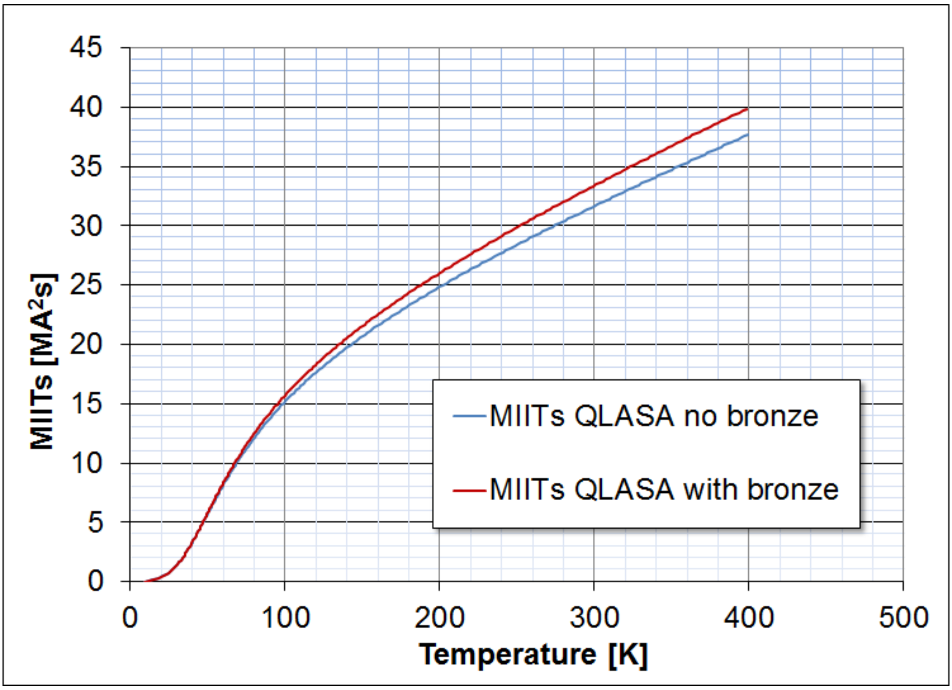

Figure 3.6: MIITs of the MQXF cable, considering bronze inside the cable, or not considering it.

therefore this quantity has been used to create the plot shown in figure 3.6. It can be seen that the effect is not negligible, and, in particular, it helps the protection. Considering that this quantity has been experimentally evaluated, the protection study reported here consider 30% of the cable not copper fraction to be bronze.

3.3.2 Temperature limit

The temperature limit chose for the quench protection of MQXF is 350 K [21]. Usually, in the magnet community the chosen value is 300 K. However, due to the very challenging nature of the MQXF protection, it has been chosen to increase this value. This is due to the fact that, actually, the ideal limit is 390 K: the Nb_3Sn coils are impregnated in an epoxy resin, which gives mechanical stability to this brittle material. However, it melts at 390 K, therefore after that temperature the coil risks to be damaged. In order to have some margin for uncertainties such as material properties, usually the quench protection limit is chosen to be 300 K, performing conservative studies. For MQXF, it has been chosen to perform a more detailed and realistic protection study, but with the higher limit of 350 K.

3.3.3 Material properties

In order to compute the hot spot temperature of the magnet, it is very important to choose the right material properties. In fact, as it can be seen in equation 1.9, the MIITs developed within the cable depends on the material properties.
In literature, there are various libraries which provide material properties of all the materials involved in superconducting magnets, such as copper, superconductors, epoxy, metals, and whatever else. The choice of a library can significantly affect the resulting hot spot temperature, such as showed in details in [22]. In this section, the library used for material properties is MATPRO [23], which is the one implemented in QLASA, and appears to be one of the most conservative present in literature.

3.3.4 Protection scheme and quench heaters

The first MQXF protection scheme consisted of a 0.048 mΩ dump resistor and quench heaters on the outer layer only. However, first quench protection studies showed that the quench protection safety was almost impossible to reach [24]. Therefore it has been decided to add quench heaters on the inner layer. Detail on the protection considering this configuration can be found in [25]. After that, the parameters of the magnet have been updated, and it has been necessary to update quench heaters and protection study too; details on this last iteration can be found in [26]; for the sake of simplicity, just this last case is reported here and analyzed in details.

MQXF stores very high magnetic energy at operation current (see Table 3.1). Moreover, it is a long magnet, therefore with a large inductance. For these reasons, it is impossible to protect it using just a dump resistor, which is limited by the maximum voltage across the coil ends, and efficient quench heaters are needed. Various designs for the inner and outer layer heaters have been carefully studied and proposed, arriving to the configuration described following.

The outer layer protection heaters are a simple set of simple straight strips that span along the coil and across each (pole and mid-plane) winding block. There are stainless steel heating stations, which have a width of 40 mm and are separated by 120 mm long copper-plated bridges. The design layout is showed in Fig. 3.7.

The inner layer protection heaters are constituted of copper-plated narrow bridges, which connect wide stainless steel heating stations. This design is optimized in order to avoid as much as possible the helium bubbles issue [27]: the magnet inner layer is in direct contact with super-fluid helium, which could penetrate between the heaters strips and the coils; during a quench, the helium evaporates, and it generates bubbles, which reduces the thermal contact between the heater and the coil surface, reducing the heater efficiency, and so increasing the intervention time. The design with narrow bridges allows for more spacing to make perforations, which should help the helium gas to evacuate the coil, and to reduce the pressure. The snake shape allows covering both the mid-plane and the pole blocks. This

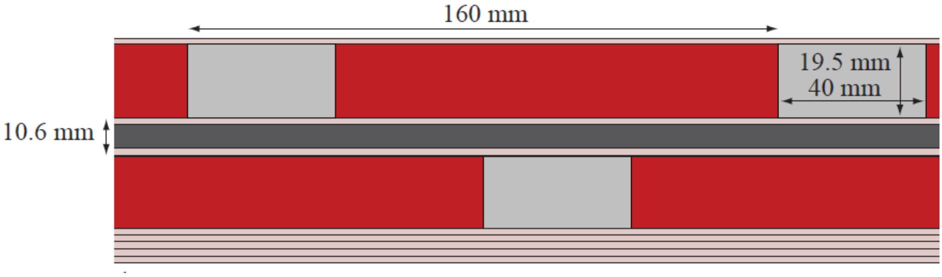

Figure 3.7: Design of the MQXF outer layer protection heaters.

design is showed in Fig 3.8.

The protection heaters efficiency is related to how fast they can induce a quench within the coils after being fired. The delay time depends on the firing voltage, and on the thickness of the insulation (typically kapton) between the heaters strips and the coils surface, which is 50 μm in the case of MQXF. The heaters delay time from firing to induced quench are used in this protection study are showed in Fig 3.9. The values are computed using CoHDA [28], which is a tool developed for the simulation of the heat propagation from heaters to Nb_3Sn coils with FEM methods. For each layer, two average values are reported: one is related to the high magnetic field (HF) zone, which is the pole block, one is related to the low magnetic field (LF) zone, which is the mid-plane block.

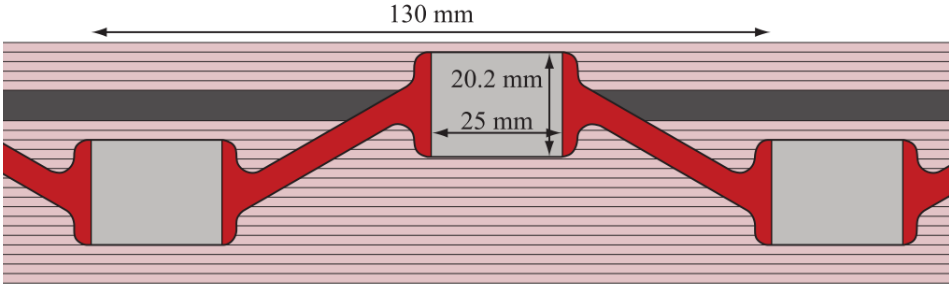

Figure 3.8: Design of the MQXF inner layer protection heaters.

The accurate design of the protection heaters allows inducing quench between 15 and 25 ms from quench validation in all the magnet (delay times at the operation value are reported in table 3.2), resulting in an equilibrated and efficient protection system, which induces an as uniform as possible quench in the whole magnet, reducing the hot spot temperature and maintaining the temperature gradient from resistive zone to superconducting zone under control. A large temperature gradient can be dangerous for the coils, because of the thermal expansion in the warmest zones, which can create local stresses and damage the coils.

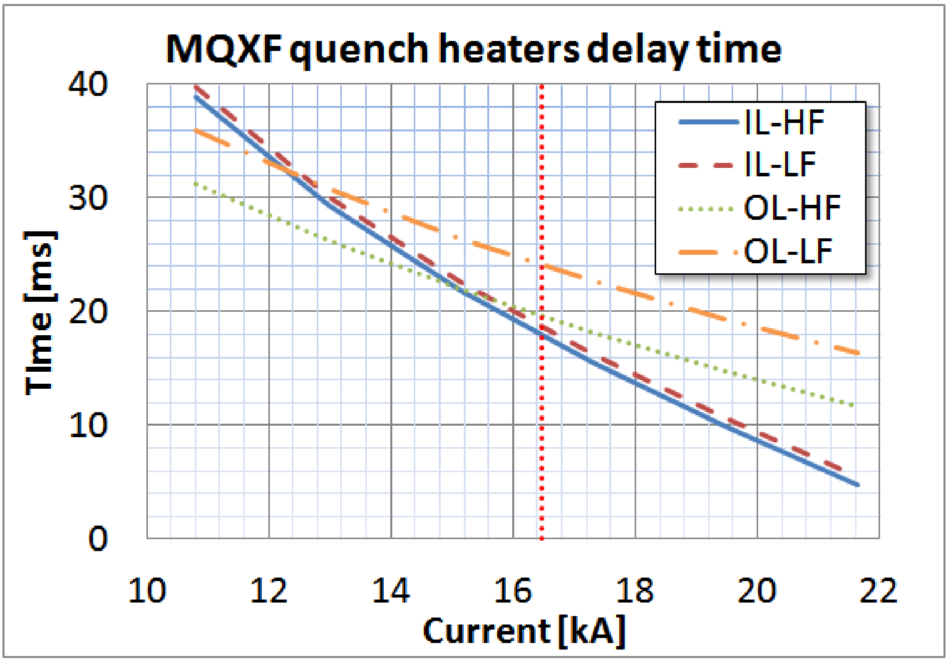

Figure 3.9: MQXF quench heaters delay time as a function of the magnet current. The solid curve shows the inner layer high-field delay time, the dashed curve shows the inner layer low-field delay time, the pointed curve shows the outer layer high-field delay time, the dashed-pointed curve shows the outer layer low-field delay time. The operational values are on the dotted vertical line.

3.3.5 Hot spot temperature computation

The most important analysis to be performed in a quench protection study is the hot spot temperature computation. As just said, an hot spot temperature below 350 K can be considered acceptable, considering also some redundancy of the protection system. The software used for the computation is QLASA, the material properties are from MATPRO.
The main protection parameters are reported in table 3.3. The meaning of the parameters reported in table 3.3 is discussed with details in section 1.5.

MQXF heaters delay time at operating current			
IL-HF	**IL-LF**	**OL-HF**	**OL-LF**
18 ms	18.8 ms	19.5 ms	24.1 ms

Table 3.2: MQXF average heaters delay time at operating current

MQXF protection parameters	
Dump resistor	0.048 mΩ
Voltage threshold	100 mV
Validation time	10 ms
Switch opening delay time after validation	5 ms

Table 3.3: MQXF main parameters

As it can be seen, no dumping resistance is foreseen in this analysis, and quench heaters described in section 3.3.4 have been modeled in QLASA. The assumptions made in the quench modeling are the following:

- the original quench is a point (initial size equal to 0) located in the peak field zone (pole turn). This is the worst case, because the copper magneto-resistance makes the joule dissipation larger in the high-field zone, making the hot spot temperature to grow faster there than in other zones. It is true that the quench propagation velocity and therefore quench detection are faster, but it can be seen that this effect, in this magnet, is less effective than heat generation. For the sake of simplicity, here only the worst case is reported.

- the detection time is computed according to the propagation velocities computed by QLASA, which, as just mentioned, are analytical and based on the Wilson model [1]. The detection time results to be ~ 7 ms in order to reach the 100 mV threshold at nominal current, in the high-field pole turn. The detection time computed by QLASA has been experimentally validated [8].

- the quench heaters delay times used are showed in Fig. 3.9. In the computation, it is assumed that the quench is induced at a different average time in the high-field and in the low-field blocks of each layer. The modeled quench has null radial dimensions, and it is induced only in the turns actually covered by quench heaters. The heating stations are simulated, but pre-heat from the copper-bridges is not considered (this is a conservative assumption: also copper part of the quench heaters produce heat, which propagates within the coils. This heat helps the longitudinal quench propagation, but it can be considered negligible to our purpose). The induced quench propagates in the radial, azimuthal and longitudinal directions according to the propagation velocities computed by QLASA. The way of modeling quench propagation using QLASA is described in [11].

- heat exchange between layers is neglected. In theory, quench should be able to propagate from one layer to the other because of the heat conduction. However, having heaters on both inner and outer layer with similar delay time, this phenomenon becomes negligible. Nevertheless, in the case of heaters failure analysis, this becomes a conservative assumption.

- dynamic effects on the magnet inductance due to the inter-filament coupling currents are taken into account. These effects are largely described with details in chapter 2, and it is expected that they can significantly help the protection study. In fact, coupling currents reduces the magnet inductance, making the current decay faster. A decay time constant τ for the inter-filament current of 25 ms has been used, considering the 19 mm filament twist pitch length.

- quench-back is neglected. This is a conservative assumption, due to the fact that QLASA cannot compute the quench back time. In principle, one could use experimental values from other magnets, however it is preferable to perform a performing protection neglecting this effect, which can be different from one magnet to another.

The quench should be performed considering the connection of the four magnets which constitute the triplet: two magnets have a length of 8.4 m, in the Q1/Q3 position (every cold mass is composed of two magnets with a length of 4.2 m), and two have a length of 7.15 m, in the Q2a/Q2b position. Two possibilities are foreseen for the magnet connections: the first is that Q1/Q3 and Q2a/Q2b are powered separately with two different power supplies (2PS scenario), and each circuit has its own 48 mΩ dump resistor; the other is to power all the 4 triplet magnets together with just one power supply (1PS scenario) and just one 48 mΩ dump resistor. However, because of the large inductance of either the configurations, which makes the dump resistor to extract only few percents of the whole stored energy, the hot spot temperature is very similar in the two scenarios (maximum 5 K difference). For this reason, here only the 1PS scenario is discussed. The resulting current decay is reported in figure 3.10.

Two simulations are reported: one considers the dynamic effects on the magnet differential inductance due to the inter-filament coupling currents, one neglects them. This is to see the effectiveness of this phenomenon, which is being used for protection studies just since few time. It can be seen that the dynamic effects appreciably affect the current decay, but not so much as in the current decays with large dump resistor (see fig. 2.7 for comparison). However, for such a challenging protection study, the help of dynamic effects can be considered useful and not negligible, as we are going to see.

In table 3.4 and 3.5, the MIITs produced during the quench and the magnet hot spot temperature computed by QLASA are reported, considering and neglecting dynamic effects on the inductance respectively.

Three columns are reported for each table: the first one refers to the nominal protection scenario, the second refers to a protection system composed by only quench heaters on the outer layer, and no quench heaters on the inner layer, the last one refers to the nominal situation, but with a failure of all the quench heaters set on the high field zone of the outer layer, which therefore do not induce the quench within the coils.

The first comment is that, in the nominal scenario, the protection of the

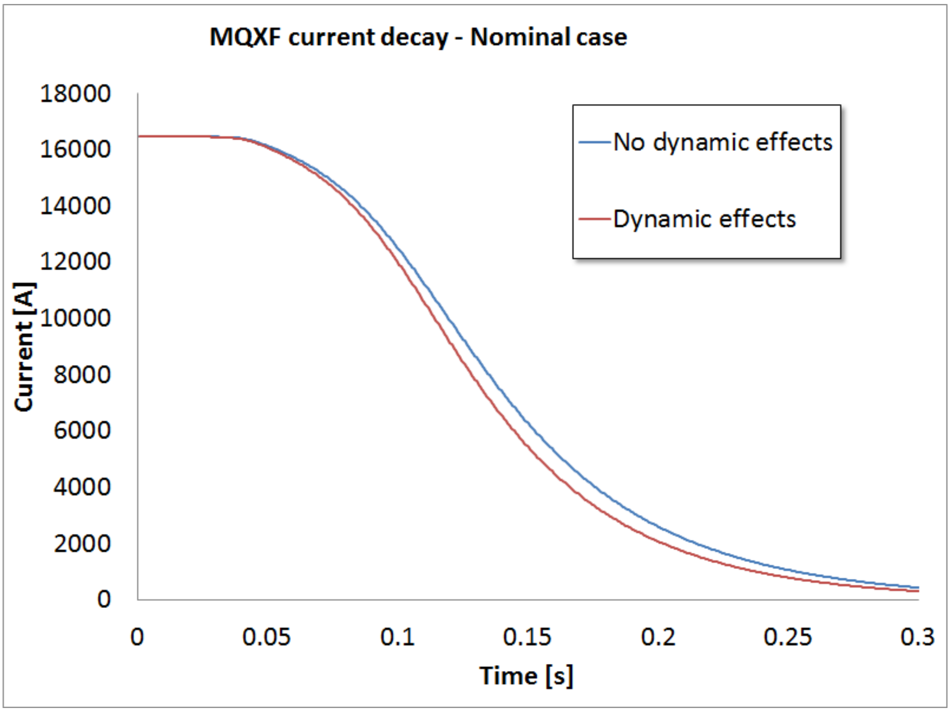

Figure 3.10: Current decay of MQXF after a quench. The blue line is a simulation performed neglecting the inter-filament coupling currents dynamic effects on the differential inductance, the red line is a simulation considering the the inter-filament coupling currents dynamic effects on the differential inductance

magnet is ensured: the hot spot temperature is well below the maximum allowed limit, set to 350 K.
Secondly, comparing table 3.4 with table 3.5, it can be seen that the use of the model considering dynamic effects on the inductance due to inter-filament coupling currents is effective for the magnet protection study: the hot spot temperature decreases of 20-25 K, which is a not negligible amount for such a challenging magnet, despite the current decay is not so different, as shown in figure 3.10. This is due to the fact that the MIITs versus tem-

MQXF hot spot temperature, with dynamic effects		
Nominal	No inner-layer QH	Outer-layer high-field QH fail
28.3 MA^{2}s 257 K	33.6 MA^{2}s 341 K	30.7 MA^{2}s 295 K

Table 3.4: MQXF MIITs and hot spot temperature considering dynamic effect on the inductance. Nominal scenario on the right, no quench heaters on the inner layer in center, failure of all the quench heaters of the outer layer high field zone on the right

MQXF hot spot temperature, no dynamic effects		
Nominal	No inner-layer QH	Outer-layer high-field QH fail
29.4 MA^{2}s 282 K	34.7 MA^{2}s 363K	30.6 MA^{2}s 316 K

Table 3.5: MQXF MIITs and hot spot temperature neglecting dynamic effect on the inductance. Nominal scenario on the right, no quench heaters on the inner layer in center, failure of all the quench heaters of the outer layer high field zone on the right

perature curve has a large slope after 200 K, when it becomes linear and an increase of ∼20 K corresponds to one more MIIT.
Moreover, the second column in both the tables shows that the protection with only quench heaters on the outer layer is almost impossible: despite considering dynamic effects the temperature is formally within the maximum value, it would be impossible to have protection redundancy; if something goes wrong in the protection system (a heater strip does not work, or some adding delay appears), the magnet could be damaged.
The third column, finally, shows that the nominal protection system provides redundancy. For this simulation, it was assumed that all the magnets of the triplets are connected in series (as it will be actually), and that **all** the quench heaters covering the outer layer high-field zone of each magnet fail working correctly, and therefore they do not induce a quench. Consid-

ering that, for each magnet, there are two heater strips in the outer-layer high-field zone, it means that this scenario assumes a failure of 12 heater strips all together, which is a very unlikely event; nonetheless, the hot spot temperature reaches less than 300 K, therefore the protection system can be considered redundant. Varying the combination of heaters failure leads to similar results on the hot spot temperature point of view; this aspect will be discussed in details in the voltage analysis, in the next section.
The protection system of MQXF presented here allows maintaining the hot spot temperature under control, and ensures redundancy. However, inner layer protection heaters are necessary, and the issue of helium bubbles is not completely solved. For this reason, a protection system constituted by outer layer heaters and CLIQ units [29], without dump resistor, is under study, as alternative to the one presented here.

3.3.6 Voltage analysis

Another important study to be performed in quench protection analysis is the peak voltages evaluation. During a quench, large voltage differences can appear within a superconducting magnet, due to the difference of resistance between various zones. These voltage differences can be dangerous, because, if they reach the maximum voltages carried by the cable or coil insulation, they can cause short circuits or even coil damages. This study is therefore very important to design and test the cable and coils insulation.
The following voltage differences will be analyzed:

- Peak voltage: it is the maximum voltage (in absolute value) reached by the magnet respect to the point set to ground. In a single magnet, typically, one end is set to ground; however, in a string of magnet such as the triplet, the peak voltage depends on where the ground has been placed, therefore its position is important to minimize this value, as we are going to see.

- Turn to turn voltage (T-T in tables): it is the voltage difference which appears between two adjacent conductors of the same layer. It is due to the resistive plus inductive voltage which is accumulated in one winding. It is important for the sizing of the cable insulation.

- Layer to layer voltage (L-L in tables): it is the voltage difference which appears between two adjacent conductors belonging to different layers. It is due to the voltage drop which is accumulated in all the winding between them. It is important for the sizing of the inter-layer insulation.
- Mid-plane to mid-plane voltage (M-M in tables): it is the voltage difference which appears between two adjacent conductors belonging to different coils. It is due to the voltage which is accumulated in one whole coil. It is important for the sizing of the mid-plane insulation.

This study has been performed using ROXIE [12] [13], which allows analyzing the voltages of each turn during a quench, depending on the current and its derivative, on the resistance, and on the magnetic field. The ROXIE output is managed using a MATLAB program developed *ad hoc.*
The assumptions are basically the same made for the hot spot temperature calculation (see section 3.3.5), except that heating station are not simulated, and dynamic effects on the inductance are not taken into account; these two features, in fact, are not present in ROXIE, and QLASA is not suitable for such a detailed analysis on voltages.
The simulations compare the scenarios considering one or two power supplies. In fact, the peak voltage,as just said, depends on where the ground has been set, and on the number of magnets which are in series. The two scenarios have to be compared in order to verify whether both of them present acceptable values. Instead, the turn to turn, layer to layer, and mid-plane to mid-plane voltages do not depend on the number of magnets in series (they are internal differences), but they depends on the magnet length; therefore, they will be evaluated just for the longer version of the magnet (7.15 m), which will be inserted in Q2a/Q2b (see table 3.1)
The nominal case is compared to a large amount of possible quench heaters failure situations. Contrary to the hot spot temperature evaluation, for this analysis the consideration of different failure scenarios is very impor-

tant, because the main responsible of large voltage difference is the series of superconducting and resistive zones, which makes the voltage to oscillates from one turn to another. The lack of just one heater strip can induce a small hot spot temperature difference, but a large turn to turn voltage, for example.
The results are listed in Table 3.6 for the 1PS scenario, and in Table 3.7 for the 2PS scenario. As just mentioned,in the 2 PS scenario values are reported only for Q2a/Q2b magnet (7.15 m).

The cases considered, from the top to the bottom of the tables, are:

- nominal case: in this case, all the protection heaters work and induce quench;
- only outer layer quench heaters: in this case, only outer layer protection heaters are present, while inner layer protection heaters are not activated;
- failure of all the quench heaters of the first coil: in this case, all the heaters of the first coil of a magnet of the series do not work. This is an unlikely scenario, involving six heater strips;
- failure of all the quench heaters of the third coil: this case is similar to the the previous one, but the not protected coil is the third one;
- failure of the outer layer quench heaters of the high-field (pole) blocks, in all the coils: in this case, all the quench heaters posed on the high field block of all the four coils of a magnet of the series do not work. This could happen only in the outer layer, because, as it can be seen in figure 3.7 and 3.8, in the outer layer the high-field and low-field heaters are powered separately, while in the inner layer they are connected together in a snake shape. However, also this is an unlikely scenario, which involves four heater strips;
- failure of the inner layer quench heaters of the first coil: in this case, the inner layer quench heaters of just the first coil of one magnet of

MQXF peak voltages, 1PS scenario					
	TG [V]	TG(sc) [V]	T-T [V]	L-L [V]	M-M [V]
Nominal	638	838	46	454	148
OL-QH	757	1007	86	549	146
Coil 1 fail	1862	2092	62	1734	1701
Coil 3 fail	1463	1693	63	1747	1832
OL-HF fail	738	958	66	239	148
Coil 1 IL fail	662	872	49	522	356
Coil 3 IL fail	663	873	50	527	482
Coil 1 OL-HF fail 1 side	608	813	48	487	159
Coil 3 OL-HF fail 1 side	608	813	47	490	275
Coil 1 OL-LF fail 1 side	597	802	47	472	147
Coil 3 OL-LF fail 1 side	582	787	47	472	176

Table 3.6: Voltage analysis for the 1 power station scenario for the MQXF protection system (all the triplet magnets are connected in series with a 48 mΩ dump resistor).

MQXF peak voltages, 2PS scenario					
	TG [V]	TG(sc) [V]	T-T [V]	L-L [V]	M-M [V]
Nominal	659	859	44	421	313
OL-QH	798	1048	81	509	311
Coil 1 fail	1810	2020	59	1674	1513
Coil 3 fai	1335	1565	59	1686	1769
OL-HF fail	833	1053	62	223	312
Coil 1 IL fail	754	964	47	486	342
Coil 3 IL fail	755	965	47	490	494
Coil 1 OL-HF fail 1 side	704	909	45	452	314
Coil 3 OL-HF fail 1 side	704	909	45	455	314
Coil 1 OL-LF fail 1 side	680	885	45	439	312
Coil 3 OL-LF fail 1 side	681	886	45	439	313

Table 3.7: Voltage analysis for the 2 power station scenario for the MQXF protection system (Q1/Q3 and Q2a/Q2b magnets are connected separately in series with their own 48 mΩ dump resistor).

the series do not work. This scenario is realistic, because it is a failure of just two heater strips, considering also the helium bubbles issue;

- failure of the inner layer quench heaters of the third coil: this case is similar to the the previous one, but it is related to the third coil of one magnet of the series;
- failure of the outer layer quench heaters of the high-field (pole) block of the first coil, just one side: in this scenario, the protection heaters of the high-field block of the outer layer of the first coil of a magnet do not work; moreover, just one side of the coil is involved (i.e. one octant of the magnet), because, in the outer layer, heaters on each side of a coil are powered separately; therefore, this scenario is realistic, because it is a failure of just two heater strips in the magnet series;
- failure of the outer layer quench heaters of the high-field (pole) block of the third coil, just one side: this case is similar to the the previous one, but it is related to the third coil of one magnet of the series;
- failure of the outer layer quench heaters of the low-field (mid-plane) block of the first coil, just one side; in this scenario, the protection heaters of the low-field block of the outer layer of the first coil of a magnet do not work; moreover, just one side of the coil is involved. This scenario is realistic, because it is a failure of just two heater strips in the magnet series;
- failure of the outer layer quench heaters of the low-field (mid-plane) block of the third coil, just one side: this case is similar to the the previous one, but it is related to the third coil of one magnet of the series.

For each case, five values are reported, from left to right:

- the first is the nominal voltage to ground: this number is computed considering symmetric grounding, i.e. ground positioned in the middle of the magnets in series; this should limit the peak voltage, respect to set the ground at the beginning or at the end of the series;

- the second is the voltage to ground with a short circuit (sc) of the symmetric ground: in this case, a failure of the symmetric ground is simulated; this means that the beginning or the end of the series is considered to ground;
- the third is the maximum turn to turn voltage;
- the fourth is the maximum layer to layer voltage;
- the fifth is the maximum mid-plane to mid-plane voltage.

The first comment is that, comparing the 1PS and 2PS scenarios, it is evident that they are almost equivalent; the main difference is that, in some failure cases, the mid-plane to mid-plane voltage doubles in the 1PS scenario; however, these failure scenarios are possible. Nonetheless, these values can be considered acceptable, because, using suitable mid-plane insulations, voltages until 500 V can be faced with no issues. Considering that all the other voltages do not appear critical, except that for largely unlikely failure scenarios, the 1 PS appears more convenient, because, sizing appropriately the mid-plane insulation, it allows to save some power supplies without having particular voltage issues.

The To Ground (first and second) columns need a comment: presently, ROXIE allows simulating only one magnet in a series, and not the whole series. This means that the simulations have been performed considering a magnet alone, with a dump resistor dimensioned in order to have the right voltage fall across the magnet ends. Then, the voltage to ground is obtained adding the actual magnet ends input voltage, considering the magnet is inserted in the chain, to the simulated voltage. For example, considering that the voltage across the dump resistor is 800 V at the beginning of the decay, in the 1 PS scenario, a voltage of 600 V has to be added to the third magnet simulated voltage in order to obtain the actual one, and so on. For this reason, the failure scenarios represent the magnet with a failure in a series of well working magnets, and the case of failures in different magnets cannot be simulated.

Moreover, this assumption causes an error on the to-ground voltage evaluation, of the order of the resistance ratio between failure scenario and nominal case: in fact, the failure causes a voltage unbalance between the magnets in series, because of the different resistance of the magnets. For example, consider the case of four identical magnets, with the same resistance, in series with a dump resistor; it is obvious that the voltage drop across the dump resistor is divided equally by four on each magnet. Now, if one of the magnet has a bit less resistance than the others, instead of having one fourth of the voltage drop, it will have a bit less, while the other three the same bit divided by three more. For this reason, in the voltage evaluation, we overestimate a bit the voltage drop across the magnet, but, however, it is a conservative and even small error, therefore we can accept it.

3.3.7 Conclusions

The protection of MQXF has been a significant challenge in the first stage of the design process. A first series of studies showed that a standard protection approach composed of energy extraction and outer layer quench heaters was not sufficient to ensure magnet safety. This result led to improve the design of quench heaters, including them on the inner layer; the design of inner layer heater has been performed in order to find possible ways to avoid the helium bubbles issue.
The current decay behavior has been studied in details during every iteration of this analysis, leading to the development of an electromagnetic model for the simulation of the inductance dependence on the inter-filament coupling currents which has been described with details in chapter 2. In fact, this model has been developed exactly in order to perform more accurate simulations for the MQXF protection study, and now it is ready to perform quench analysis of other challenging magnets.
The magnet parameters have been upgraded, increasing the margin to the short sample limit. This work shows that, with all these innovations, MQXF protection is possible, with a good margin on the uncertainties (such as material properties), and with a good redundancy in the case of possible failure scenarios. The hot spot temperature is under control, and the peak voltages do not appear worrisome.

Moreover, we have shown that using just one power supply for the protection of the whole triplet is a safe option, because both hot spot temperature and peak voltages are acceptable, and it could be considered in order to reduce costs.

The last open issue is the inner layer quench heaters reliability because of the helium bubbles. The first quench tests on the first MQXF coils are currently under way, and some indications on this issue will be available soon. If it will not be solved, the option of using CLIQ with only outer layer quench heaters and no dump resistor should be taken into account. Tests like the last one are in fact foreseen and being performed soon.

Chapter 4

Design and protection of a 16 T cosθ bending dipole for the Future Circular Collider (FCC)

4.1 FCC and EuroCirCol

After LHC will be turned off, more energetic accelerator machines will be needed in order to explore unknown regions of high-energy physics. For this reason, at CERN the project *Future Circular Collider* (FCC) has started [30]. The aim of FCC is to build a circular collider on the CERN site, with a circumference of 100 km, after 2050. Three phases of the machine are foreseen: an electron-electron collider (FCC-ee), an electron-proton collider (FCC-eh), and a proton-proton collider (FCC-hh). In particular, for the last one, proton beams with an energy of 50 TeV per beam are expected, in order to provide collisions of 100 TeV in the center of mass reference system. It is easy to verify that, maintaining the present LHC filling factor for the bending dipoles, in order to accomplish the machine size and energy, the development of bending dipoles able to operate at 16 T will be needed.

The design of such magnets is a challenge for the present technology.
In this framework, the *EuroCirCol* project was born [31]. EuroCirCol is a project founded by the European Community, which aims to develop a conceptual design of FCC within 2020. Between the several activities, one of the most important is the design of a bending dipole able to provide an operating magnetic field of 16 T. This magnet has to be a superconducting magnet; in particular, the material chosen to design the magnet is Nb_3Sn. Presently, LHC has NbTi superconducting dipoles; however, this material cannot reach such an operating magnetic field, because it overcomes its critical field. High temperature superconductors are not considered ready for the design of long, high-field accelerator magnets, therefore Nb_3Sn is the best material that the technology can provide today. However, contrary to NbTi, Nb_3Sn is a novel technology for high-field accelerator magnet, as just said in the chapter 3; moreover, in order to reach 16 T with a reasonable amount of conductor, it has to be exploited at its highest current performances. For these reasons, the design of such a magnet is a challenge for the magnet community.
A dedicated working package (WP5) has been instituted in the EuroCirCol collaboration for the design of a 16 T bending dipole for FCC. Within this collaboration, three different magnetic layouts are being considered: a common coil design, a block coil design, and a $\cos\theta$ design; each layout is responsibility of a dedicated team. The INFN Milano and Genova team is responsible of the design of the $\cos\theta$ version of the magnet. In this chapter, we describe the magnetic design, mechanical design and the quench protection of the $\cos\theta$ 16 T dipole developed by the INFN team within the EuroCirCol collaboration.

4.2 Design of a 16 T $\cos\theta$ dipole operating at 4.2 K at 90% of the load line

In this section, we present the design of a 16 T $\cos\theta$ superconducting magnet which operates at 4.2 K, at the 90% of the load line [32]. The load line is the function that represents the magnetic field produced in the bore of a magnet as a function of the current; typically, in a superconducting magnet this function is linear. The load line of a superconducting magnet crosses the critical surface; the intersection point depends on the temperature of the magnet, because its critical surface does. This point represents the maximum current that the magnet can carry; after that, a quench certainly occurs. Obviously, a superconducting magnet cannot work at its maximum current, because the slightest disturbance could induce a quench; therefore, the design of a magnet foresees an operating point, which is the percentage on the load line at which the magnet is assumed to work. This means that the magnet described here has to produce 16 T carrying a current equal to the 90% of the maximum current it can carry at 4.2 K.

4.2.1 Design constraints

In order to compare the different layouts, a set of design parameters has been discussed and approved by the EuroCirCol collaboration. The parameters chosen aim to combine technology foreseen development with magnet feasibility. The set of parameters is shown in table 4.1. We just want to point out that the magnet layout has two apertures for the beams such as the present LHC magnets.
Another important feature that has been discussed is the critical current: this is an important parameter for the design, because it defines the maximum current that the magnet can take, and consequently the amount of conductor needed. For the development of such a large machine, reducing the conductor is one of the most important acts to do in order to save costs. Considering that the Nb_3Sn is a technology under development, and that first prototypes of the EuroCirCol magnet will not be build within 5 years, it has been decided to use as critical current the one expected in the next few years for high performance Nb_3Sn strands[33]. The target is to reach in the superconductor a current of 1500A/mm^2 at 16 T, with a temperature of 4.2 K. The complete critical current is reported in figure 4.1

Main design paramenters	
Bore inner diameter	50 mm
Beam distance	250 mm
Bore nominal field	16 T
Operating temperature	4.2 K
Operation on load-line	90 %
Maximum strand number	40
Insulation thickness	0.15 mm
Cu/NCu	≥ 1
Field harmonics (geo/sat)	≤3/10 arbitrary units
Iron yoke outer radius	400 mm
Aperture number	2

Table 4.1: Main design parameters for the comparison of the three magnet layouts.

4.2.2 Magnetic design

The layout

The magnetic design has been performed using ROXIE [12] [13]. In Fig.4.2 the whole cross-section layout is shown together with iron yoke, and the field within the iron. Instead, in Fig. 4.3 just one quadrant of the magnet is shown, presenting the details of the windings arrangement, and the magnetic field within the coils. As just mentioned, the layout is based on a cosine-theta magnet. In particular, a layout with four layers of conductors has been chosen. This is a compromise between maximum number of strands available in a cable (see table 4.1), and the amount of conductor. In fact, the cable used for the first two layers is different from the cable used for the last two layers, which is smaller. This is a technique commonly used in superconducting magnets, called *grading*: within a coil, the magnetic field in the zones far away from the bore is smaller, therefore, at the same current, a smaller cable can be used in order to obtain a larger current

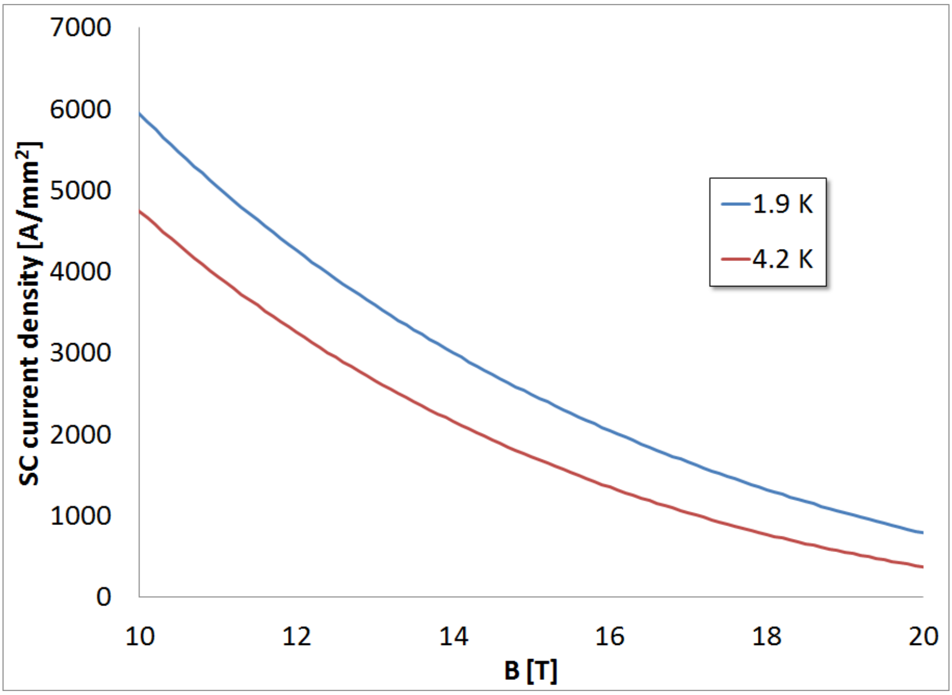

Figure 4.1: Superconductor critical current for the design of the EuroCirCol magnets.

density and to produce a larger magnetic field, optimizing the conductor needed. The number of turns for each layer is shown in Table 4.2. The large amount of wedges between the blocks (11 per quarter magnet) helps reducing the peak field on the coil, besides having more freedom to adjust the field quality. However, this could be a complication for the construction of the magnet.

As just said, in order to minimize the superconductor cross section area, grading between layer 2 and 3 is foreseen. This means that the coils can be assembled as two classic double pan-cakes connected on the mid-plane, which is the standard and well known manufacture process used for cosine-

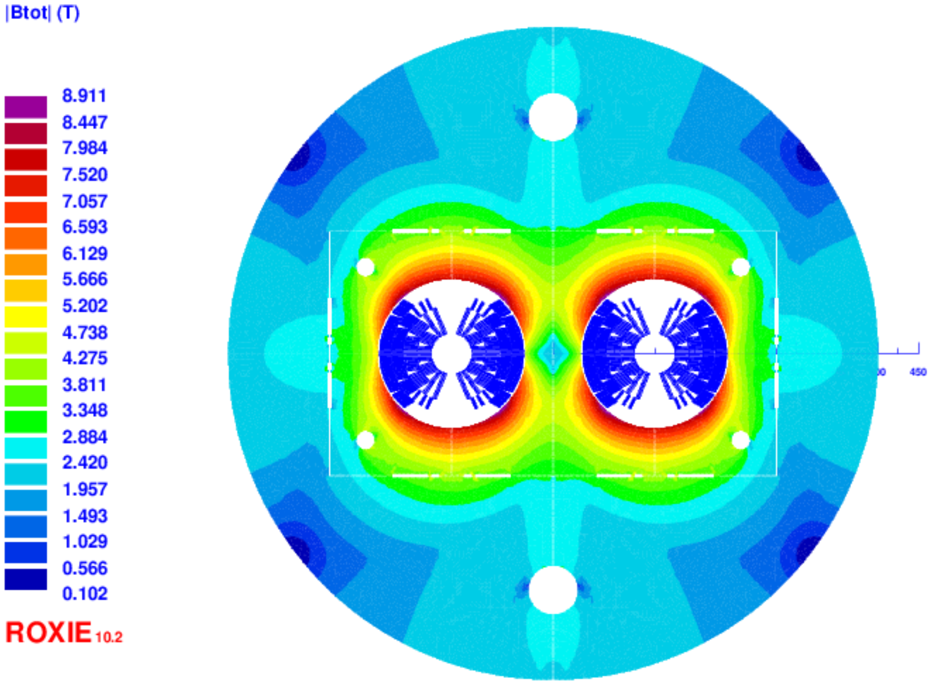

Figure 4.2: Cross-section layout of the EuroCirCol cos θ and magnetic field within the iron yoke

theta magnets; in practice, a double pan-cake consist of a coil constituted by two layers, with connection for other coils on the mid-plane, in order to obtain a four, six, eight etc... magnet. Presently, only Nb_3Sn cos θ design with an even number of layers are considered feasible, because connection on the pole are not possible for the conductor brittleness.

The coil peak field is 16.4 T, and it is in the bottom-left corner of pole turn into the first layer. The minimum bending radius for the windings is 6.4 mm.

Table 4.3 reports the properties of both the cables are reported. HF (High Field) Cable refers to the cable used in the first and the second layer, while

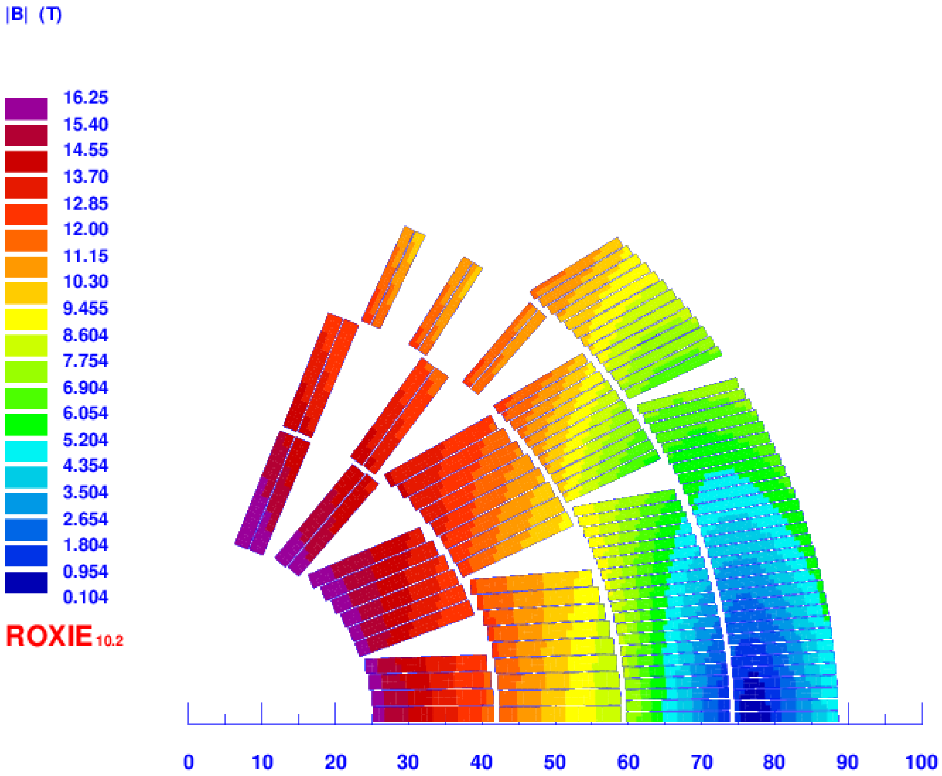

Figure 4.3: Detail of the windings arrangement of the EuroCirCol $\cos\theta$ and magnetic field within the coils

LF (Low Field) Cable refers to the third and the fourth layer. A comment which we want to underline is that both the cables work at 90% of the load line; this means that they are optimized as much as possible, exploiting the grading in order to save the largest amount of conductor.

Figure 4.4 shows in detail the margin on the load line of the magnet. Obviously, the two conductors have different load-lines (they have different current density!) in order to stay at 90% of the maximum current density that they can carry.

Number of turns	
Layer 1	14
Layer 2	21
Layer 3	37
Layer 4	43
Total	230 per aperture

Table 4.2: Number of turns for each layer of the EuoroCirCol $\cos\theta$

Conductor properties		
	HF Cable	**LF Cable**
Strand number	28	38
Strand diameter	1.1 mm	0.7 mm
Bare width	16.5 mm	14 mm
Bare inner thickness	1.892 mm	1.204 mm
Bare outer thickness	2.036 mm	1.326 mm
Insulation	0.15 mm	0.15 mm
Keystone angle	0.5^o	0.5^o
Cu/NCu	1	2
Operating current	10275 A	10275 A
Operating point on load line (4.2 K)	90 %	90 %

Table 4.3: Conductor properties of both the cables used for the design of the EuroCirCol $\cos\theta$

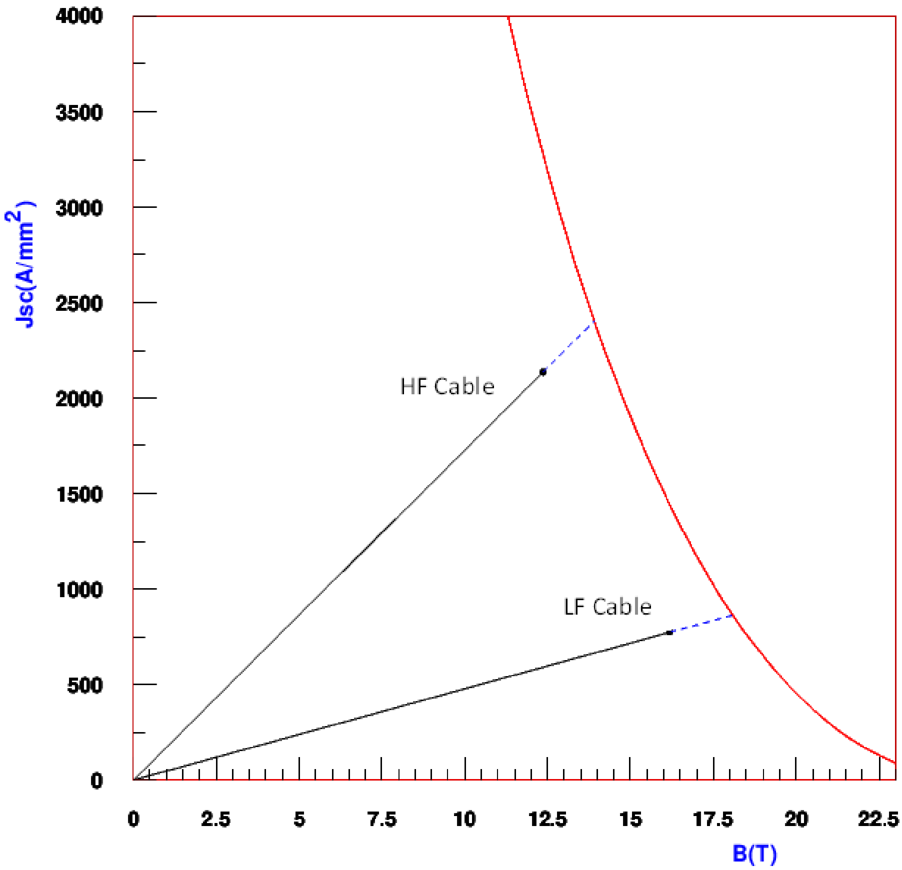

Figure 4.4: Load line of the EuroCirCol cos θ magnet, for the LF and HF conductor

Looking at table 4.3, an evident difference which appears between the two conductors is that LF cable has an appreciably higher copper content than HF cable (Cu/NCu is 2 instead of 1); it is important to point out that this high copper content is due to protection reason, as will be discussed in section 4.2.4.

Inductance and energy	
Inductance	25 mH/m/aperture
Stored energy	1.5 MJ/m/aperture

Table 4.4: Inductance and stored energy of the EuoroCirCol $\cos\theta$

Looking at Fig. 4.2, it can be seen that the mechanics of the magnet assumes a mechanical structure based on a *bladders and keys* solution [34]. However, it has not any mechanical meaning; today, the purpose of the collaboration, regarding the mechanics of the magnet, is designing a structure for a **one aperture** magnet, as discussed in details in section 4.2.3, foreseeing the construction of a first prototype with one aperture. The choice made here aims to look at the effect of the iron very close to the coils, which helps to produce the needed magnetic field with a lower current, therefore with less conductor at the same margin. In Table 4.4 inductance and stored energy are indicated for such an iron configuration.

Field quality

An accelerator magnet needs a very good field quality, in order to ensure a particle beam with the properties required by the experiments. In order to ensure the field quality, field harmonics are evaluated within a diameter equal to 2/3 of the magnet aperture. Field harmonics are basically the undesired components of the field, which always are present in a magnet. In our case, for example, we would like a perfect dipole field; however, there will be a component of each other harmonics possible for a magnetic field, such as the quadrupole, the sextupole, the octupole, etc... (for the magnetic field, only even components are possible, because the magnetic monopole does not exist). However, it is possible to tolerate a certain quantity of these harmonics, as reported in Table 4.1. The field harmonics are evaluated in arbitrary units, which are equivalent to 1/10.000 of the main field. For example, a field harmonic of 1 unit means that the relative field component

Odd harmonics					
b3	b5	b7	b9	b11	b13
-0.01	0.97	-0.87	0.28	0.66	-0.13

Table 4.5: Even harmonics of the EuoroCirCol $\cos\theta$

Even harmonics					
b2	b4	b6	b8	b10	b12
-19.94	-0.49	-0.01	0.00	0.00	0.00

Table 4.6: odd harmonics of the EuoroCirCol $\cos\theta$

is 0.01% of the main magnetic field (in this case, the dipole).
As reference baseline, the field harmonics have been set to be less than 3 at the operation field (geometric harmonics), less than 10 at the injection field (saturation harmonics), as indicated in Table 4.1. Geometric harmonics are due to the windings arrangements, while saturation harmonics are due to the fact that the iron saturates while increasing the current, producing a not linear magnetic field. The last ones are important during the injection phase of the machine. Table 4.5 and 4.6 report the field harmonics at the nominal field, while Fig. 4.5 shows the main harmonics as function of the bore field.

In this specific case, the even harmonics are due to the cross-talking between the two apertures. The oscillation of b3 in Fig. 5 is due to the iron saturation, as just explained.
Looking at table 4.1, it is easy to note that the requirements on the field quality are accomplished by this magnet, except b2, which is about 20 at nominal field. By the way, at this stage of the design, the optimization of b2 has not been performed; in future studies b2 will be corrected with holes in the iron, or with asymmetric coils, if it will be required, such as done for the HiLumi D2 [35].

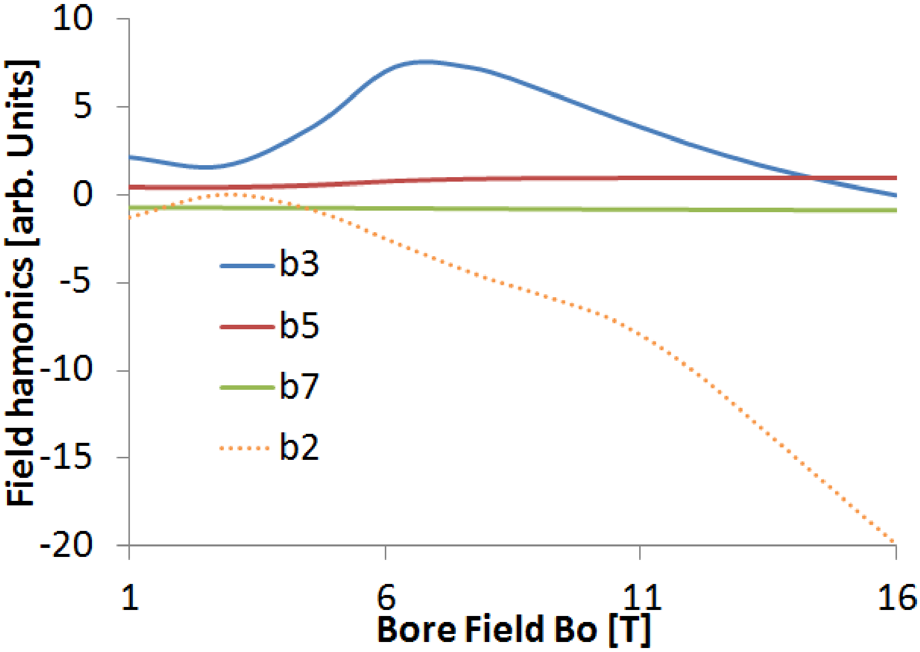

Figure 4.5: Field harmonics as a function of the bore field

Strand area and amount of conductor

The evaluation and minimization of the strand area is very important, because about 4600 dipole units with a length of 14.3 m will be inserted in FCC [31], therefore even a small variation of the conductor area means a huge difference in terms of cost. Table 4.7 indicates the strand area computed for this magnet using the set of parameters reported in Table 4.3, and the values used for the calculation. The total strand area for a double aperture magnet is then 168.1 cm^2, whence a total conductor weight of 9.6 ktons can be calculated for the whole FCC.

A possible alternative solution can be considered in order to reduce the superconducting strand area for this magnet: in Table 4.3 is reported that

Strand area	
Number of dipole units (FCC)	4578
Dipole length	14.3 m
Conductor density	8.7 kg/dm3
Strand area (2 apertures)	168.1 cm^2
Total conductor weight	9.6 ktons

Table 4.7: Strand area and FCC weight estimation for the EuroCirCol $\cos\theta$.

for the low field cable the ratio Cu/NCu is 2; remembering that this high copper content is for protection reason, it is possible to distribute the copper in a different way, cabling 25 superconducting strands with Cu/NCu=1 together with 13 pure copper strands, such as shown in Fig. 4.6. Using this solution, stability is ensured (the Cu/NCu is the same as in HF cable), and the total content of copper is not changed, but only distributed in a different way, therefore also on the quench protection point of view there is not difference. Instead, the cost of the cable can change significantly: in fact, in Table 4.8 the total superconducting strand area using this option is indicated. A similar solution has been adopted for the development of the magnet presented here [36], and the mechanical properties of such a cable have been studied here [37]. The pure copper strand area has to be added in order to obtain the old value of 168 cm^2. By the way, because in terms of costs the manufacturing process is more expensive than materials, the cost of superconducting strands is almost independent on the Cu/NCu value. Therefore, because pure copper strands cost less than

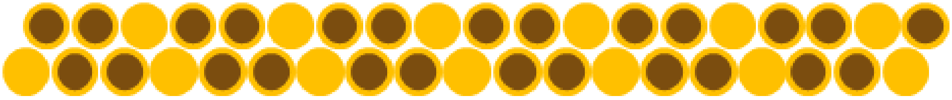

Figure 4.6: Alternative option for the low field cable . Superconducting strands are represented as brown circles with a yellow jacket, pure copper strands are represented as yellow circles

Strand area	
Number of dipole units (FCC)	4578
Dipole length	14.3 m
Conductor density	8.7 kg/dm3
Strand area (2 apertures)	136 cm^2
Total sc-conductor weight	7.8 ktons

Table 4.8: Strand area and FCC weight estimation for the EuroCirCol $\cos\theta$, using the alternative conductor for the low field cable represented in Fig. 4.6

superconducting strands, this solution allows to save about 20% of the cost. It is important to study in the future the possible issues of this solution (current distribution during a quench, mechanical properties of the cable, thermal contraction during reaction, etc...) in order to assess its feasibility.

4.2.3 Mechanical design

The main purpose of a mechanical structure for a superconducting magnet, beside mechanical stability, is to avoid movements of the conductors: the motion of a cable, because of the friction, could provide enough heat to induce a quench inside the magnet. In particular, it is important to maintain the contact between the pole turn of the coils and the pole of the magnet. In fact, because of the lorentz forces, a dipole tends to detach from the poles, leaving the conductors free to move. In order to avoid this, the mechanical structure has to provide *azimuthal pre-stress* to the coils: briefly, during the assembly, cool-down and energization of the magnet, the structure presses the coils against the pole, avoiding its detachment.
In this section, the mechanical layout designed for the EuroCirCol $\cos\theta$ is shown.

The B&K layout

The mechanical structure chosen for the magnet is based on a bladders and keys (B&K) option [34], but some modifications have been made to the original version. Bladders and keys is a new technology used for example for the assembly of HiLumi and Larp quadrupole magnets [20], and there are not previous designs for $\cos\theta$ dipoles in the literature. The solution is shown in Fig. 4.7. It is easy to note that the mechanical design is for a single aperture magnet. This is related to the fact that this would be the first attempt of bladders and keys on a $\cos\theta$ magnet, therefore starting from a more complicated design for a double aperture magnet could be deleterious. Moreover, forces on the mechanical design have been focused on the development of a EuroCirCol prototype in 2021, which will be a single aperture magnet. In the future, the design of a double aperture mechanical structure will be performed, once the single aperture structure will reach a reasonably reliable configuration.

The bladders and keys structure is composed by an iron pad close (2 mm) to the coils, a stainless steel insert for the insertion of bladders and keys (two vertical keys, one horizontal key), an iron yoke with 275 mm diameter and a 70 mm aluminum shell. In order to balance better the azimuthal pre-stress on the coils during the-cool down, undercuts in the first and third layer are foreseen in the titanium nose (the component with whom the pole turn is in contact, in order to have mechanical stability), and a 0.4 - 0.2 mm tapered shim is inserted in the mid-plane. These are the modifications made to the standard B&K structure, which alone cannot provide enough pre-stress to the coils.

Mechanical properties and acceptance criteria

The mechanical analysis has been performed using ANSYS. The mechanical properties of the materials inserted in the simulations and their stress limits are presented in Table 4.9 and 4.10, at operating and at room temperature respectively [38]. The goal of the design is to maintain the pole-coil contact when the magnet is fully energized, producing 16 T, and to keep stresses

Material properties at 4.2 K				
Material	**Max stress [MPa]**	**E[GPa]**	ν	α **[x10$^-$3]**
Coil	200	E$_x$=52, E$_y$=44, E$_z$=21	0.3	α_x=3.1, α_y=3.4
Al shell	690	79	0.3	4.2
Iron	720	224	0.28	2.0
Ti Pole	1650	130	0.3	1.7

Table 4.9: Material properties used for the mechanical analysis at operating temperature (4.2 K).

Material properties at 293 K				
Material	**Max stress [MPa]**	**E[GPa]**	ν	α **[x10-3]**
Coil	150	E_x=52, E_y=44, E_z=21	0.3	α_x=3.1, α_y=3.4
SL steel	350	193	0.28	2.8
Al shell	480	70	0.3	4.2
Iron	180	213	0.28	2.0
Ti Pole	800	130	0.3	1.7

Table 4.10: Material properties used for the mechanical analysis at room temperature (293 K).

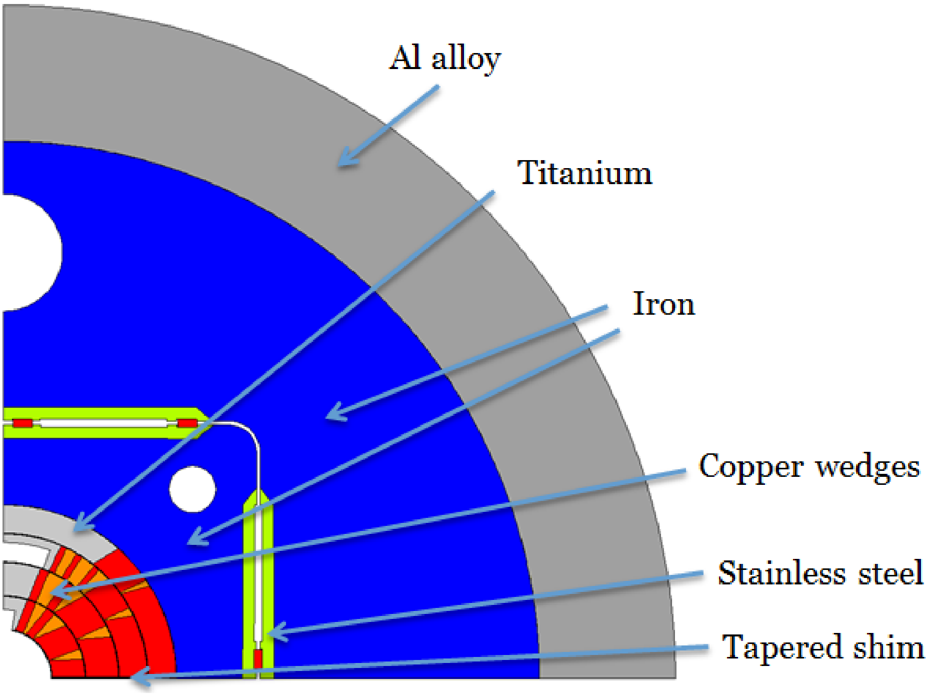

Figure 4.7: Mechanical structure of the EuroCirCol $\cos\theta$

within limits shown in Table 4.9 and 4.10 during assembly, cool-down and energization. In particular, the following acceptance criteria have been considered:

- The contact pressure in the midpoint between the pole and the coil has to be larger than 2 MPa after energization;
- The maximum pressure provided by the bladders for the keys insertion is 50 MPa;
- The maximum displacement provided by the bladders is 100 μm;
- Iron at 4.2 K becomes brittle, therefore σ_1 (the tension part of the

stress) has to be lower than 200 MPa.

These numbers have been discussed within the EuroCirCol collaboration, and they are intended to compare the designs with the same assumptions. In particular, the numbers have been decided following the HiLumi experience [20]. The discussion on these numbers can be found in [38].

Assembly

During the assembly, a part of the stress in the coils comes from the keys interference with the structure, and a part from the interference of the tapered shim in the mid-plane with the coils. The Von Mises stress during this phase is shown in Fig. 4.8. The scale of the plot has been locked to the maximum stress allowed, which is 150 MPa as indicated in Table 4.10. It can be seen that a not negligible part of the coil (the grey zone) overcomes this number, which means that in this area the conductor could suffer degradation.

Cool-down

During the cool down, the aluminum shell shrinks because of the thermal contraction. Because of the different thermal contraction constants of the involved materials, the remaining part of the needed azimuthal pre-stress is given during this process. The Von Mises stress within the coils is reported in Fig. 4.9 Noting that the plot scale has been updated and locked to 200 MPa, which is the maximum allowed stress at operating temperature (4.2 K) as shown in Table 4.9, there is no evidence of issues during this phase.

Energization

After the magnet is fully energized, it is important to maintain the pole in contact with the coil. In fact, as just mentioned, because of the Lorentz forces, the coil tends to crush on the mid-plane, and to detach from the pole; the resulting movements of the turns can induce a quench, and in the

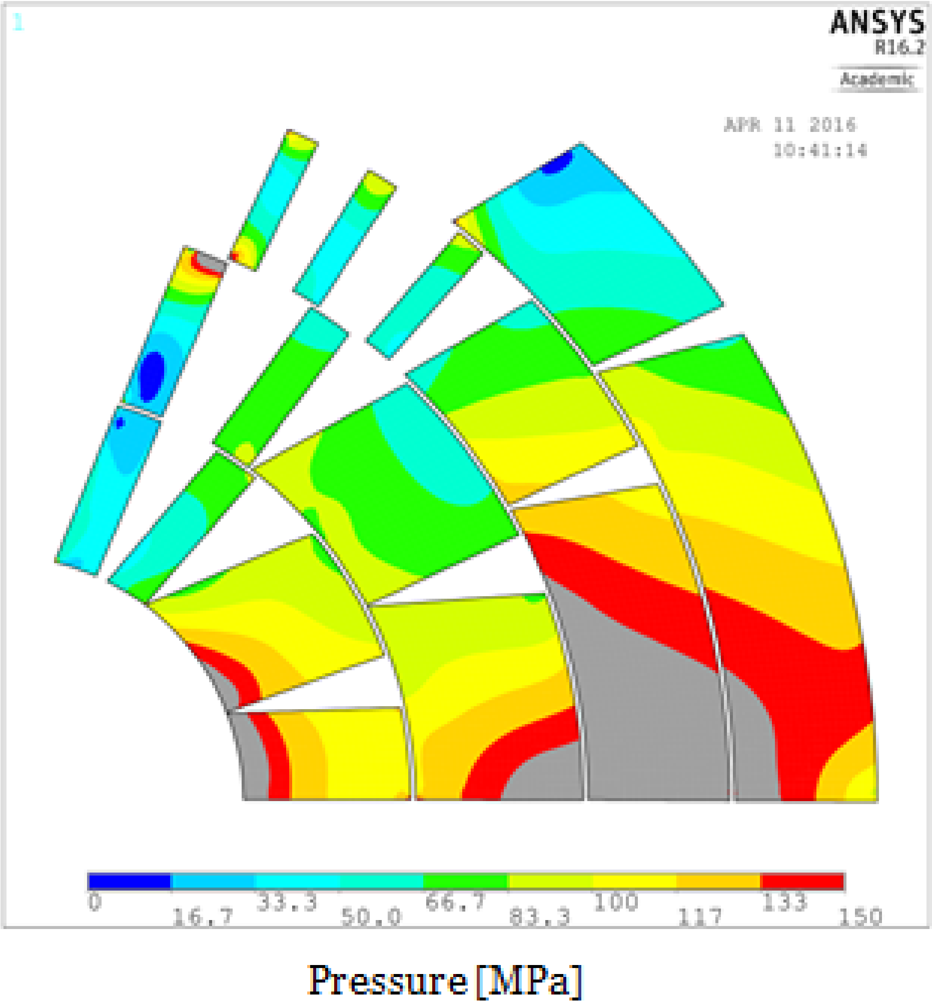

Figure 4.8: Von Mises stress within the coils during the assembly. Grey zones overcomes the scale.

worst cases the magnet could never reach the operating point.
In Fig. 4.10, the pole-coil contact pressure after energization is plotted.

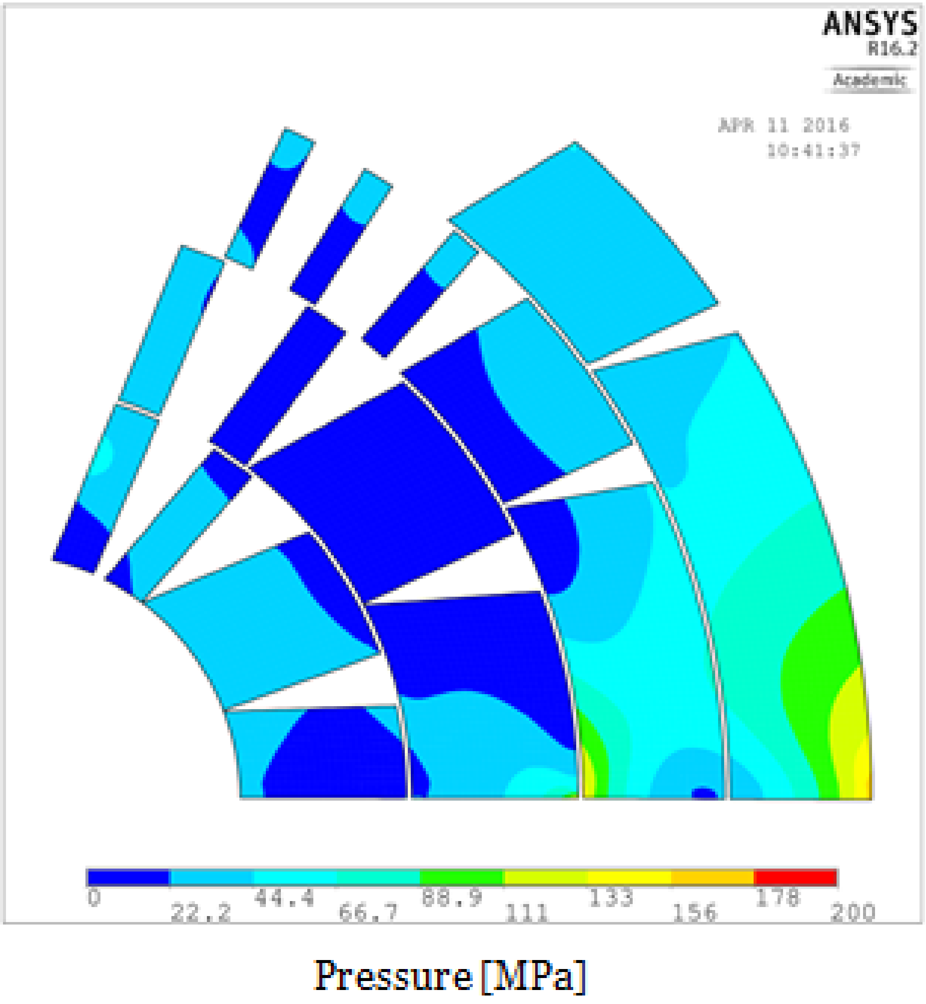

Figure 4.9: Von Mises stress within the coils during the cool-down.

It can be seen that the mechanical structure presented here gives enough azimuthal pre-stress to the first, to the second and to the fourth layer.

The third layer, instead, has some detachments in the lateral sides of the pole turn; by the way, the acceptance criterion defined previously is accomplished, because the conductor mid-point is in contact with the pole, with a pressure larger than 2 MPa.

In Fig. 4.11, the Von Mises stress within the coils after energization is shown. As during the cool-down, no particular issues are foreseen during this stage. Only a small zone of the third layer slightly overcomes the maximum allowed stress, but a bit of degradation in such a low field area should not affect the magnet performances. By the way, due to the fact that at room temperature the stress over-comes its maximum, this configuration is very hard to achieve. In conclusion, this mechanical analysis has to be iterated in the future in order to optimize it and make it feasible.

Tension within the iron

As just mentioned, the iron at 4.2 K suffers from tension larger than 200 MPa. In Fig. 4.12, the tension within the iron after the magnet energization is plotted. It can be noted that, generally, the tension is well below the maximum allowed of 200 MPa at 4.2 K. Only very small zones overcome this value, close to the hole in the pad and to the curve of the stainless steel insert. The situation can be optimized changing the curvature radius, and at this stage of the design it does not constitute a critical issue.

Stresses in other materials

In Table 4.11, the Von Mises stresses in the other components of the mechanical structure during assembly, cool-down and energization are reported. Comparing Table 4.11 with Tables 4.9 and 4.10, it can be seen that all the requirements are respected.

4.2.4 Quench protection

Dealing with high-field long accelerator magnets, quench protection is one of the main aspects to take into consideration right from the beginning of the design. In fact, because of the high inductance, it is very difficult to

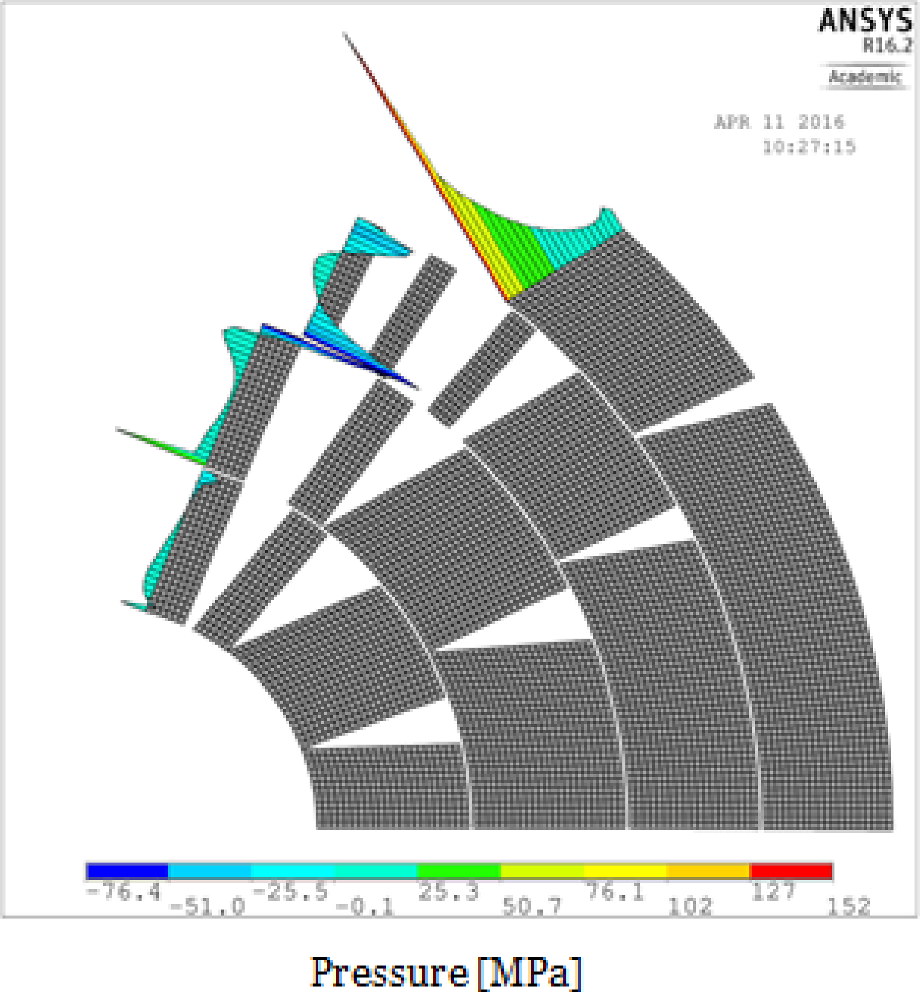

Figure 4.10: Pole-coil contact pressure after magnet energization. Positive values of the pressure mean that there is contact, negative values mean that there is detachment.

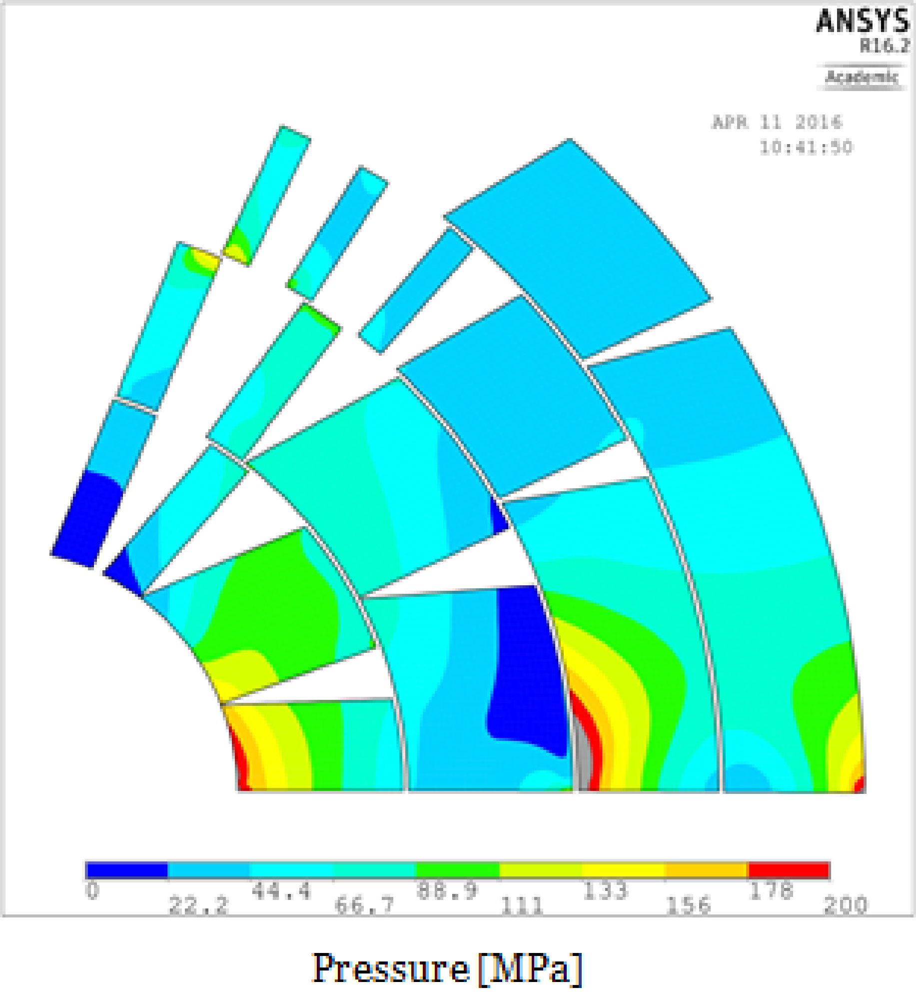

Figure 4.11: Von Mises stress within the coils after magnet full energization.

extract the huge stored energy, which has to be dissipated within the coils. Protection of these magnets can be achieved only by spreading the quench

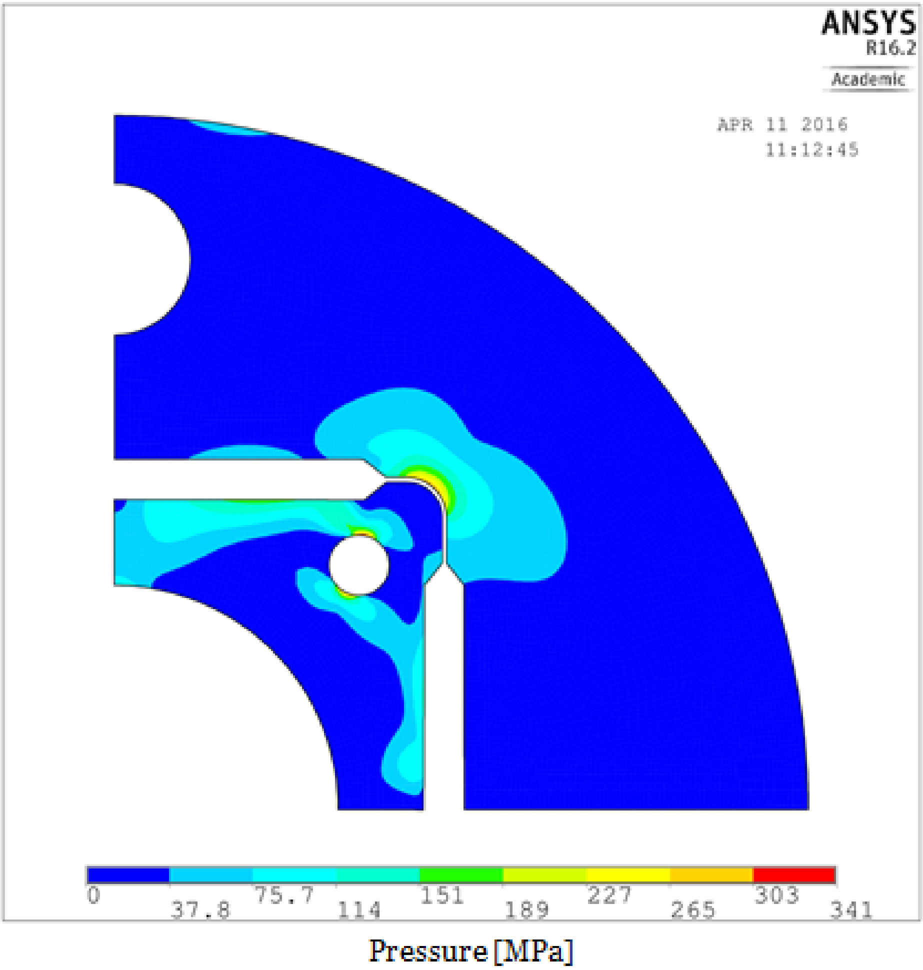

Figure 4.12: Tension within the iron after magnet energization.

over the largest area and in the shortest time possible (using therefore quench heaters, or the novel CLIQ technology [15]), and taking care of the copper quantity in the cables during the design.

Von Mises stresses in other parts of the magnet			
Material	**Assembly [MPa]**	**Cool-down [MPa]**	**Energization [MPa]**
SL steel	734	859	1010
Al shell	47	168	167
Iron	381	451	553
Ti Pole	668	1150	613

Table 4.11: Von Mises stresses in other parts of the magnet computed in other parts of the mechanical structure during the different phases.

As shown in Table 4.3, in the LF Cable the Cu/NCu ratio has been set to 2; this value comes from the particular care, during the magnetic design phase, to maintain the current density in the copper as low as possible, in order to reduce the hot spot temperature during a quench, which is obviously in the pole turn of the third layer (smallest conductor, high-field zone). The resulting layout is therefore a thoughtful compromise between quench protection, load line margin and conductor area optimization. The resulting current density in the copper is about 1100 A/mm^2. The quench protection acceptance criteria discussed in the EuroCirCol collaboration are the following; these numbers are intended to compare the designs with the same assumptions. The discussion on these numbers can be found in [38]:

- Hot spot temperature has to be lower than 350 K, when a quench is induced in the whole magnet 40 ms after the initial quench, at 105% of the operating current;
- The maximum voltage to ground has to be lower than 2 kV, in the same situation discussed above.

These requirements have been set in order to compare all the EuroCirCol designs on the quench protection point of view using simple assumptions, and in order to have a final design that can be protected. For this magnet, just this simple analysis has been performed. A more detailed protection

Quench protection results	
Hot spot temperature	**Max voltage to ground**
330 K	1.2 kV

Table 4.12: Quench protection results for the EuroCirCol $\cos\theta$.

study has been performed on the upgraded design described in section 4.3. This study does not intend to provide a detailed protection analysis.

In Table 4.12 the hot spot temperature and the voltage to ground of the magnet presented here are reported, under the assumptions described above. The protection study has been performed using Coodi [39]; material properties are from the NIST database [40], and the chosen copper RRR is 150. It is easy to note that the quench protection of the magnet satisfies the requirements. More details on the protection can be found in [39].

4.2.5 Conclusions

In this section, we have presented a four layer, graded Nb_3Sn magnet, with two conductors used for the magnetic design. The proposed magnet can reach an operating field of 16 T, as required by the EuroCirCol collaboration, being at the 90% of the load line at 4.2 K on both the conductors. The required conductor area is $\sim$ 168 cm^2, which is equivalent to $\sim$9.6 ktons of cable for the building of FCC; this number can be reduced by 20 % studying more in depth an alternative solution for the LF cable using pure copper strands. Field quality of the magnet is fully satisfactory.

The mechanical structure chosen is based on a bladders and keys option, with some modifications (uppercuts in the pole nose, and tapered shim on the mid-plane). The mechanical analysis has shown that the azimuthal pre-stress needed in order to maintain the pole-coil contact after the magnet energization can be hardly achieved; in particular, the third layer pole turn has some detaching zones, but it nearly accomplishes the acceptance criteria. However, this requirement makes it very difficult to maintain the stresses lower than the maximum allowed in the coils and the iron yoke,

especially during the assembly; the mechanical design has therefore to be optimized in future studies, but can be considered a satisfactory starting point. The present option surely needs further iterations in order to improve the performances, but shows that it is possible to design a mechanical support structure for this magnet.
The magnet can be considered safe on the quench protection point of view, following the EuroCirCol requirements for the comparison of the three layouts. The copper quantity in the LF cable has been optimized in order to contain the hot spot temperature within the limits, but keeping a good electromagnetic efficiency. The resulting hot spot temperature is 330 K at 105% of the operating current, and the maximum voltage to ground is 1.2 kV.
A further iteration of the design of this magnet is shown in the next section 4.3, with particular emphasis on the quench protection.

4.3 Design of a 16 T $\cos\theta$ dipole operating at 1.9 K at 86% of the load line

In this section, an improvement of the magnet presented in section 4.2 is presented [41]. For this design, the constraints have been modified to explore a larger range of parameters and study their effects on the results.

4.3.1 Design constraints

The updated design constraints are reported in Table 4.13.
The main differences are that the operating temperature is 1.9 K instead that 4.2 K, but with a margin of 86% on the load line instead that 90%. Considering that a 90% on the load line at 4.2 K is equivalent to about 80% at 1.9 K, it means that this magnet design could significantly reduce the amount of conductor. Moreover, the minimum copper/not-copper ratio has been changed from 1 to 0.8, giving the possibility to explore the impact of having more superconductor in the first two layers. The other parameters have been kept.

Main design paramenters	
Bore inner diameter	50 mm
Beam distance	250 mm
Bore nominal field	16 T
Operating temperature	1.9 K
Operation on load-line	86 %
Maximum strand number	51
Insulation thickness	0.15 mm
Cu/NCu	≥ 0.8
Field harmonics (geo/sat)	$\leq$3/10 arbitrary units
Iron yoke outer radius	400 mm
Aperture number	2

Table 4.13: Main design parameters for the comparison of the three magnet layouts.

4.3.2 Magnetic design

The electromagnetic study has been performed using ROXIE, again in the configuration of a double aperture inside the same yoke as the layout presented in 4.2.2. Again, in order to increase the efficiency of conductor and reduce the total quantity of superconductor it is necessary to use a grading of the current density in the coils, considering a four layers configuration. The cross section optimizations have been performed mainly to minimize the conductor quantity, keeping the requirements of field quality and conductor maximum field margin on load line. Fig. 4.13 presents the coil cross section with magnetic field, while Fig. 4.14 shows the iron shape with the magnetic field. Again, this configuration is a generalization with no mechanical meanigs of the single aperture mechanical structure presented in section 4.3.3.

The two cables used for the design are described in Table 4.14.

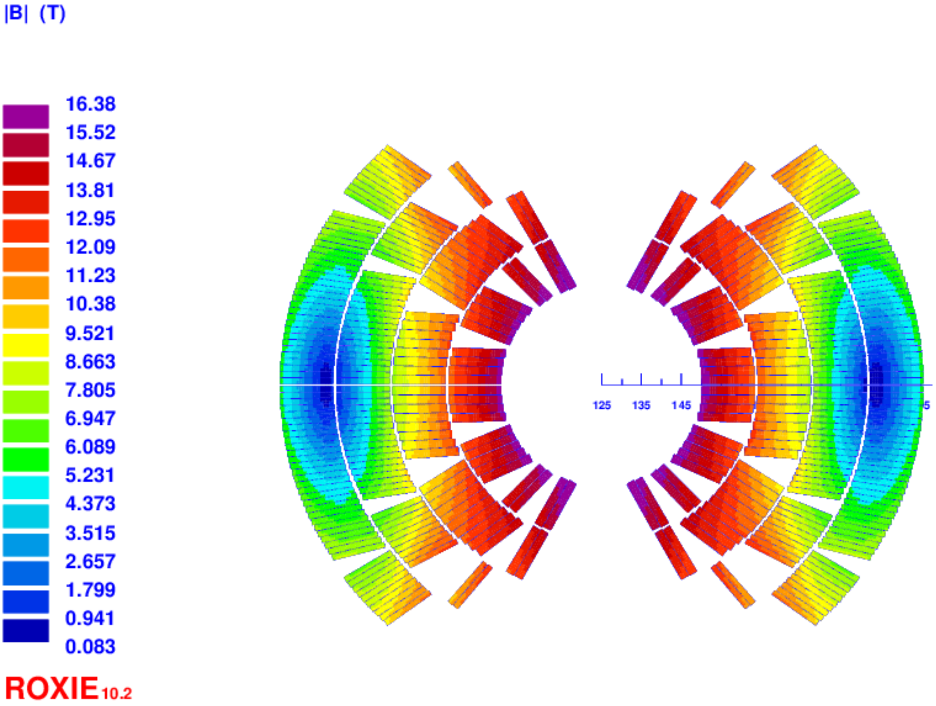

Figure 4.13: Field distribution on one coil cross section for the updated cosine-theta solution.

As it can be seen, comparing with table 4.3, the HF cable has more superconductor, and both the cables are smaller, carrying more current. This is an effect of the margin increas. Moreover, the LF cable has more copper, due to protection reason.
The maximum operating point on the load line at 1.9 K is 86% for both the conductors. The minimum separation between conductor blocks (minimum wedge thickness at in the winding radius of the mandrel) is 0.82 mm. This value has been considered acceptable if compared to the value of the minimum wedge thickness in the LHC main dipole, which is 0.70 mm.

Conductor properties		
	HF Cable	**LF Cable**
Strand number	22	36
Strand diameter	1.1 mm	0.71 mm
Bare width	13.2 mm	13.3 mm
Bare inner thickness	1.892 mm	1.204 mm
Bare outer thickness	2.072 mm	1.320 mm
Insulation	0.15 mm	0.15 mm
Keystone angle	0.5Â°	0.5Â°
Cu/NCu	0.85	2.15
Operating current	11180 A	11180 A
Operating point on load line (4.2 K)	86 %	86 %
Number of turns(per aperture, per quadrant)	33	68

Table 4.14: Conductor properties of both the cables used for the design of the upgraded EuroCirCol $\cos\theta$

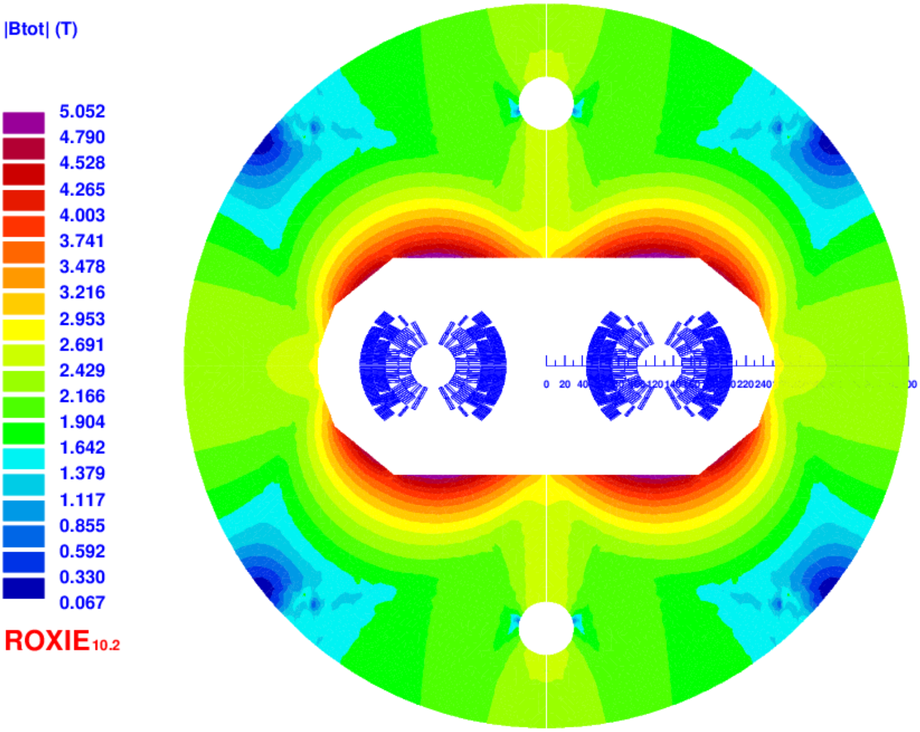

Figure 4.14: Double aperture cross section for the updated cosine-theta solution. The white zone around coils indicates the space for the thick stainless steel pads (collars).

The field quality has been optimized at high field (16 T), with all harmonics below 1 unit. The effect of iron saturation in the harmonic variation during ramp-up is moderate, with Δb3 = 6 units. Other minor effects (conductor hysteresis, a.c. effects) have not been considered. Again, only the quadrupole component present a larger variation (Δb2=20 units) because of the cross talking of the two apertures. At this stage corrections of these oscillation has not been compensated and they do not give particular

worries.
The evaluation of conductor mass is critical for the cost estimation, because great part of the total FCC dipole magnet cost is dominated by conductor production cost. The present magnet design (updated solution) requires, for the whole FCC circumference length of 100 km, a total conductor mass of 7.59 ktons. The calculation has been performed using the parameters reported in table 4.7. The previous solution with larger margin led to 9.6 ktons of conductor. Considering that the low field conductor requires a large content of pure copper for protection reason (to limit the hot spot temperature), like for the previous design, again an alternative solution could be mixing, during the cabling process, pure copper strands with superconducting strands. The average copper fraction necessary for protection would be the same, but it would allow to diminish the quantity of superconducting strands by 1.61 ktons for the whole FCC, which is equivalent to 21% of the total conductor mass (see section 4.2.2 for details).

4.3.3 Mechanical design

The mechanical structure chosen for the magnet is based again on the bladders and keys (B&K) technology, with some modifications. Due to the huge magnetic forces arising when charging the dipole up to 16 T, a standard B&K mechanical structure is not able to fulfill all the mechanical requirements. It is fundamental preserving the pole-coil contact when the magnet is fully energized and, at the same time, keeping the stresses within the given limits. The parameters used for the computation and the stress limits are the same presented in Tables 4.9 and 4.10. Between the several configurations found, the most promising is reported in Fig. 4.15.

The mechanical components include a thick stainless steel pad (collar), close to the coils, a tilted stainless steel key, an iron yoke and a 55 mm thick aluminum alloy shell. Pad and yoke are cut vertically to allow the assembly of the magnet. The thick stainless steel pad allows proper distribution of the pressure, transferred through the key in the coil region, and avoid excess of peak stress. The stainless steel C-clamp helps keeping the pole-coil contact when the magnet is fully energized. In order to balance

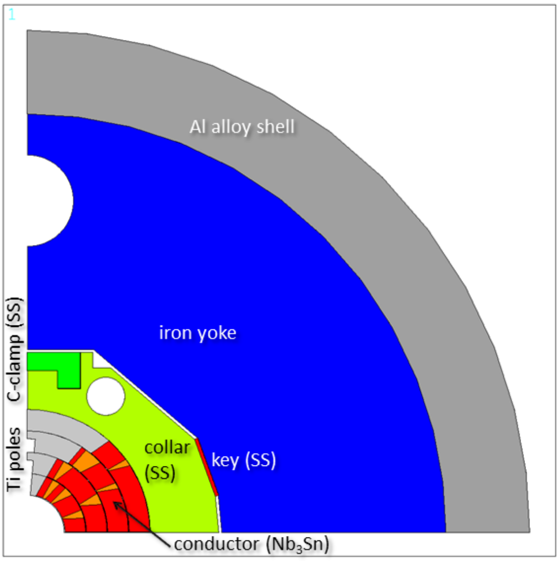

Figure 4.15: Mechanical structure of the magnet.

the azimuthal pre-stress on the coils during the-cool down, undercuts in the first, second and third layer of the titanium poles are foreseen.
Finite element analyses have been carried out using the software ANSYS, aiming at optimizing the free parameters of the configuration (collar thickness, key length, key position angle, shell thickness, shape of the Ti poles, C-clamp dimension, hole position and size in the collar). The design results are quite satisfactory because the pole-coil contact is fully ensured (see Fig. 4.16) and the peak stresses are within the prescribed limits (see Fig. 4.17, 4.18 and 4.19).

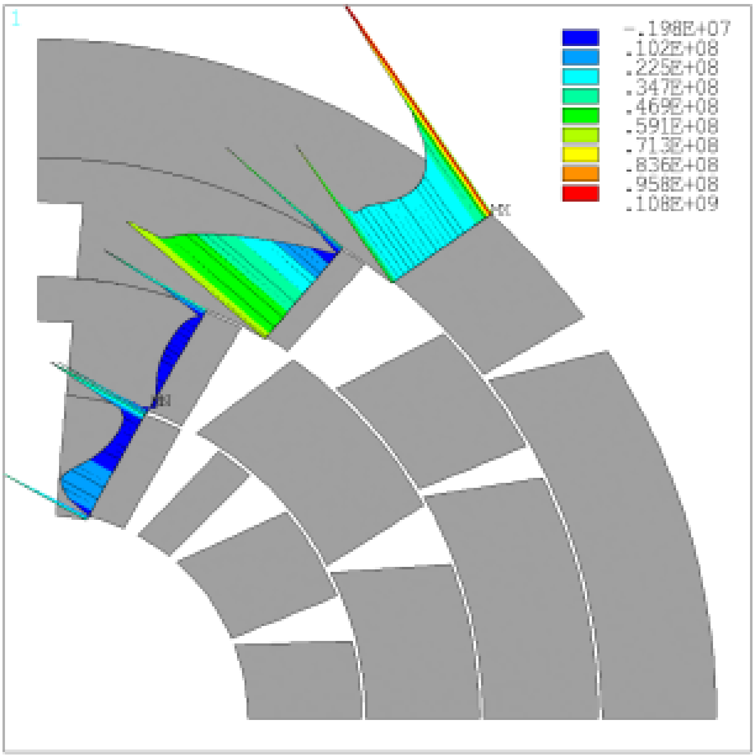

Figure 4.16: Contact pressure (Pa) at the coil/pole interfaces

4.3.4 Quench protection

The quench protection of this magnet has been studied more in depth than for the previous version, trying to design a more realistic protection system, based on quench heaters, with a detection and validation time, instead of having a generic intervention time of 40 ms [42]. Moreover, the electromagnetic model described in chapter 2 for the simulation of dynamic effects on the inductance due to inter-filament coupling currents has been used.

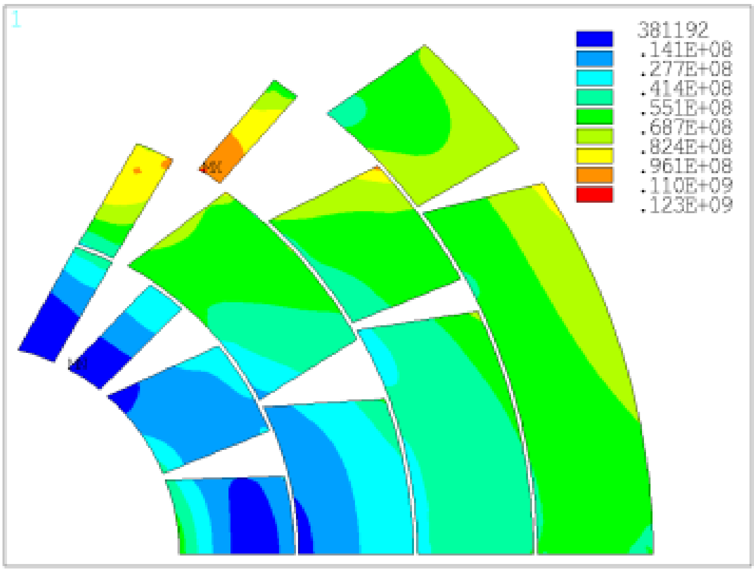

Figure 4.17: Von Mises stress (Pa) in the conductor after assembly.

Protection heaters design

The quench protection heaters were designed considering the present state-of-the-art trace-based heater technology, which is used also in the HL-LHC inner triplet quadrupoles [43]. The heater strips are 25 μm thick stainless steel strips glued on a 75 μm thick layer of polyimide. The insulation thickness is increased by 50% from the HL-LHC quadrupole to account for the higher voltages.

It is assumed that the two double-pancakes in $\cos\theta$ are reacted separately, allowing placing of heaters on the surface of each coil layer. Based on simulations it was necessary to cover a large fraction of the coil surface to produce a sufficiently wide normal zone in the coil. Fig. 4.20 shows the approximate locations of the heater strips, that cover 70% of the coil turns. Each heater strip is 14.3 m long, and is based on heating stations. The heating station length is 5 cm in each strip and 25 cm long copper plated

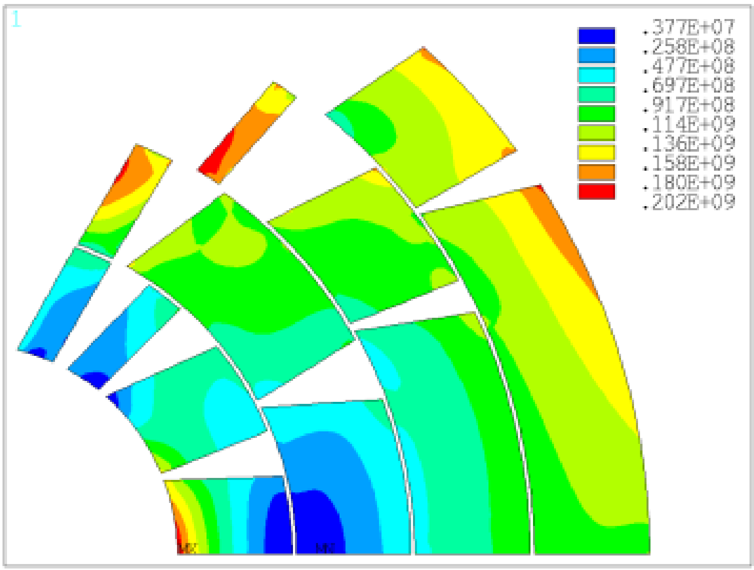

Figure 4.18: Von Mises stress (Pa) in the conductor after cool-down.

segment serves as a low-resistance bridge between them (see Fig. 4.21). The strips however have different widths as detailed in Table 4.15.

For the powering, the heater strips in each half-coil are connected into three circuits. The circuits have 2,3 or 6 identical strips connected in parallel to a Heater Firing Unit (HFU) with charging voltage of 450 V and capacitance of 19.2 mF. In series with each heater strip parallel-connection is assumed 0.5 Ω resistance for wires. The resulting peak powers are in the range of 60-90 W/cm, and the circuit RC-time constants about 30 ms.

The heater delays were simulated using the 2-D heat diffusion model CohDA [28]. Fig. 4.22 shows the delays as a function of magnetic field at 105% of operation current for the different considered heater powers and cables. The delays are computed for both conductors, at different values of the magnetic field (copper magneto-resistivity is taken into account); in fact, heater-induced quench has different delay time accordingly to the zone where the

Powering of the heater strips in one coil-half with 3 HFU				
Circuit	QH strips	Strip width (cm)	$P_{QH}(0)$ (W/cm^2)	τ_{RC} (ms)
HFU#1	1A, 1B, 2A, 2B, 2C, 2D	1.0	67	25
HFU#2	3B, 4C, 4B	1.7	76	27
HFU#6	3A, 4A	2.0	89	32

Table 4.15: Protection heaters powering parameters $\cos\theta$

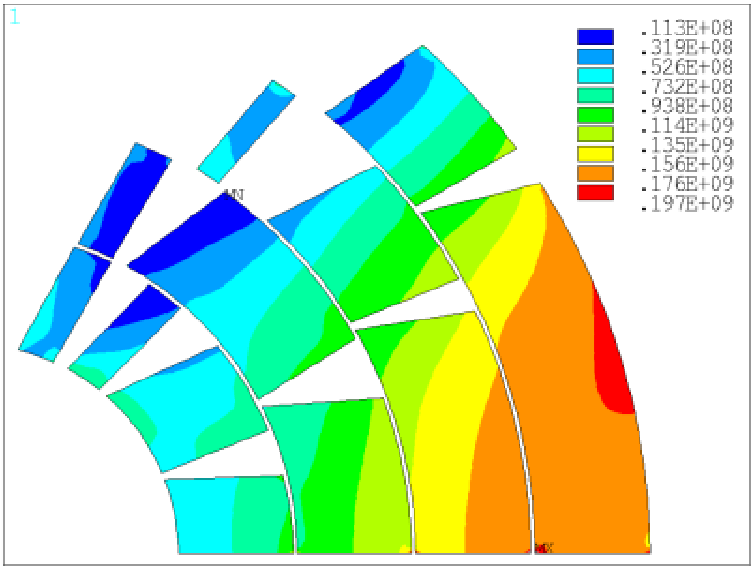

Figure 4.19: Von Mises stress (Pa) in the conductor after energization at 16 T.

heater is set, following the magnetic field shape.

Nominal protection study

The main goal of this protection study is to maintain the hot spot temperature (the temperature of the zone where the quench begins) within a certain level of safety. In this thesis, the maximum allowed temperature will be considered as 350 K. This number comes from the HiLumi-LHC experience with Nb_3Sn (see section 3.3). The quench protection system presented here is based on the quench heaters discussed previously. Table 4.16 shows the other parameters used for the computation.

Presence of dump resistor is not foreseen: as it can be seen in Table 4.13, this magnet has large inductance and large stored energy, therefore the amount of energy that could be extracted in an external resistance would

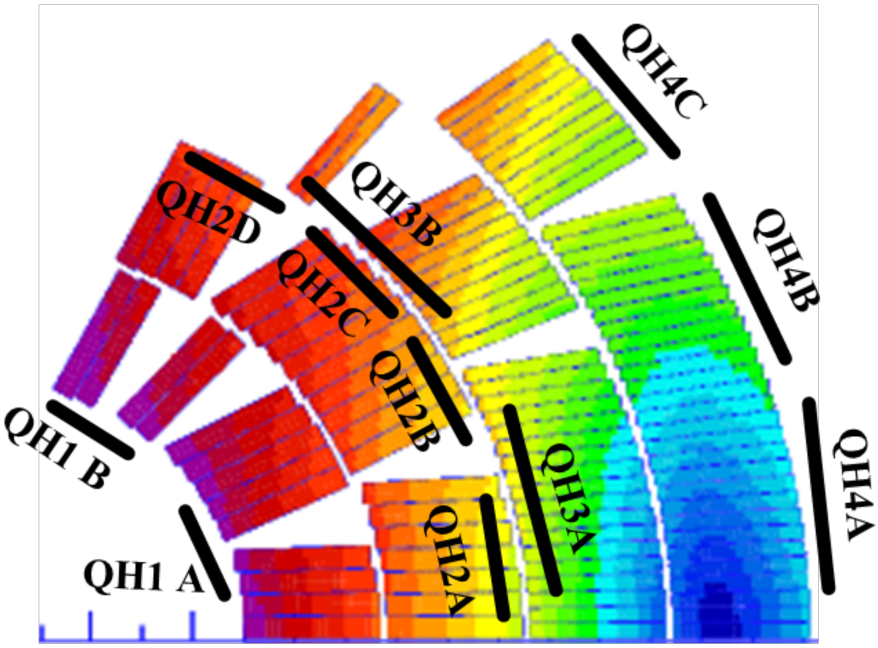

Figure 4.20: Location of heater strips on coil surfaces.

Figure 4.21: A heater strip geometry: Each strip has 5 cm long stainless steel heating stations placed with 30 cm period. Three different strip widths are used: 1.0, 1.7 and 2.0 cm.

be negligible, just adding a complication for the voltage study. The analysis has been performed using QLASA, making the following assumptions:

- The quench begins in the high field zone of the layer 3 (pole turn).

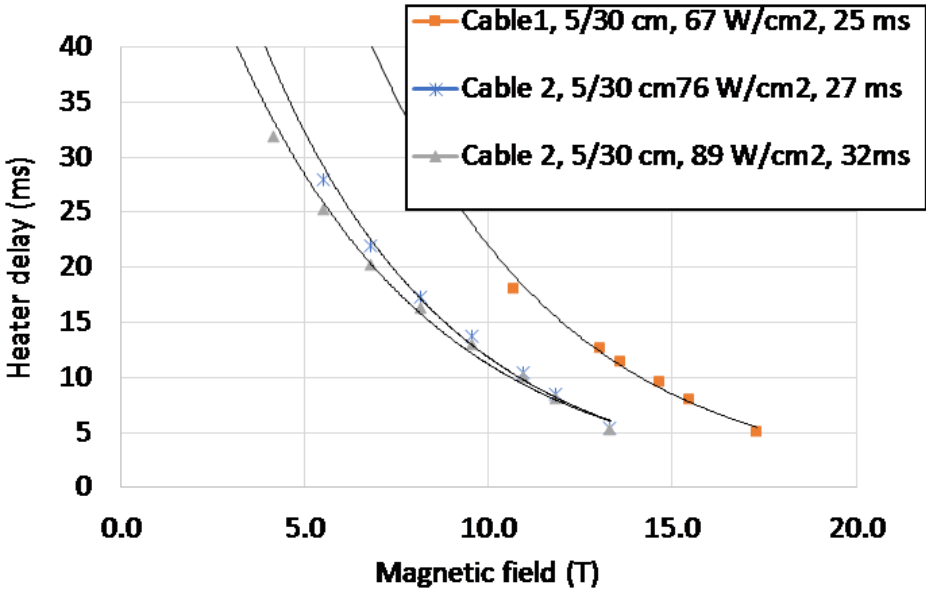

Figure 4.22: Heater delays in the EuroCirCol updated cos θ simulated with CoHDA, at 105% of operation current.

- The hot spot temperature is computed with adiabatic assumptions.
- Material properties are from MATPRO.
- The protection heaters delay time has been computed using CoHDA, following the scheme showed previously. Average values are used for the high-field and low-field zones of each layer.
- The quench is induced by heaters only in the turns covered by them; then, transversal propagation is taken into account.
- The quench is induced by heaters only under heating stations; then, longitudinal propagation is taken into account, while pre-heating coming from the heater copper sections is neglected.

Protection parameters	
Voltage threshold	100 mV
Validation time	10 ms
Switch opening delay time after validation	1 ms
Inter-filament coupling currents average decay time	15 ms

Table 4.16: Protection parameters for the updated EuroCirCol $\cos\theta$

Protection results		
	Nominal	No dynamic effects
MIITs	17.3 $\mathrm{MA^2s}$	18.2 $\mathrm{MA^2s}$
Hot Spot Temperature	332 K	357 K

Table 4.17: Protection results for the updated EuroCirCol $\cos\theta$

- The differential inductance of the magnet is computed considering the dynamic effects of inter-filament coupling currents on it; details on the model implemented in QLASA can be found in chapter 2.
- Inter-layer quench propagation is neglected.
- Quench back is neglected.
- Computation is performed at 105% of the operating current.

Table 4.17 shows the resulting hot spot temperature and MIITs, comparing the nominal scenario with a computation done neglecting the dynamic effects on the inductance. It is easy to note that, according to the nominal scenario, the magnet can be considered protected, also with a margin of about 20 K on the maximum allowed temperature of 350 K. It is interesting to consider, too, that neglecting the effect of coupling currents on the magnet inductance, the protection of this magnet would be considered very hard to achieve, because the temperature rises of about 25 K, and it goes slightly over the maximum allowed. This is a great application of the model

described in chapter 2, without which this magnet could be not considered feasible.
At this stage of the design, the analysis of heater failure scenarios has not been yet performed. It will be needed in future studies in order to ensure the protection redundancy.

Parametric study

In this section, a parametric study is presented, varying between reasonable values the most relevant parameters of the protection system and of the conductors. This study aims to show the direction to take for the future electromagnetic design upgrades of this magnet, in order to take the quench protection under control, or even to improve it, and to see how to eventually improve the protection parameters. The assumptions made are the same discussed previuosly.

While the quench develops and the consequent resistance rises up, a growing resistive voltage appears between the ends of the magnet. This voltage can be therefore measured and used in order to detect a quench. The voltage threshold is the value beyond which a quench is considered detected. However, superconductivity has for its own nature instabilities which cause voltage peaks; for this reason, after a quench is detected, it needs to be validated: the voltage has to stay over the threshold for a certain time, called validation time. Only after that, the quench protection system is activated. Therefore, the choice of the voltage threshold and of the validation time has to be done with care: these two parameters have to be low enough in order to reduce the MIITs developed during detection and validation, but high enough in order to avoid false quench triggering due to superconductor instabilities. In Fig. 4.23-left, the dependence of the temperature on the voltage threshold is showed, while in Fig.4.23-right the dependence on the validation time is represented. The other parameters have been taken as the nominal ones. It can be seen that the temperature does not strongly depends on the threshold, while the validation time has to be chosen with care, because every millisecond costs about 5 K.

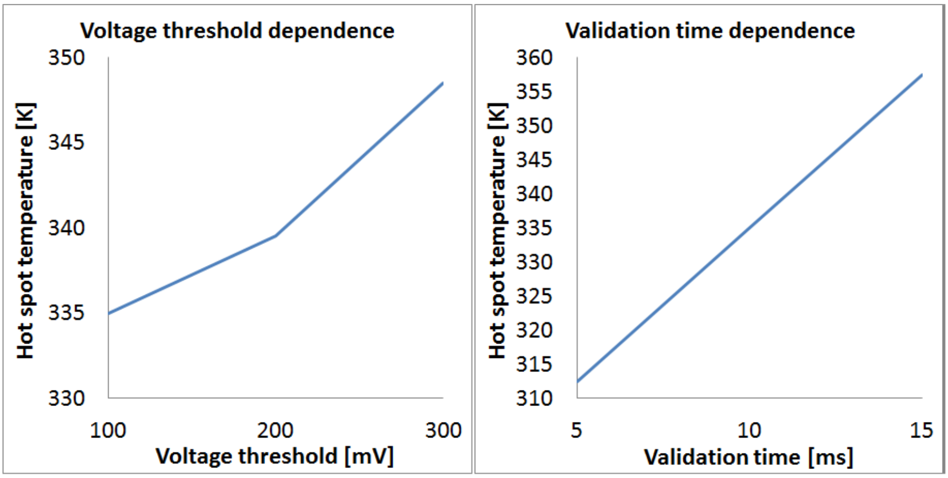

Figure 4.23: Hot spot temperature dependence on the voltage threshold (left) and on the validation time (right).

The RRR is defined as the ratio between the resistivity at room temperature and the resistivity at 10 K. A high RRR means that the copper is pure, and that its resistance at cold is low. Typically, a large RRR in the initial quench zone helps to maintain the hot spot temperature as a more pure copper allows a faster heat propagation. Fig. 4.24 shows the dependence of hot spot temperature on the RRR of HF and LF conductor respectively. It can be noted that the higher is the LF conductor RRR, the lower is the hot spot temperature, such as just explained. Nevertheless, for the HF conductor the behavior is opposite: this is due to the fact that the resistance developed by quench heaters is less with larger RRR. We should point out that the dependence on RRR is minimal in both the cases.

The Cu/NCu is the ratio between the copper and the other material fractions within the strand. A large content of copper is usually preferable for the protection, because it reduces the copper current density and the

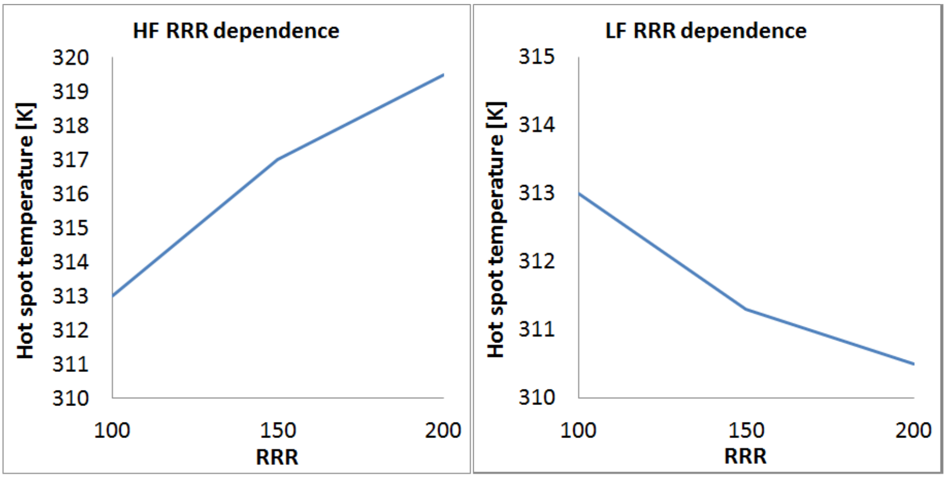

Figure 4.24: Hot spot temperature dependence on the HF (left) and LF (right)conductor RRR.

heat dissipation; however, it decreases the margin on the load-line, keeping constant the strand section. Fig. 4.25 shows the hot spot temperature dependence on the Cu/NCu of HF and LF conductor respectively. Also in this case, the behaviours are opposite: for the HF conductor, a larger amount of copper means that the resistance induced by heaters is lower, and that the hot spot temperature is therefore larger; instead, for the LF conductor, a larger amount of copper means that the initial quench zone warms up slowly, therefore the hot spot temperature decreases. The amount of copper have to be chosen with care, and with a good tolerance: in fact, as shown in Fig. 4.25, every 0.1 in Cu/NCu fraction costs 5-10 K in terms of hot spot temperature.

4.3.5 Conclusions and perspectives

In this section, we have presented the upgraded version of the EuroCirCol dipole $\cos\theta$ design, with particular emphasis on the quench protection study.

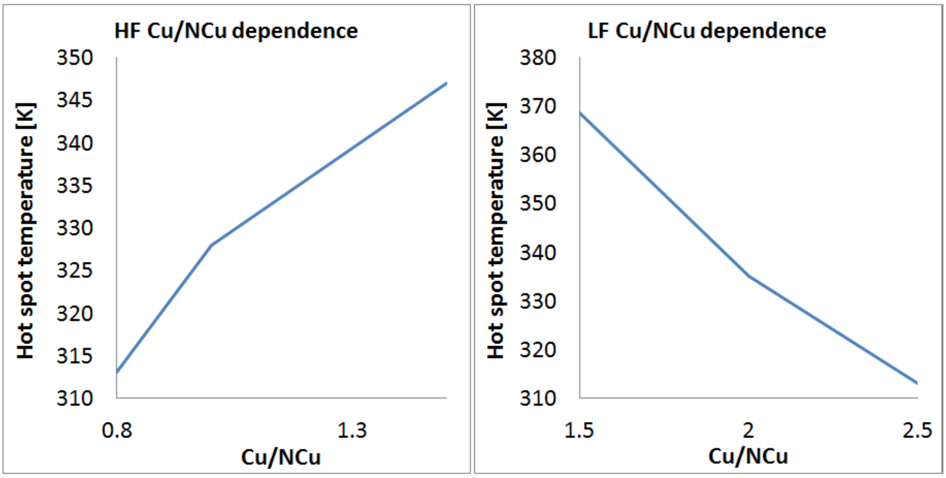

Figure 4.25: Hot spot temperature dependence on the HF (left) and LF (right) conductor Cu/NCu.

The main advantage of this version is that less conductor is used respect to the previous one presented in section 4.2, which could result in a large save of money for the FCC construction. Moreover, the mechanical study seems more efficient and feasible. However, future upgrades of the magnetic and mechanical design are foreseen in the next years.
The quench protection has been studied more in depth, and it is based on quench heaters, which have been designed with realistic assumptions. The nominal protection computation has been performed, showing that the hot spot temperature of the magnet can be maintained under control, within the safe value of 350 K. In particular, we have understood that the use of novel electromagnetic models which simulate the effect of inter-filament coupling currents on magnet inductance, described in chapter 2 helps to design more performing magnets. In fact, without using it, the protection of this magnet could be considered problematic, and this magnet would not be considered for future upgrades; instead, we are still working on the design improvement, as we believe that that a feasible design will be achieved.

Moreover, a parametric study has been performed, showing the dependence of the hot spot temperature on the main protection and conductor parameters. This work shows that the temperature depends mainly on the Cu/NCu of the two conductors and on the validation time, while it is slightly dependent on the RRR and on the voltage threshold. This study can be useful for future upgrades of the electro-magnetic design and for the development of the protection system.

In future studies, the analysis of failure scenarios will be carried on, in order to ensure the protection redundancy, and the analysis of peak voltages during a quench will be performed.

Chapter 5

Conclusions and perspectives

Quench protection is one of the most challenging aspects of the design of high-performance accelerator magnets. The high-energy physics ambitions and needs lead to the design of more and more performing magnet, which are more and more difficult to protect. For this reason, quench protection of superconducting accelerator magnets has been studied more in deep details in the last years. The work presented here is inserted in this scenario, and it has the purpose of improving the quality of quench protection studies.
During the test sessions of the LARP prototype magnets, it has been noticed that the current discharge could not be simulated using the nominal magnet inductance, even when analyzing simple tests with large dump resistors, and no spontaneous quench. In fact, in this case, the current decay should be a simple exponential decay (the solution of a LR circuit), with a decay time $\tau = \frac{L}{R}$. However, it is not possible to fit the experimental decays using exponential functions with decay time obtained by the nominal inductance, or the one measured during standard magnetic measurements; moreover, the decay time appears lower than expected, showing that the magnet inductance could be lower than expected during a quench. The understanding of this phenomenon can be considered very useful for quench protection studies, because an inductance reduction helps to discharge the current and to maintain the voltages; the comprehension of this

phenomenon can be therefore used to design more performing magnet, making more reliable and realistic protection studies.
Usually, such a phenomenon is explained with quench back, which can increase the magnet resistance. But, in this case,, quench back is not a reliable solution, because it needs some time (∼10 - 100 ms) to occur, while the apparent inductance reduction appears immediately, at the very beginning of the discharge. For this reason, the solution of the problem has been searched in electromagnetic coupling with external circuit.
This work shows that the inductance reduction of superconducting magnets during a quench can be explained with inter-filament coupling currents (IFCC). IFCC are a well-known phenomenon in superconductivity: briefly, during magnetic field changes, coupling currents are generated between the superconducting filaments which constitutes the strands. These currents dissipate heat going through the strand copper matrix, and it is well understood that they help to heat the magnet, and that, at large current derivative, they can induce a quench. However, we have showed that a connected, but different phenomenon can be associated to IFCC: they can be considered as magnetization currents (they are loop currents generated by the field changes), therefore the coils can be considered as a magnetized material; this affects the magnet inductance, such as the iron does. Here we have presented an electromagnetic model which can be used to compute the inductance during a quench in superconducting magnet, considering the effect of IFCC. It is a first-order analytical model, which depends basically on the IFCC decay time; by the way, it aims to show that the IFCC can affect the inductance and the decay in a noticeable way, and that it can explain the experimental evidence explained before. The experimental comparison of this model has been successful, and it has been shown that it is necessary to fit experimental decays impossible to describe until now.
Moreover, we have explained how to measure the inductance of a magnet during a quench. This measurement is different from a standard one, which is usually made at very low ramp-rate, in order to avoid quench resistance.
An experimental measurement of the inductance of a magnet has been performed following the method described here, and a comparison of the results has been made with the IFCC model, giving another experimental

confirmation of the inductance reduction phenomenon. The agreement of the model with the experimental measurement is satisfying, and confirms that IFCC can describe the experimental measured inductance reduction with a good approximation, even with the simple model presented here. Then, the quench protection of MQXF is reported in this thesis, with emphasis on the inductance reduction due to the IFCC. MQXF is the low-β quadrupole for the intersection regions of HiLumi LHC, and quench protection has been one of the most challenging aspects during the design phase. The use of the model describing the effect of IFCC on the inductance has helped to prove the magnet safety during a quench. A complete protection study is reported here, showing that hot spot temperature and peak voltages can be maintained under control, even with redundancy of the protection system.
Finally, the magnetic design of a bending dipole for FCC is reported in this work. FCC is am international project just started under the CERN leadership, and it has as target the construction of a circular accelerator able to collide 50 TeV proton beams, within a 100 km length collider. In order to reach this target, 16 T Nb_3Sn magnets are needed to bend the beams. Here the magnetic and mechanical design of two cosine theta layouts is reported. The design has been made taking care of reducing as much as possible the quantity of conductor within the coils, in order to keep the costs under control (the conductor is the most expensive component of a Nb_3Sn superconducting magnet). A key role can be played by the quench protection in order to reduce the amount of conductor: in fact, a conservative protection study has the effect of increasing the copper quantity in the conductor, and therefore of increasing the amount of conductor. For this reason, the quench protection study of the presented magnets has been performed using the model which considers the inductance reduction due to the IFCC, giving the possibility of designing a more performing and compact magnet which can be considered safe on the protection point of view. This work can be considered one of the first attempts to describe the inductance during a quench as a dynamic quantity, which is an unknown of the problem, and it is not known a-priori. In fact, considering the transient effect of IFCC, the inductance of the magnet depends on the current

discharge, and vice-versa. Despite its simplicity and its assumptions, the model presented here can be implemented in quench software, and the agreement with experimental data is good. It is almost completely analytical, and it can be considered a theoretical and physics background for more complex and less approximated numerical works, such as LEDET[44] or STEAM[45], which have similar results.

Acknowledgments

First of all, I would like to thank my supervisor Dr. Massimo Sorbi. During these three years, we have worked together, and he has always been available for my needs, as professor, and also as a person. It is not obvious to find people like him at work. I have learned to perform independent research under his supervision, and my professional owes a lot to him.

I would like to thank my research group, and the whole LASA staff. It has been important for me to find a working place like this, where everyone is disposable to the needs of the other.

I would like to thank all the people I have collaborated with. I have always find available people, and we have always made a good work together.

I would like to thank the two referee of this thesis, Prof. Luisa Chiesa and Dr. Umberto Gambardella. Their very useful comments and suggestions helped me to increase the quality level of this work, making it much better than the previous version.

I would like to thank my friends and my family. It is important for me to have people who care about you, with whom you can freely speak about your life, and I am lucky in this.

Last but not least, I would like to thank my wife Ilaria and my daughter Caterina. Thank you for having supported me during these years, for being present every day, in joy and in sorrow. You are the best thing in my life.

Bibliography

[1] Martin N. Wilson, 1983, Superconducting magnets

[2] G. Iannone *et al.*, Composite superconducting wires for fast ramped magnets, *Composites Part B: Engineering*, Vol.90, 2016.

[3] HiLumi website, http://hilumilhc.web.cern.ch

[4] LARP website, http://www.uslarp.org

[5] H. Felice *et al.*, Design of HQ - A High Field Large Bore Nb_3Sn Quadrupole Magnet for LARP, *IEEE Transactions on Applied Superconductivity*, Vol.19, No.3, 2009.

[6] G. Chlachidze *et al.*, Performance of HQ02, an optimized version of the 120 mm Nb_3Sn LARP quadrupole, *IEEE Transactions on Applied Superconductivity*, Vol.24, No.3, 2014.

[7] H. Bajas *et al.*, Cold Test Results of the LARP HQ Nb_3Sn Quadrupole Magnet at 1.9 K, *IEEE Transactions on Applied Superconductivity*, Vol.23, No.3, 2013.

[8] V. Marinozzi, Study of the quench propagation in the high field superconducting quadrupoles for the LHC luminosity upgrade, Master thesis, University of Milan, 2013; Tech. Rep. TD-13-013, Fermilab Technical Division, 2013. Presented on 23 July 2013.

[9] L.Rossi, Study of superconducting-to-resistive transition for the US-LARP large high field quadrupoles for the LHC upgrade, Master thesis, University of Milan, 2012; Tech. Rep. TD-12-011, Fermilab Technical Division, 2012.

[10] L. Rossi and M. Sorbi, QLASA: A computer code for quench simulation in adiabatic multicoil superconducting windings, Nat. Inst. of Nucl. Phys. (INFN), Rome, Italy, Tech. Rep. TC-04-13,2004.

[11] V. Marinozzi, Guidelines for the quench analysis of Nb3Sn accelerator magnets using QLASA, Tech. Rep. TD-13-008, Fermilab Technical Division, 2013.

[12] N. Schwerg, H. Henke, and S. Russenschuck, Numerical calculation of transient field effects in quenching superconducting magnets. PhD thesis, Berlin, Berlin, Tech. U., Berlin, department of Electrical Engineering and Computer Science. Presented on 18 Nov 2009.

[13] S. Russenschuck, Field Computation for Accelerator Magnets: Analytical and Numerical Methods for Electromagnetic Design and Optimization. Weinheim: Wiley, 2010.

[14] M. Sorbi and V. Marinozzi, Magnetization Heat in Superconductors and in Eddy Current Problems: A Classical Thermodynamic Approach, *IEEE Transactions on Applied Superconductivity*, Vol.26, No.6, 2016.

[15] E. Ravaioli *et al.*,New coupling loss induced quench protection system for superconducting accelerator magnets, *IEEE Transactions on Applied Superconductivity*, Vol.24, No.3, 2014.

[16] H. Bajas *et al.*, Test Results of the LARP HQ02b Magnet at 1.9 K,*IEEE Transactions on Applied Superconductivity*, Vol.25, No.3, 2015.

[17] M. Sorbi *et al.*, Measurements and analysis of dynamic effects in the LARP model quadrupole HQ02b during rapid discharge, *IEEE Transactions on Applied Superconductivity*, Vol.26, No.4, 2016.

[18] S. Mariotto, Studio e analisi della propagazione del quench in un quadrupolo superconduttivo ad alto campo magnetico in presenza di effetti dinamici, Bachelor degree Thesis, UniversitÃ degli Studi di Milano, Physics Dep., 2014

[19] D.A. Edwards, M.J. Syphers, An introduction to the physics of high energy accelerators. Wiley&Sons editors, 1993.

[20] P. Ferracin *et al.*,Development of MQXF, the Nb_3Sn low-β quadrupole for the HiLumi LHC,*IEEE Transactions on Applied Superconductivity*, Vol.26, No.4, 2016.

[21] E. Todesco, Quench limits in the next generation of magnets, CERN yellow report 2013-006 10-16 (2013).

[22] G. Manfreda, Review of ROXIE material properties database for quench simulation, TE-MSC internal note 24, CERN, December 2011.

[23] G. Manfreda, L. Rossi, and M. Sorbi, MATPRO upgraded version 2012: a computer library of material property at cryogenic temperature, Tech. Rep. INFN-12-04/MI, INFN, April 2012.

[24] G. Manfreda *et al.*, Quench protection study of the low-β quadrupole for the LHC luminosity upgrade, *IEEE Transactions on Applied Superconductivity*, Vol.24, No.3, 2014.

[25] V. Marinozzi *et al.*, Study of quench protection for the Nb_3Sn low-β quadrupole for the LHC luminosity upgrade (HiLumi LHC), *IEEE Transactions on Applied Superconductivity*, Vol.25, No.3, 2015.

[26] V.Marinozzi *et al.*, Quench protection study of the updated MQXF for the LHC luminosity upgrade (HiLumi LHC), *IEEE Transactions on Applied Superconductivity*, Vol.26, No.4, 2016.

[27] G. Ambrosio *et al.*, Test results of the first 3.7 m long Nb_3Sn quadrupole by LARP and future plans, *IEEE Transactions on Applied Superconductivity*, Vol.21, No.3, 2011.

[28] T. Salmi *et al.*, A novel computer code for modeling quench protection heaters in high field Nb_3Sn accelerator magnets, *IEEE Transactions on Applied Superconductivity*, Vol.24, No.4, 2014.

[29] E. Ravaioli *et al.*,Advanced quench protection for the Nb3Sn quadrupoles for the high luminosity LHC, *IEEE Transactions on Applied Superconductivity*, Vol.26, No.3, 2016.

[30] FCC website, https://fcc.web.cern.ch/Pages/default.aspx

[31] EUROCIRCOL website, https://fcc.web.cern.ch/eurocircol/Pages/default.aspx

[32] V. Marinozzi *et al.*, Preliminary design of a superconducting main dipole for the Future Circular Collider, *Physical Review Special Topic Accelerators and Beams*, submitted for publication.

[33] A. Ballarino, and L. Bottura, Targets for R&D on Nb_3Sn conductor for High Energy Physics,*IEEE Transactions on Applied Superconductivity*, Vol.25, No.3, 2015.

[34] S. Caspi *et al.*, The use of pressurized bladders for stress control of superconducting magnets,textitIEEE Transactions on Applied Superconductivity, 11, 6948843 (2002).

[35] S. Farinon *et al.*,The Design of Superconducting Separation Dipoles D2 for the High Luminosity Upgrade of LHC, *IEEE Transactions on Applied Superconductivity*, Vol.26, No.4, 2016.

[36] E. Acerbi *et al.*, The 18 Tesla-100 mm 4.2 K free bore solenoid for LASA-Milan, *IEEE Transactions on Applied Superconductivity*, Vol.28, n.1, 1992.

[37] M. Coccoli *et al.*, Fabrication and performance of Nb3Sn Rutherford-type cable with Cu added as a separate component, *IEEE Transactions on Applied Superconductivity*, Vol.14, n.2, 2004.

[38] https://fcc.web.cern.ch/eurocircol/

[39] T. Salmi *et al.*, Quench protection analysis integrated in the design of 16 T Nb_3Sn dipoles for the Future Circular Collider, *Physical Review Special Topic Accelerators and Beams*, submitted for publication.

[40] www.webbook.nist.gov

[41] M. Sorbi *et al.*, The EuroCirCol 16T Cosine-Theta Dipole Option for the FCC,*IEEE Transactions on Applied Superconductivity*, accepted for publication.

[42] V. Marinozzi *et al.*, Quench Protection Study of the Eurocircol 16 T $\cos\theta$ Dipole for the Future Circular Collider (FCC), *IEEE Transactions on Applied Superconductivity*, accepted for publication.

[43] H. Felice *et al.*, Instrumentation and quench protection for LARP Nb_3Sn magnets, *IEEE Transactions on Applied Superconductivity*, vol.19, no.3, 2009.

[44] E. Ravaioli, B. Auchmann, M. Maciejewski, H.H.J. ten Kate, and A.P. Verweij, Lumped-Element Dynamic Electro-Thermal model of a superconducting magnet,*Cryogenics*, vol.80, no.3, 2016.

[45] L. Bortot *et al.*, A Consistent Simulation of Electrothermal Transients in Accelerator Circuits, *IEEE Transactions on Applied Superconductivity*, Vol.27, n.4, 2017.